

AUTHOR QUERY FORM

 <p>AIP Publishing</p>	<p>Journal: J. Math. Phys.</p> <p>Article Number: 16-0766JMP</p>	<p>Please provide your responses and any corrections by annotating this PDF and uploading it to AIP's eProof website as detailed in the Welcome email.</p>
--	--	--

Dear Author,

Below are the queries associated with your article. Please answer all of these queries before sending the proof back to AIP.

Article checklist: In order to ensure greater accuracy, please check the following and make all necessary corrections before returning your proof.

1. Is the title of your article accurate and spelled correctly?
2. Please check affiliations including spelling, completeness, and correct linking to authors.
3. Did you remember to include acknowledgment of funding, if required, and is it accurate?

Location in article	Query/Remark: click on the Q link to navigate to the appropriate spot in the proof. There, insert your comments as a PDF annotation.
Q1	Please check that the author names are in the proper order and spelled correctly. Also, please ensure that each author's given and surnames have been correctly identified (given names are highlighted in red and surnames appear in blue).
Q2	In the sentence beginning "The transport of sea ice floes..." the term "eddie" has been changed to "eddy." Kindly check and confirm.
Q3	In the sentence beginning "Such methods have been..." please check the usage of "anelastic."
Q4	Please define PDE at first occurrence.
Q5	In the sentence beginning "In order to streamline..." please indicate which appendix the term "an appendix" refers to.
Q6	In the sentence beginning "The matrix analysis of..." please indicate which appendix the term "the appendix" refers to.
Q7	In the sentence beginning "This derivation will also..." please indicate which appendix the term "the appendix" refers to.
Q8	Kindly check the edits made to the sentence beginning "A closer look at these figures...."
Q9	In the sentence beginning "In order to streamline..." please indicate which appendix the term "an appendix" refers to.
Q10	Please confirm the change in volume number and page number in Ref. 26.
Q11	Please provide arXiv number in Ref. 30.
Q12	If preprint Ref. 30 has subsequently been published elsewhere, please provide updated reference information (journal title, volume number, and page number).
Q13	AIP does not allow the use of "in preparation" in the references; therefore, we have changed Ref. 43 to "unpublished." If the article has been published, provide complete published information (volume, page number, and year) if available. If the article is an "early" or "advance" view published online by a journal before assignment to a volume and issue, please provide a DOI if available.
Q14	Please confirm the change in volume number in Ref. 44.
Q15	Please confirm the change in page number in Ref. 61.

Continued on next page.

Continued from previous page.

2 Please confirm ORCIDs are accurate. If you wish to add an ORCID for any author that does not have one, you may do so now.
3 For more information on ORCID, see <https://orcid.org/>.
4

N. B. Murphy –
J. Xin –
E. Cherkaev –
J. Zhu –
K. M. Golden –

Please check and confirm the Funder(s) and Grant Reference Number(s) listed:

National Science Foundation, Award/Contract Number DMS-1211179, DMS-0940249, DMS-1413454, DMS-1715680,
DMS-1522383

Office of Naval Research, Award/Contract Number N00014-13-10291, N00014-12-10861, N00014-18-1-2552

Please add any additional funding sources

Thank you for your assistance.

5 Spectral analysis and computation for 6 homogenization of advection diffusion 7 processes in steady flows

9 Cite as: J. Math. Phys. 60, 000000 (2019); doi: 10.1063/1.5127457

10 Submitted: 29 April 2016 • Accepted: 3 September 2019 •

11 Published Online: XX XX XXXX



12 N. B. Murphy,^{1,2} J. Xin,¹ E. Cherkaev,² J. Zhu,² and K. M. Golden²

13 AFFILIATIONS

14 ¹Department of Mathematics, University of California at Irvine, 340 Rowland Hall, Irvine, California 92697-3875, USA

15 ²Department of Mathematics, University of Utah, 155 S 1400 E, RM 233, Salt Lake City, Utah 84112-0090, USA

16

17 ABSTRACT

18 Advection diffusion plays a key role in the transport of salt, heat, buoys, and markers in geophysical flows, in the dispersion of pollutants
19 and trace gases in the atmosphere, and even in the dynamics of sea ice floes influenced by winds and ocean currents. The long time, large
20 scale behavior of such systems is equivalent to an enhanced diffusion process with an effective diffusivity matrix \mathfrak{D}^* . Three decades ago, a
21 Stieltjes integral representation for the homogenized matrix, involving a spectral measure of a self-adjoint operator, was developed. However,
22 analytical calculations of \mathfrak{D}^* have been obtained for only a few simple flows, and numerical computations of the effective behavior based
23 on this spectral representation have apparently not been attempted. We overcome these limitations by providing a mathematical founda-
24 tion for the computation of Stieltjes integral representations of \mathfrak{D}^* . We explore two different approaches and for each approach we derive
25 new Stieltjes integral representations and rigorous bounds for the symmetric and antisymmetric parts of \mathfrak{D}^* , involving the molecular dif-
26 fusivity and a spectral measure μ of a self-adjoint operator that depends on the characteristics of a randomly perturbed periodic flow. In
27 discrete formulations of each approach, we express μ explicitly in terms of standard (or generalized) eigenvalues and eigenvectors of Hermitian
28 matrices. We develop and implement an efficient numerical algorithm that combines beneficial numerical attributes of each approach.
29 We use this method to compute the effective behavior for model flows and relate spectral characteristics to flow geometry and transport
30 properties.

31 Published under license by AIP Publishing. <https://doi.org/10.1063/1.5127457>

33 I. INTRODUCTION

34 The advective enhancement of diffusive transport of passive scalars by complex fluid flows plays a key role in many important processes
35 in the global climate system⁶³ and Earth's ecosystems.¹⁵ Advection by geophysical fluids intensifies the dispersion and large scale transport of
36 heat,⁴¹ pollutants,⁵⁵ and nutrients^{15,24} diffusing in their environment. Advective processes also enhance the large scale transport of plankton,²⁴
37 which is an important component of the food web that sustains life in the polar oceans. The transport of sea ice floes in the polar oceans is
38 diffusive in nature over short time scales as floes bump against each other, yet can be influenced and enhanced by eddy fluxes, storms, and
39 prevailing winds in the atmosphere as well as ocean currents.^{31,51,52,63,64} Thermal transport through sea ice, coupling the temperature field in
40 the upper ocean to the lower atmosphere, can be enhanced due to the presence of convective fluid flow in the porous brine microstructure of
41 sea ice.^{21,30,32,62}

42 It was discovered in the early 1900s⁶⁰ that complex fluid flows transport passive scalars in much the same way as molecular diffusion.
43 The mathematical description of this phenomenon⁶¹ demonstrated that the long time, large scale behavior of a diffusing particle or tracer
44 being advected by an *incompressible* fluid velocity field is equivalent to an enhanced diffusion process with an effective diffusivity matrix \mathfrak{D}^* .
45 Describing the enhancement of the effective transport properties by fluid advection is a challenging problem with theoretical and practical
46 importance in many fields of science and engineering, ranging from turbulent combustion^{2,12,50,59,65,66} to mass, heat, and salt transport in
47 geophysical flows.⁴¹

48 A broad range of mathematical techniques have been developed that reduce the analysis of complex fluid flows, with rapidly varying
49 structures in space and time, to solving averaged or *homogenized* equations that do not have rapidly varying data, but involve effective
50 parameters.^{11,17,18,33–35,48,66} Homogenization of the advection diffusion equation for passive scalar transport by stochastically stationary, time-
51 independent, *mean-zero* fluid velocity fields was treated in Ref. 35. This reduced the analysis of advective diffusion to solving a diffusion
52 equation involving a homogenized temperature field and a constant effective diffusivity matrix \mathfrak{D}^* .

53 An important consequence of this analysis is that the effective diffusivity \mathfrak{D}^* is given in terms of a solution of the so-called “cell
54 problem,”³⁵ which can be written as a steady state diffusion equation involving a skew-symmetric random matrix H .^{3,4,17,18} By adapting the
55 analytic continuation method of homogenization theory for composite materials,^{8,22,39} it was shown^{3,4} that the cell problem could be written
56 in resolvent form involving a self-adjoint random operator acting on the Hilbert space of *curl-free vector fields*. This, in turn, led to a Stieltjes
57 integral representation for the *symmetric* part of \mathfrak{D}^* , involving the Péclet number Pe of the flow and a *spectral measure* of the operator. A key
58 feature of the integral representation for \mathfrak{D}^* is that parameter information in Pe is *separated* from the geometry of the fluid velocity field. The
59 velocity field geometry is encoded in the spectral measure through its moments. This parameter separation has led^{3,4,17,18} to rigorous forward
60 bounds for the diagonal components of \mathfrak{D}^* .

61 The mathematical framework developed in Ref. 35 was adapted^{33,48} to the case of a periodic, time-dependent fluid velocity field with
62 *nonzero mean*. It was shown⁴⁸ that, depending on the strength of the fluctuations relative to the mean flow, the effective diffusivity matrix \mathfrak{D}^*
63 can be constant or a function of both space and time. When \mathfrak{D}^* is constant, only its symmetric part appears in the homogenized equation
64 as an enhancement in the diffusivity. However, when \mathfrak{D}^* is a function of space and time, its antisymmetric part also plays a key role in the
65 homogenized equation. Based on Refs. 9 and 10, the cell problem associated with a *time-independent* flow was transformed⁴⁸ into a resolvent
66 formula involving a self-adjoint operator, acting on a Sobolev space^{19,37} of spatially periodic *scalar fields*, which is also a Hilbert space. This, in
67 turn, led to a discrete Stieltjes integral representation for the *antisymmetric* part of \mathfrak{D}^* , involving the Péclet number of the flow and a spectral
68 measure of the operator.

69 Such methods have been extended to steady flows where particles diffuse according to linear collisions,⁴⁹ solute transport in porous
70 media,^{9,10} anelastic (weakly compressible) flows,³⁶ as well as to the setting of a time-dependent fluid velocity field.^{5,33,44} All these approaches
71 yield integral representations of the symmetric and, when appropriate, the antisymmetric part of \mathfrak{D}^* . Variational formulations of the effective
72 parameter problem for \mathfrak{D}^* are given in Refs. 4, 17, and 18.

73 We now discuss the main contributions of this work. In Refs. 3 and 4, a Stieltjes integral representation and the associated rigorous
74 bounds were developed for the diagonal components of \mathfrak{D}^* (which are components of the *symmetric* part of \mathfrak{D}^*); the off-diagonal components
75 were ignored. In Ref. 48, using a different method, a Stieltjes integral representation was developed for the off-diagonal components of the
76 *antisymmetric* part of \mathfrak{D}^* (the diagonal components are zero); no bounds were developed using the spectral representation. Here, we adapt
77 and extend the mathematical frameworks developed in Refs. 3, 4, and 48 to the case of a time-independent randomly perturbed periodic flow.
78 We obtain *new* Stieltjes integral representations and rigorous bounds for both the symmetric and antisymmetric parts of \mathfrak{D}^* —for both its
79 diagonal and off-diagonal components. These integral representations achieve a separation of the geometry of the fluid velocity—through the
80 spectral measures of self-adjoint operators—from the relevant material property of the fluid, its molecular diffusivity.

81 For each approach, we provide a mathematical foundation for the computation of Stieltjes integral representations for \mathfrak{D}^* , by developing
82 discrete, matrix formulations of the effective parameter problem. The spectral measure in each of these two approaches is given explicitly
83 in terms of the eigenvalues and eigenvectors of either a standard or generalized Hermitian eigenvalue problem. In general, the numerical
84 implementation of the generalized eigenvalue problem is more computationally expensive than a standard eigenvalue problem.⁴⁷ However,
85 the approach involving the standard problem involves a matrix that is larger by a factor of the dimension d compared to the matrix of the other
86 approach involving the generalized problem. The numerical eigenvalue decomposition of a matrix is quite expensive, and the high resolution
87 of the discretized domain results in very large matrices. Therefore, it is important to develop an efficient way to numerically compute the
88 spectral measure. We provide a detailed matrix analysis that demonstrates both approaches can be formulated in terms of a common *standard*
89 eigenvalue problem involving a matrix with the *smaller size* encountered in the generalized eigenvalue problem, thus combining beneficial
90 numerical attributes of both approaches.

91 In the continuum setting, the self-adjoint operators used in Refs. 3, 4, and 48 involve the inverse of the negative Laplacian $(-\Delta)^{-1}$, which
92 is given in terms of convolution with the Green’s function for $\Delta = \nabla^2$.⁵⁶ In the discrete setting, the negative matrix Laplacian is full-rank,
93 hence invertible when Dirichlet boundary conditions are considered, for example. However, the matrix Laplacian is rank-deficient, hence
94 noninvertible when periodic boundary conditions are considered. The matrix analysis discussed above in the full-rank setting reveals useful
95 structure with minimal effort. However, the matrix analysis of the rank-deficient setting is quite a bit more involved, but necessary, since here
96 we investigate advection enhanced diffusion by periodic flows. This analysis demonstrates that the two approaches considered yield equivalent
97 spectral representations for the effective diffusivity matrix \mathfrak{D}^* .

98 We utilize this unified mathematical framework to compute the effective diffusivity matrix \mathfrak{D}^* for some model periodic and randomly
99 perturbed periodic flows and describe the behavior of the enhancement of diffusive transport in terms of the behavior of the spectral measure.
100 There are several approaches to computing \mathfrak{D}^* , including numerical solutions of the underlying cell problem PDE,⁴⁸ Monte Carlo methods,¹³
101 and a method accurate for large Péclet numbers.²³ Our work here was not motivated by a goal of finding a faster or more accurate method of
102 computing \mathfrak{D}^* , although our approach does provide an alternative way of computing \mathfrak{D}^* and is quite robust.

103 Instead, for randomly perturbed periodic flows, our spectral method for computing \mathfrak{D}^* is set apart from more traditional methods
104 in that it was developed not only to study homogenized behavior but to investigate *spectral statistics*. Indeed, the effective behavior of the
105 system, as encapsulated by \mathfrak{D}^* , is closely connected to the statistical behavior of the spectral measure which, in turn, is determined by the

statistics of the random eigenvalues and eigenvectors. Consequently, the spectral method enables the homogenization of advection diffusion processes to be viewed through the lens of random matrix theory. In the theory of two-phase composite materials, this approach has led to a new understanding of critical behavior of transport in high contrast composite materials as a percolation threshold is approached. The focus on calculating spectral measures in Stieltjes representations for composite materials through computation of eigenvalues and eigenvectors of random matrices led to the realization that critical behavior of classical transport at a percolation threshold can be viewed as a type of Anderson transition.⁴⁵ In the analysis enabled by the spectral approach for composites, we investigated the appearance, for example, of localization phenomena, mobility edges, and universal Wigner-Dyson statistics of the Gaussian orthogonal ensemble for the eigenvalue spacing distribution. The results in this manuscript lay the mathematical and computational groundwork for such investigations in the context of advection diffusion processes, where the geometry of the fluid velocity field plays the role of the microstructural properties of the composite. Our results in this direction are somewhat outside the scope of this paper and will be published elsewhere, although we consider here some spectral characteristics and their relations to flow geometry and transport properties.

As another example of how this work enables applications to geophysics, we consider advection diffusion within sea ice. The enhancement of the effective thermal conductivity of sea ice due to the presence of convective fluid flow has long been known from an observational perspective.^{21,32,62} The authors are unaware, though, of any predictive, theoretical works on this enhancement. In Ref. 30, the effective thermal conductivity of sea ice in the presence of *bulk* fluid convection is investigated, by applying the results developed here. Using Stieltjes integral representations, a series of bounds on the effective thermal conductivity were obtained for model flows using Padé approximants and the analytic continuation method, in terms of the Péclet number.

Motivated by the theoretical findings in this work, in Ref. 44, we generalized the results given here to the setting of a time-dependent fluid velocity field $\mathbf{u} = \mathbf{u}(t, \mathbf{x})$. Furthermore, we used different abstract methods of functional analysis to generalize the equivalence results summarized in Theorem 5, Corollary 6, Lemma 9, and Theorem 10 of this work to the continuum, steady, and dynamic settings.

In order to streamline the presentation leading to the numerical results, we have placed in an appendix the development of integral representations for effective diffusivities using the approach introduced in Refs. 3 and 4—for both the continuum and discrete settings. The matrix analysis of the rank deficient setting and the equivalence results discussed above have also been placed in the appendix. Comments on the notation used throughout this manuscript are given in Appendix B.

II. HOMOGENIZATION OF THE ADVECTION DIFFUSION EQUATION

The dispersion of a passive scalar with density ϕ diffusing in a fluid with molecular diffusivity ε and being advected by a mean-zero incompressible velocity field \mathbf{u} satisfying $\nabla \cdot \mathbf{u} = 0$ and $\langle \mathbf{u} \rangle = 0$ is described by the advection diffusion equation

$$\phi_t(t, \mathbf{x}) = \mathbf{u}(\mathbf{x}) \cdot \nabla \phi(t, \mathbf{x}) + \varepsilon \Delta \phi(t, \mathbf{x}), \quad \phi(0, \mathbf{x}) = \phi_0(\mathbf{x}), \quad \mathbf{x} \in \mathbb{R}^d, \quad t > 0, \quad (1)$$

with initial density $\phi_0(\mathbf{x})$ given. Here, $\langle \cdot \rangle$ denotes volume averaging over the period cell \mathcal{V} , ϕ_t denotes partial differentiation of ϕ with respect to time t , $\Delta = \nabla \cdot \nabla = \nabla^2$ is the Laplacian, $\varepsilon > 0$, and d is the system dimension, and we denote by 0 the null element in all linear spaces in question. Moreover, $\xi \cdot \zeta = \xi^\dagger \zeta$ and \dagger is the operation of complex-conjugate-transpose, with $\xi \cdot \xi = |\xi|^2$. Later, we will extensively use this form of the dot product over complex fields, with built in complex conjugation. However, we emphasize that all quantities considered in this section are *real-valued*. We assume for now that the time-independent fluid velocity field \mathbf{u} is spatially periodic on the region $\mathcal{V} \subset \mathbb{R}^d$. Later, we will discuss the case of an array of randomly perturbed, periodic flows.

The long time, large scale dispersion of passive scalars can be described⁶¹ by an effective diffusivity matrix \mathfrak{D}^* . An explicit representation for \mathfrak{D}^* can be found using methods of homogenization theory.^{7,46} These methods have demonstrated that the averaged or *homogenized* behavior of the advection diffusion equation in (1) is determined by a diffusion equation involving an averaged scalar density $\bar{\phi}$ and a (constant) effective diffusivity matrix \mathfrak{D}^* ,³⁵

$$\bar{\phi}_t(t, \mathbf{x}) = \nabla \cdot [\mathfrak{D}^* \nabla \bar{\phi}(t, \mathbf{x})], \quad \bar{\phi}(0, \mathbf{x}) = \phi_0(\mathbf{x}). \quad (2)$$

The components \mathfrak{D}_{jk}^* , $j, k = 1, \dots, d$, of \mathfrak{D}^* are given by³⁵

$$\mathfrak{D}_{jk}^* = \varepsilon \delta_{jk} + \langle u_j \chi_k \rangle. \quad (3)$$

The function χ_j in (3) satisfies a cell problem which is a steady state advection diffusion equation with a forcing term involving u_j , the j th component of the fluid velocity field \mathbf{u} ,^{18,35}

$$\mathbf{u} \cdot \nabla \chi_j + \varepsilon \Delta \chi_j = -u_j, \quad \langle \nabla \chi_j \rangle = 0. \quad (4)$$

Equations (2)–(4) follow from the assumption that the length scale associated with spatial variations of the initial density ϕ_0 is much larger than the length scale of spatial variations associated with the fluid velocity field \mathbf{u} ^{18,35} (separation of scales). This information is incorporated into Eq. (1) by introducing a small dimensionless parameter $\delta \ll 1$ and writing³⁵

$$\phi(0, \mathbf{x}) = \phi_0(\delta \mathbf{x}). \quad (5)$$

154 Anticipating that ϕ will have diffusive dynamics as $t \rightarrow \infty$, space and time are rescaled by $x \mapsto x/\delta$ and $t \mapsto t/\delta^2$. As $\delta \rightarrow 0$, the associated
 155 solution $\phi^\delta(t, x) = \phi(t/\delta^2, x/\delta)$ of Eq. (1) (in the rescaled variables) converges to $\bar{\phi}(t, x)$ which satisfies Eq. (2). The convergence is in an L^2
 156 sense that depends on the technical assumptions made about the fluid velocity field \mathbf{u} .^{4,17,18,33,35,48}

157 We emphasize that the cell problem in (4) involves only the fast variable x/δ .³⁵ Other space-time scalings have also been considered,
 158 which have led to space-time dependent \mathfrak{D}^* ⁴⁸ and even anomalous diffusive dynamics.³³ Homogenization theorems for space-time dependent
 159 fluid velocity fields are treated in Refs. 11, 33, and 48.

160 In our analysis of the effective diffusivity matrix \mathfrak{D}^* , it is beneficial to use nondimensional parameters. We therefore assume that Eq. (1)
 161 has been nondimensionalized as follows: Let ℓ and τ be the typical length and time scales associated with the problem of interest. Mapping
 162 to the nondimensional variables $t \mapsto t/\tau$ and $x \mapsto x/\ell$, one finds that ϕ satisfies the advection diffusion equation in (1) with a nondimensional
 163 molecular diffusivity and fluid velocity field,

$$164 \quad \varepsilon \mapsto \tau\varepsilon/\ell^2, \quad \mathbf{u} \mapsto \tau\mathbf{u}/\ell. \quad (6)$$

165 This demonstrates that by nondimensionalizing Eq. (1), the fluid velocity field \mathbf{u} is, in turn, divided by a quantity with dimensions of
 166 velocity and the molecular diffusivity is divided by a quantity with dimensions of velocity multiplied by the spatial length. It is convenient to
 167 choose the rescaled \mathbf{u} and ε in a way that captures information about the fluid velocity field. However, it is also convenient to choose these
 168 rescaled variables in a way that separates the rescaled ε from the geometry of the flow; this leads to mathematically and physically meaningful
 169 properties of rigorous bounds for \mathfrak{D}^* which follow from the analytic structure of Stieltjes integral representations for \mathfrak{D}^* ^{4,6}—discussed in Sec.
 III.

170 We accomplish both of these goals as follows: Define the dimensional fluid velocity field by $\mathbf{u} = u_0\mathbf{v}$, where the parameter u_0 has dimensions
 171 of velocity and represents the “flow strength” of \mathbf{u} which is independent of the geometry of the flow; the flow geometry is encapsulated
 172 in the nondimensional vector field \mathbf{v} . With these definitions, we choose reference scales τ and ℓ in Eq. (6) to satisfy $u_0 = \ell/\tau$ so that $\mathbf{u} \mapsto \mathbf{v}$
 173 and $\varepsilon \mapsto \varepsilon/u_0\ell$. For example, in Sec. V, we compute \mathfrak{D}^* for BC-flow¹¹ having dimensional fluid velocity field $\mathbf{u} = u_0(C \cos y, B \cos x)$, where
 174 the flow strength $u_0 \in (0, \infty)$ is independent of the nondimensional parameters $B, C \in [0, 1]$ which determine the streamline geometry of \mathbf{u} .

175 An example of a nondimensional, parameter that compares the rate of scalar advection to the rate of diffusion is the Péclet number.
 176 We define it by the ratio $Pe = \ell u_0/\varepsilon$, although other definitions have been used.^{33,36} The advection and diffusion dominated regimes are
 177 characterized by $Pe \gg 1$ and $Pe \ll 1$, respectively. Therefore, our choice of the rescaled ε satisfies $Pe = 1/\varepsilon$.

178 The parameter separation between Pe and the geometry of the flow is important for rigorous upper and lower Padé approximant bounds
 179 for \mathfrak{D}^* .^{4,43} Padé approximants of \mathfrak{D}^* are given in terms of ratios of polynomials⁶ $P(z)/Q(z)$, where $z = Pe^2$, $0 < z < \infty$, and the coefficients
 180 of these polynomials depend on the moments of a spectral measure that, in turn, depend on the fluid velocity field \mathbf{u} .^{4,43} For example, when
 181 \mathbf{u} is given by BC-flow, the moments of the measure depend⁴³ on the parameters B and C . Our numerical investigations have shown if the
 182 nondimensionalization of Eq. (1) is chosen in a way that the variable z also depends on the flow geometry through the ratio B/C , then this
 183 gives rise⁴³ to positive real roots for the polynomials $P(z)$ and $Q(z)$. This, in turn, gives rise to positive real roots and poles in the (rigorous) Padé
 184 approximant bounds for \mathfrak{D}^* , which is not physically or mathematically consistent with the known behavior of \mathfrak{D}^* .^{11,17,33,48} This demonstrates
 185 the importance of parameter separation between z and the flow geometry for Padé approximant bounds for \mathfrak{D}^* .

186 This way of nondimensionalizing Eq. (1) is also convenient in the case of a time-dependent fluid velocity field,⁴⁴ where the parameter
 187 u_0 again represents the flow strength and the vector field \mathbf{v} encapsulates the geometric and dynamical properties of the flow. For example,
 188 the space-time periodic flow with velocity field $\mathbf{u} = u_0((C \cos y, B \cos x) + \cos t(y \sin y, \beta \sin x))$ has dynamical behavior exhibiting Lagrangian
 189 chaos.^{11,44} Here, the flow strength $u_0 \in (0, \infty)$ is independent of the parameters $B, C, y, \beta \in [0, 1]$ which determine the geometric and dynamical
 190 properties of \mathbf{u} . This choice of nondimensionalization gives a clearer interpretation of the advection and diffusion dominated regimes in terms
 191 of $Pe = 1/\varepsilon$ than that given in Ref. 44. A detailed discussion of various nondimensionalizations of Eq. (1) is given in Refs. 33 and 36.

192 III. HILBERT SPACE AND INTEGRAL REPRESENTATIONS

193 In this section, we adapt and extend a method^{9,10,48} which provides Stieltjes integral representations for the effective diffusivity matrix
 194 \mathfrak{D}^* . We do so by providing functional formulas for the symmetric \mathfrak{S}^* and antisymmetric \mathfrak{A}^* parts of \mathfrak{D}^* , involving the scalar field χ_j in
 195 Eq. (4). We also provide a Sobolev space formulation of the effective parameter problem⁴⁸ which yields a resolvent formula for χ_j , involving a
 196 self-adjoint operator that depends only on the fluid velocity field \mathbf{u} . This and the spectral theorem^{53,58} yield Stieltjes integral representations
 197 for \mathfrak{S}^* and \mathfrak{A}^* involving a spectral measure of the operator.

198 Consider the Hilbert space \mathcal{H} ,

$$199 \quad \mathcal{H} = \{f \in L^2(\mathcal{V}, v) : f(x) \text{ is periodic in } \mathcal{V} \text{ and } \langle f \rangle = 0\}, \quad (7)$$

200 where v is the Lebesgue measure on \mathbb{R}^d , restricted to \mathcal{V} , and the σ -algebra associated with the underlying measure space is generated by the
 201 Lebesgue measurable subsets of \mathbb{R}^d . The Hilbert space \mathcal{H} is equipped with a sesquilinear inner product $\langle \cdot, \cdot \rangle$ defined by $\langle f, h \rangle = \langle \bar{f} h \rangle$, with
 202 $\langle h, f \rangle = \overline{\langle f, h \rangle}$ for $f, h \in \mathcal{H}$, which induces a norm $\| \cdot \|$ defined by $\| f \| = \langle f, f \rangle^{1/2}$ and $f \in \mathcal{H}$ implies $\| f \| < \infty$.

203 One could also consider a random fluid flow filling all of \mathbb{R}^d , with a velocity field \mathbf{u} determined by the probability space (Ω, P) with
 204 σ -algebra generated by the sets $\{\mathbf{u}(x) \in B\}$, where $x \in \mathbb{R}^d$ and B is a Borel subset of \mathbb{R}^d .⁴ Here, Ω is the set of all geometric realizations of \mathbf{u} ,
 205 which is indexed by the parameter $\omega \in \Omega$ representing one particular geometric realization, and P is the associated probability measure. The
 206 underlying Hilbert space in this case can be taken to be $\mathcal{H} = L^2(\Omega, P)$, i.e., the space of all P -measurable complex-valued scalar functions ξ

satisfying $\|\xi\| = \langle |\xi|^2 \rangle^{1/2} < \infty$, where $\langle \cdot \rangle$ denotes ensemble averaging and the underlying sesquilinear inner-product is defined by $\langle \xi, \zeta \rangle = \langle \bar{\xi} \zeta \rangle$. In this case, one could consider a random fluid flow with a velocity field \mathbf{u} that is stationary³⁵ or ergodic,^{3,4} for example, with regularity conditions at infinity, i.e., as $|\mathbf{x}| \rightarrow \infty$. In these cases, one works with an infinite medium directly, which presents substantial computational difficulties.

A more computationally tractable random system is given by an $n \times n$ array of randomly perturbed periodic flows.¹⁸ In this case, the σ -algebra associated with the underlying probability space is generated by the Lebesgue measurable subsets of \mathbb{R}^d . Here, the Hilbert space \mathcal{H} is given by Eq. (7) and the averaged quantities depend on the realization of the random medium because $\langle \cdot \rangle$ is given by volume averaging over the period cell \mathcal{V} .¹⁸ The effective diffusivity matrix \mathfrak{D}^* is obtained by taking an infinite volume limit, $\mathfrak{D}^* = \lim_{n \rightarrow \infty} \mathfrak{D}_n^*$, of the finite volume effective diffusivity matrix \mathfrak{D}_n^* and evoking an ergodic theorem.^{18,22} Numerically, by the law of large numbers,¹⁶ it is natural to spatially average each statistical trial and then ensemble average over all of the sampled random realizations. This is the approach we take here.

In any case, once the Hilbert space \mathcal{H} is established, with associated average $\langle \cdot \rangle$, inner-product $\langle \cdot, \cdot \rangle$, and norm $\|\cdot\|$, the spectral theory presented in the remainder of this section progresses independent of the underlying details, as it lays on an axiomatic foundation.⁵⁸ For the sake of numerical tractability, we will assume that the Hilbert space \mathcal{H} is given by Eq. (7). The fluid velocity field \mathbf{u} can be assumed to represent a periodic or randomly perturbed periodic flow. Now, consider the Sobolev space $\mathcal{H}^{1,2}$, which itself is a Hilbert space,^{9,10}

$$\mathcal{H}^{1,2} = \{f \in \mathcal{H} : \|f\|_{1,2} < \infty, \langle f \rangle = 0\}, \quad \|f\|_{1,2} = \langle |\nabla f|^2 \rangle^{1/2}, \quad (8)$$

where $\|\cdot\|_{1,2}$ is the norm induced by the underlying sesquilinear inner-product $\langle \cdot, \cdot \rangle_{1,2}$ defined by $\langle f, h \rangle_{1,2} = \langle \nabla f \cdot \nabla h \rangle$, with $\langle h, f \rangle_{1,2} = \langle f, h \rangle_{1,2}$ (recall $\xi \cdot \zeta = \xi^\dagger \zeta$ includes complex conjugation).

Recall the definition of the components $\mathfrak{D}_{jk}^* = \varepsilon \delta_{jk} + \langle u_j \chi_k \rangle$, $j, k = 1, \dots, d$, of the effective diffusivity matrix \mathfrak{D}^* in (3). Rewrite the functional $\langle u_j \chi_k \rangle$ as⁴⁸

$$\langle u_j \chi_k \rangle = \langle [\Delta \Delta^{-1} u_j] \chi_k \rangle = -\langle \nabla \Delta^{-1} u_j \cdot \nabla \chi_k \rangle = -\langle \Delta^{-1} u_j, \chi_k \rangle_{1,2}, \quad (9)$$

where we have integrated by parts and used the periodicity of the functions u_j and χ_k . Here, Δ^{-1} is based on convolution with the Green's function for the Laplacian Δ .⁵⁶ The symmetric \mathfrak{S}^* and antisymmetric \mathfrak{A}^* parts of the effective diffusivity matrix \mathfrak{D}^* are defined by

$$\mathfrak{D}^* = \mathfrak{S}^* + \mathfrak{A}^*, \quad \mathfrak{S}^* = \frac{1}{2} (\mathfrak{D}^* + [\mathfrak{D}^*]^T), \quad \mathfrak{A}^* = \frac{1}{2} (\mathfrak{D}^* - [\mathfrak{D}^*]^T). \quad (10)$$

Substituting into Eq. (9) the expression $-u_j = \mathbf{u} \cdot \nabla \chi_j + \varepsilon \Delta \chi_j$ for $-u_j$ in (4) yields the following functional formulas for the components \mathfrak{S}_{jk}^* and \mathfrak{A}_{jk}^* , $j, k = 1, \dots, d$, of \mathfrak{S}^* and \mathfrak{A}^* ,

$$\mathfrak{S}_{jk}^* = \varepsilon (\delta_{jk} + \langle \chi_j, \chi_k \rangle_{1,2}), \quad \mathfrak{A}_{jk}^* = \langle A \chi_j, \chi_k \rangle_{1,2}, \quad A = \Delta^{-1} [\mathbf{u} \cdot \nabla]. \quad (11)$$

Due to the incompressibility of the fluid velocity field, $\nabla \cdot \mathbf{u} = 0$, the operator A is antisymmetric on $\mathcal{H}^{1,2}$, i.e., $\langle A \xi, \zeta \rangle_{1,2} = -\langle \xi, A \zeta \rangle_{1,2}$ for all $\xi, \zeta \in \mathcal{H}^{1,2}$ [see Eq. (C1)]. Since the scalar fields χ_j and $A \chi_j$ are *real-valued*, we have that $\langle \chi_j, \chi_k \rangle_{1,2} = \langle \chi_k, \chi_j \rangle_{1,2}$ and $\mathfrak{A}_{kj}^* = \langle A \chi_k, \chi_j \rangle_{1,2} = -\langle \chi_k, A \chi_j \rangle_{1,2} = -\langle A \chi_j, \chi_k \rangle_{1,2} = -\mathfrak{A}_{jk}^*$, confirming that \mathfrak{S}^* is symmetric and \mathfrak{A}^* is antisymmetric, with $\mathfrak{A}_{kk}^* = 0$.

Applying the operator Δ^{-1} to both sides of the cell problem $\varepsilon \Delta \chi_j + \mathbf{u} \cdot \nabla \chi_j = -u_j$ in Eq. (4) yields the following resolvent formula for χ_j involving the operator A in (11):

$$\chi_j = (\varepsilon + A)^{-1} g_j, \quad g_j = (-\Delta)^{-1} u_j. \quad (12)$$

Substituting the resolvent formula for χ_j in (12) into the bilinear functionals in Eq. (11) yields

$$\begin{aligned} \mathfrak{S}_{jk}^* &= \varepsilon (\delta_{jk} + \langle (\varepsilon + A)^{-1} g_j, (\varepsilon + A)^{-1} g_k \rangle_{1,2}), \\ \mathfrak{A}_{jk}^* &= \langle A (\varepsilon + A)^{-1} g_j, (\varepsilon + A)^{-1} g_k \rangle_{1,2}. \end{aligned} \quad (13)$$

Since \mathcal{V} is a bounded domain, the linear operator Δ^{-1} is bounded on \mathcal{H} with bounded operator norm $\|\Delta^{-1}\| < \infty$.⁵⁶ When $|\mathbf{u}|$ is uniformly bounded on the period cell \mathcal{V} , $\sup_{x \in \mathcal{V}} |\mathbf{u}(x)| < \infty$, the linear operator A is bounded on $\mathcal{H}^{1,2}$, with [see Eqs. (C2) and (C3)]

$$\|A\|_{1,2} \leq [\|\Delta^{-1}\| \sup_{x \in \mathcal{V}} |\mathbf{u}(x)|^2]^{1/2} < \infty, \quad (14)$$

where $\|A\|_{1,2}$ denotes the operator norm of A induced by the norm $\|\cdot\|_{1,2}$ in Eq. (8). All of the fluid velocity fields that we consider in our numerical computations of \mathfrak{D}^* in Sec. V are uniformly bounded. More generally, for $u_k \in \mathcal{H}$, $k = 1, \dots, d$, the operator A is compact on $\mathcal{H}^{1,2}$,^{9,10,48} hence bounded.⁵⁶ Consequently, $M = -iA$, where $i = \sqrt{-1}$, is a bounded linear operator on $\mathcal{H}^{1,2}$ with $\|M\|_{1,2} = \|A\|_{1,2} < \infty$. Moreover, the skew-symmetry of A and the sesquilinearity of the $\mathcal{H}^{1,2}$ -inner-product imply that M is also symmetric, $\langle Mf, h \rangle_{1,2} = \langle f, Mh \rangle_{1,2}$. The bounded linear symmetric operator M with domain $\mathcal{H}^{1,2}$ is *self-adjoint*.^{53,58}

250 The spectrum Σ of the self-adjoint operator M is real-valued, with the spectral radius equal to its operator norm,⁵³ i.e.,

$$251 \quad \Sigma \subseteq [-\|A\|_{1,2}, \|A\|_{1,2}]. \quad (15)$$

252 The spectral theorem for bounded linear self-adjoint operators in Hilbert space states that there is a one-to-one correspondence between the
253 operator M and a family of self-adjoint projection operators $\{Q(\lambda)\}_{\lambda \in \Sigma}$ —the resolution of the identity—satisfying⁵⁸

$$254 \quad \lim_{\lambda \rightarrow -\inf \Sigma} Q(\lambda) = 0, \quad \lim_{\lambda \rightarrow \sup \Sigma} Q(\lambda) = I. \quad (16)$$

255 Furthermore, for all $\xi, \zeta \in \mathcal{H}^{1,2}$, the *complex-valued* function of the spectral variable λ defined by $\mu_{\xi\zeta}(\lambda) = \langle Q(\lambda)\xi, \zeta \rangle_{1,2}$ has real and imaginary
256 parts that are of bounded variation.⁵⁸ Therefore, there is a *complex* Stieltjes measure $\mu_{\xi\zeta}$ associated with $\mu_{\xi\zeta}(\lambda)$.^{20,57,58}

257 The spectral theorem also states, for all complex-valued functions $f \in L^2(\mu_{\xi\zeta})$ and $h \in L^2(\mu_{\xi\zeta})$, there exist linear operators denoted by
258 $f(M)$ and $h(M)$ which are defined in terms of the bilinear functional $\langle f(M)\xi, h(M)\zeta \rangle_{1,2}$.⁵⁸ In particular, this functional has the following
259 Radon–Stieltjes integral representation involving the Stieltjes measure $\mu_{\xi\zeta}$, for all $\xi, \zeta \in \mathcal{H}^{1,2}$:

$$260 \quad \langle f(M)\xi, h(M)\zeta \rangle_{1,2} = \int_{-\infty}^{\infty} \bar{f}(\lambda) h(\lambda) d\mu_{\xi\zeta}(\lambda), \quad \mu_{\xi\zeta}(\lambda) = \langle Q(\lambda)\xi, \zeta \rangle_{1,2}, \quad (17)$$

261 where the integration is over the spectrum Σ of M ^{53,58} and \bar{f} denotes the complex conjugation of the scalar function f . Since the Stieltjes
262 measure $\mu_{\xi\zeta}$ has the property⁵⁸ $\int_a^b d\mu_{\xi\zeta}(\lambda) = \mu_{\xi\zeta}(b) - \mu_{\xi\zeta}(a)$, Eq. (16) implies that the mass $\mu_{\xi\zeta}^0$ of the measure $\mu_{\xi\zeta}$ is given by

$$263 \quad 264 \quad \mu_{\xi\zeta}^0 = \int_{-\infty}^{\infty} d\mu_{\xi\zeta}(\lambda) = \int_{-\infty}^{\infty} d\langle Q(\lambda)\xi, \zeta \rangle_{1,2} = \langle \xi, \zeta \rangle_{1,2}, \quad (18)$$

265 which is bounded in the sense that $|\mu_{\xi\zeta}^0| \leq \|\xi\|_{1,2} \|\zeta\|_{1,2} < \infty$ for all $\xi, \zeta \in \mathcal{H}^{1,2}$. Due to the sesquilinearity of the inner-product and the fact
266 that the projection operator $Q(\lambda)$ is self-adjoint on $\mathcal{H}^{1,2}$, the complex-valued function $\mu_{\xi\zeta}(\lambda)$ satisfies $\mu_{\xi\zeta}(\lambda) = \bar{\mu}_{\xi\zeta}(\lambda)$ and $\mu_{\xi\zeta}(\lambda) = \|Q(\lambda)\xi\|^2$,
267 so $\mu_{\xi\zeta}$ is a *positive* measure. The formulas in Eqs. (16)–(18) will be used several times throughout this manuscript to clarify and streamline
268 the development of various Stieltjes integral representations for the effective diffusivity matrix \mathfrak{D}^* . They will be used both in the continuum
269 setting and the discrete setting, which leads to an efficient numerical algorithm for our computation of spectral representations for \mathfrak{D}^* for
270 various model fluid flows in Sec. V.

271 We are now ready to present the main results of this section. For notational simplicity, denote the complex-valued function
272 $\mu_{jk}(\lambda) = \langle Q(\lambda)g_j, g_k \rangle$, instead of $\mu_{g_j g_k}(\lambda)$, where $g_j = (-\Delta)^{-1} u_j$ is defined in (12). Denote the real and imaginary parts of the function $\mu_{jk}(\lambda)$
273 by $\text{Re } \mu_{jk}(\lambda)$ and $\text{Im } \mu_{jk}(\lambda)$, respectively.

274 **Theorem 1.** Let $Q(\lambda)$ denote the resolution of the identity corresponding to the self-adjoint operator M . Then, the components \mathfrak{S}_{jk}^* and \mathfrak{A}_{jk}^* ,
275 $j, k = 1, \dots, d$, of the symmetric \mathfrak{S}^* and antisymmetric \mathfrak{A}^* parts of the effective diffusivity matrix \mathfrak{D}^* have the following  Radon–Stieltjes integral
276 representations:

$$277 \quad \mathfrak{S}_{jk}^* = \varepsilon \left(\delta_{jk} + \int_{-\infty}^{\infty} \frac{d\text{Re } \mu_{jk}(\lambda)}{\varepsilon^2 + \lambda^2} \right), \quad \mathfrak{A}_{jk}^* = \int_{-\infty}^{\infty} \frac{\lambda d\text{Im } \mu_{jk}(\lambda)}{\varepsilon^2 + \lambda^2}. \quad (19)$$

278 For $j \neq k$, $\text{Re } \mu_{jk}$ and $\text{Im } \mu_{jk}$ are signed measures.²⁰ For $j = k$, $\text{Re } \mu_{kk} = \mu_{kk}$ is a positive measure²⁰, which demonstrates that the effective transport
279 of the scalar density ϕ is enhanced by the presence of an incompressible fluid velocity field \mathbf{u} , above the bare diffusive value ε ,

$$280 \quad \mathfrak{S}_{kk}^* = \varepsilon \left(1 + \int_{-\infty}^{\infty} \frac{d\mu_{kk}(\lambda)}{\varepsilon^2 + \lambda^2} \right) \geq \varepsilon. \quad (20)$$

281 The mass μ_{jk}^0 of the measure μ_{jk} is real-valued and satisfies

$$282 \quad \mu_{jk}^0 = \langle [(-\Delta)^{-1} u_j] u_k \rangle, \quad |\mu_{jk}^0| \leq \|\Delta^{-1} u_j\| \|u_k\| < \infty. \quad (21)$$

283 *Proof of Theorem 1.* We first provide integral representations for the bilinear functional formulas in Eq. (13) for \mathfrak{S}_{jk}^* and \mathfrak{A}_{jk}^* . Since
284 we have already established the operator M is self-adjoint, we only need to identify the appropriate functions $f(\lambda)$ and $h(\lambda)$ as well as the
285 Hilbert space members $\xi, \zeta \in \mathcal{H}^{1,2}$ in (17). Using $A = \imath M$, comparison of the functionals in Eqs. (13) and (17) identifies $f(\lambda) = h(\lambda) = (\varepsilon + \imath\lambda)^{-1}$
286 for the first formula in (13), while $f(\lambda) = \imath\lambda(\varepsilon + \imath\lambda)^{-1}$ and $h(\lambda) = (\varepsilon + \imath\lambda)^{-1}$ for the second formula, with $\xi = g_j$ and $\zeta = g_k$ for both of these
287 formulas.

Now we just need to verify $f, h \in L^2(\mu_{kk})$ for all $k = 1, \dots, d$ and $0 < \varepsilon < \infty$. From Eq. (18), the mass μ_{jk}^0 of the measure μ_{jk} is given by $\mu_{jk}^0 = \langle g_j, g_k \rangle_{1,2} = \langle \nabla \Delta^{-1} u_j \cdot \nabla \Delta^{-1} u_k \rangle$. Integration by parts and the Cauchy-Schwartz inequality²⁰ then yield Eq. (21). In particular, $|\mu_{kk}^0| \leq \|\Delta^{-1}\| \|u_k\|^2 < \infty$, as Δ^{-1} has bounded operator norm $\|\Delta^{-1}\|$ on $L^2(\mathcal{V})$.⁵⁶ Consequently, since $0 < (\varepsilon^2 + \lambda^2)^{-1} \leq 1/\varepsilon^2 < \infty$ and $0 < \lambda^2(\varepsilon^2 + \lambda^2)^{-1} < 1$ for all $0 < \varepsilon < \infty$, it is clear that $f, h \in L^2(\mu_{kk})$. Consequently, the spectral theorem in (17) implies that the functional formulas for \mathfrak{S}_{jk}^* and \mathfrak{A}_{jk}^* in Eq. (13) have the following Stieltjes integral representations:

$$\mathfrak{S}_{jk}^* = \varepsilon \left(\delta_{jk} + \int_{-\infty}^{\infty} \frac{d\mu_{jk}(\lambda)}{\varepsilon^2 + \lambda^2} \right), \quad \mathfrak{A}_{jk}^* = - \int_{-\infty}^{\infty} \frac{i\lambda d\mu_{jk}(\lambda)}{\varepsilon^2 + \lambda^2}, \quad (22)$$

which involve the *complex measure* μ_{jk} .

We now show how the integrals for \mathfrak{S}_{jk}^* and \mathfrak{A}_{jk}^* in (22) can be represented in terms of the *signed measures* $\text{Re } \mu_{jk}$ and $\text{Im } \mu_{jk}$. Since ε, χ_k, u_k , and g_k in (13) are *real-valued*, we have from (12) the following symmetry conditions:

$$\begin{aligned} \langle (\varepsilon I + A)^{-1} g_j, (\varepsilon I + A)^{-1} g_k \rangle_{1,2} &= \langle (\varepsilon I + A)^{-1} g_k, (\varepsilon I + A)^{-1} g_j \rangle_{1,2}, \\ \langle A (\varepsilon I + A)^{-1} g_j, (\varepsilon I + A)^{-1} g_k \rangle_{1,2} &= \langle (\varepsilon I + A)^{-1} g_k, A (\varepsilon I + A)^{-1} g_j \rangle_{1,2}. \end{aligned} \quad (23)$$

These symmetries, the sesquilinearity of the \mathcal{H} -inner-product, the linearity⁵⁸ of the Stieltjes integrals in Eq. (22) with respect to the function $\mu_{jk}(\lambda)$, and the two identities $\text{Re } \mu_{jk}(\lambda) = (\mu_{jk}(\lambda) + \bar{\mu}_{jk}(\lambda))/2$ and $\text{Im } \mu_{jk}(\lambda) = (\mu_{jk}(\lambda) - \bar{\mu}_{jk}(\lambda))/(2i)$ yield Eq. (19). This concludes our Proof of Theorem 1. \square

Theorem 2. Let Σ denote the spectrum of the operator M , denote $\lambda_+ = \sup_{\lambda \in \Sigma} |\lambda|$, and assume $0 < \varepsilon < \infty$. Then, the diagonal components $\mathfrak{S}_{kk}^* = \mathfrak{D}_{kk}^*$ of the effective diffusivity matrix satisfy the following, rigorous upper⁴ and lower bounds:

$$\varepsilon [1 + \mu_{kk}^0 / (\varepsilon^2 + \lambda_+^2)] \leq \mathfrak{S}_{kk}^* \leq \varepsilon [1 + \mu_{kk}^0 / \varepsilon^2]. \quad (24)$$

For $j \neq k$, let $\text{Re } \mu_{jk} = \text{Re } \mu_{jk}^+ - \text{Re } \mu_{jk}^-$ and $\text{Im } \mu_{jk} = \text{Im } \mu_{jk}^+ - \text{Im } \mu_{jk}^-$ denote the Jordan decomposition of the signed measures $\text{Re } \mu_{jk}$ and $\text{Im } \mu_{jk}$, respectively, and denote the total variation of these measures by $|\text{Re } \mu|_{jk} = \text{Re } \mu_{jk}^+ + \text{Re } \mu_{jk}^-$ and $|\text{Im } \mu|_{jk} = \text{Im } \mu_{jk}^+ + \text{Im } \mu_{jk}^-$, respectively. Finally, denote the masses of the measures $\text{Re } \mu_{jk}^+$, $\text{Re } \mu_{jk}^-$, and $|\text{Im } \mu|_{jk}$ by $[\text{Re } \mu_{jk}^+]^0$, $[\text{Re } \mu_{jk}^-]^0$, and $|\text{Im } \mu|_{jk}^0$, respectively. Then, the off-diagonal components \mathfrak{S}_{jk}^* and \mathfrak{A}_{jk}^* , $j \neq k$, satisfy the following, rigorous upper and lower bounds:

$$\varepsilon \frac{[\text{Re } \mu_{jk}^+]^0}{\varepsilon^2 + \lambda_+^2} - \frac{[\text{Re } \mu_{jk}^-]^0}{\varepsilon} \leq \mathfrak{S}_{jk}^* \leq \frac{[\text{Re } \mu_{jk}^+]^0}{\varepsilon} - \varepsilon \frac{[\text{Re } \mu_{jk}^-]^0}{\varepsilon^2 + \lambda_+^2}, \quad j \neq k, \quad (25)$$

$$-\frac{\lambda_+ |\text{Im } \mu|_{jk}^0}{\varepsilon^2} \leq \mathfrak{A}_{jk}^* \leq \frac{\lambda_+ |\text{Im } \mu|_{jk}^0}{\varepsilon^2}, \quad j \neq k. \quad (26)$$

Proof of Theorem 2. Assume that $0 < \varepsilon < \infty$. From Eq. (15), the spectrum Σ of the compact^{9,10,33} operator $M = -iA$ is a bounded subset of \mathbb{R} . The spectrum is discrete⁵⁶ away from the spectral origin $\lambda = 0$ and comes in \pm pairs⁴⁸ with an accumulation point at $\lambda = 0$.⁵⁶ Denote $\lambda_+ = \sup_{\lambda \in \Sigma} |\lambda|$ and note that $\inf_{\lambda \in \Sigma} \lambda^2 = 0$. The inequalities $1/(\varepsilon^2 + \lambda_+^2) \leq 1/(\varepsilon^2 + \lambda^2) \leq 1/\varepsilon^2$ hold for all $\lambda \in \Sigma$. Consequently, since μ_{kk} is a positive measure with finite mass μ_{kk}^0 , the inequalities in (24) hold.²⁰ It may happen that $\mu_{kk}^0 = 0$, hence $\mathfrak{S}_{kk}^* = \varepsilon$, e.g., shear flow orthogonal to the k th direction.^{4,17}

When $j \neq k$, $\text{Re } \mu_{jk}$ is a signed measure. By the Jordan decomposition of $\text{Re } \mu_{jk}$, there are unique, positive measures $\text{Re } \mu_{jk}^+$ and $\text{Re } \mu_{jk}^-$ such that $\text{Re } \mu_{jk} = \text{Re } \mu_{jk}^+ - \text{Re } \mu_{jk}^-$. Moreover, associated with the signed measure, $\text{Re } \mu_{jk}$ is its total variation $|\text{Re } \mu|_{jk}$,²⁰

$$\text{Re } \mu_{jk} = \text{Re } \mu_{jk}^+ - \text{Re } \mu_{jk}^-, \quad |\text{Re } \mu|_{jk} = \text{Re } \mu_{jk}^+ + \text{Re } \mu_{jk}^-. \quad (27)$$

From Eq. (21), the measures $\text{Re } \mu_{jk}^+$ and $\text{Re } \mu_{jk}^-$ have bounded mass, which we denote $[\text{Re } \mu_{jk}^+]^0$ and $[\text{Re } \mu_{jk}^-]^0$, respectively; thus, the mass $|\text{Re } \mu|_{jk}^0$ of the measure $|\text{Re } \mu|_{jk}$ is also bounded. Since we have²⁰ that $|\mathfrak{S}_{jk}^*| \leq \int d|\text{Re } \mu|_{jk}(\lambda)/(\varepsilon^2 + \lambda^2)$, the upper bound in Eq. (24) with μ_{kk}^0 replaced by $|\text{Re } \mu|_{jk}^0$ holds for the positive quantity $|\mathfrak{S}_{jk}^*|$. These bounds for \mathfrak{S}_{jk}^* can be improved upon by separately considering the positive and negative contributions of the integral representation for \mathfrak{S}_{jk}^* , yielding Eq. (25). In a similar way, we obtain the bounds for \mathfrak{A}_{jk}^* in Eq. (26). This concludes our Proof of Theorem 2. \square

We conclude this section by noting that bounds on \mathfrak{S}_{kk}^* can also be obtained using variational methods^{4,17,18} as well as Padé approximants^{4,6} of Stieltjes functions.

329 **IV. DISCRETE SETTING: SOBOLEV SPACE OF SCALAR FIELDS**

330 For our numerical computations of the effective diffusivity \mathfrak{D}^* in Sec. V, we consider a discrete approximation of the cell problem
 331 in Eq. (4) written as $(\varepsilon + \imath M)\chi_j = g_j$. Here, $M = -\imath A$, $A = \Delta^{-1}[\mathbf{u} \cdot \nabla]$, and $g_j = -\Delta^{-1}u_j$, as defined in Eqs. (11) and (12). In this section, we
 332 manipulate these formulas in order to develop a numerical algorithm which enables numerical computations of \mathfrak{D}^* by directly computing a
 333 discrete representation of the spectral measure μ_{jk} in Eq. (19), in terms of the eigenvalues and eigenvectors of a *generalized* eigenvalue problem.
 334 This is not a trivial extension of the spectral theory for the continuum setting discussed in Sec. III, as the matrix representation of the operator
 335 $(-\Delta)^{-1}[\mathbf{u} \cdot \nabla]$ is *not* Hermitian. The special structure of the generalized eigenvalue problem itself makes these matrix operators Hermitian
 336 only with respect to a discrete Sobolev-like inner-product analogous to the inner-product $\langle \cdot, \cdot \rangle_{1,2}$ introduced after Eq. (8). Moreover, the
 337 eigenvector orthogonality is only with respect to this inner-product.

338 Towards this goal, we begin by noting that since $\mathbf{u}(x)$ is incompressible, $\nabla \cdot \mathbf{u} = 0$, there is a real (nondimensional) *antisymmetric* matrix
 339 $H(x)$ ^{3,4} such that

$$340 \quad \mathbf{u} = \nabla \cdot H, \quad H^T = -H, \quad (28)$$

341 where H^T denotes transposition of the matrix H . Due to the antisymmetry of the matrix H in Eq. (28) and the symmetry of the Hessian
 342 operator $\nabla \nabla$ when acting on a sufficiently smooth space of functions, we have $H: \nabla \nabla \varphi = 0$ for all such smooth functions φ , where  denotes
 343 matrix contraction. Consequently, $\nabla \cdot [H \nabla \varphi] = [\nabla \cdot H] \cdot \nabla \varphi + H: \nabla \nabla \varphi = [\nabla \cdot H] \cdot \nabla \varphi$, or

$$344 \quad \nabla \cdot [H \nabla] = [\nabla \cdot H] \cdot \nabla, \quad (29)$$

345 as operators acting on such functions. With (29) we can write the operator $M = \imath(-\Delta)^{-1}[\mathbf{u} \cdot \nabla]$ as $M = \imath(-\Delta)^{-1}\nabla \cdot [H \nabla]$.

346 We now discuss our discrete formulation of the effective parameter problem, which leads to Stieltjes integral representations for the
 347 symmetric \mathfrak{S}^* and antisymmetric \mathfrak{A}^* components of the effective diffusivity matrix \mathfrak{D}^* , involving a discrete spectral measure. For notational
 348 brevity, assume that the period cell \mathcal{V} is square. In the discrete setting,⁴² \mathcal{V} is represented by a square grid of size L , which is bijectively mapped
 349 to a vector with L^d components. The functions $u_j(x)$ and $\chi_j(x)$ are mapped to vectors \mathbf{u}_j and χ_j with L^d components, respectively, and the
 350 matrix $H(x)$ is mapped to a square banded antisymmetric matrix of size $N = L^d d$ (see Sec. V A for details). For simplicity, we will not make a
 351 notational distinction for H between the discrete and continuum settings, as the context will be clear.

352 The differential operator ∇ is represented by a finite difference matrix ∇ ,^{14,42} where $\nabla^T = (\nabla_1^T, \dots, \nabla_d^T)$ and ∇_j , $j = 1, \dots, d$, are also
 353 finite difference matrices. Moreover, the divergence operator $\nabla \cdot$ is given by $-\nabla^T$ and the matrix representation of the negative Lapla-
 354 cian $-\Delta$ is given by $\nabla^T \nabla$. Consequently, we may write the discrete, matrix representation M of the self-adjoint operator $M = \imath(-\Delta)^{-1}\nabla \cdot$
 355 $[H \nabla]$ as $M = (\nabla^T [-\imath \nabla^T H \nabla])$. This composition of the Hermitian matrix $-\imath \nabla^T H \nabla$ and the real-symmetric matrix $(\nabla^T)^{-1}$ is nei-
 356 ther real-symmetric nor Hermitian symmetric. From Eq. (C1), we see that the symmetry properties of the integrodiffer-
 357 ent operator M depend intimately on the inner-product $\langle f, h \rangle_{1,2} = \langle \nabla f \cdot \nabla h \rangle$ of the underlying Sobolev space $\mathcal{H}^{1,2}$ defined in Eq. (8). Therefore,
 358 we anticipate that the properties of this inner-product must be incorporated into the discrete formulation of integral representations
 for \mathfrak{D}^* .

359 We now provide a matrix formulation of the effective parameter problem introduced in Sec. III, which involves a *generalized eigenvalue*
 360 problem that has the Sobolev-type inner-product as a central feature. In particular, this formulation retains the key properties of the weak form
 361 of the eigenvalue problem $\langle M\varphi_n, \varphi_n \rangle_{1,2} = \lambda_n$. Namely, the operator M is self-adjoint with respect to the inner-product $\langle \cdot, \cdot \rangle_{1,2}$, its eigenfunctions
 362 $\varphi_n \in \mathcal{H}^{1,2}$ are orthonormal $\langle \varphi_n, \varphi_m \rangle_{1,2} = \delta_{nm}$, $n, m = 1, 2, 3, \dots$, with respect to the inner-product $\langle \cdot, \cdot \rangle_{1,2}$, and the spectrum Σ of M is real valued,
 363 $\Sigma \subset \mathbb{R}$. Toward this goal, consider the eigenvalue problem $M\varphi_n = \lambda_n\varphi_n$ in the following “strong” form:

$$364 \quad \imath \nabla \cdot [H \nabla \varphi_n] = \lambda_n(-\Delta)\varphi_n. \quad (30)$$

365 Using a discrete version of Eq. (30), we will establish the integral representations in (19) for discrete versions of the functionals
 366 $\mathfrak{S}_{jk}^* = \varepsilon(\delta_{jk} + \langle \chi_j, \chi_k \rangle_{1,2})$ and $\mathfrak{A}_{jk}^* = \langle \imath M\chi_j, \chi_k \rangle_{1,2}$ in (11), involving a discrete spectral measure.

367 By our discussion in this section, the matrix representation of the eigenvalue problem in (30) is

$$368 \quad Bz_n = \lambda_n Cz_n, \quad B = -\imath \nabla^T H \nabla, \quad C = \nabla^T \nabla. \quad \text{ $$

369 The first formula in Eq. (31) is a *generalized eigenvalue problem*⁴⁷ associated with the pencil $B - \lambda C$, where B and C are Hermitian and
 370 real-symmetric matrices, respectively, of size $K = L^d$. The λ_n and eig_n , $n = 1, \dots, K$, are known as generalized eigenvalues and eigenvectors,
 371 respectively. The matrix $C = \nabla^T \nabla$ is clearly positive semidefinite. In this section, we will assume that C is positive definite, hence invertible.
 372 We will discuss the case where C is positive semidefinite in Appendix G, which is necessary for the setting where ∇ incorporates *periodic*
 373 boundary conditions—needed for our study of advection enhanced diffusion by a spatially periodic fluid velocity field \mathbf{u} .

374 Since B and C are Hermitian and real-symmetric, respectively, and C is positive definite, the generalized eigenvalue problem in (31) has
 375 properties which are similar to the properties of the standard symmetric eigenvalue problem.⁴⁷ In particular, the generalized eigenvalues λ_n are
 376 all real, the generalized eigenvectors eig_n form a basis for \mathbb{C}^K , and they are orthonormal in the following sense: $\langle \text{eig}_n, \text{eig}_m \rangle = \delta_{nm}$, $n, m = 1, \dots, K$.⁴⁷

377 Since $C = \nabla^T \nabla$ is real-valued, this is equivalent to the Sobolev-type orthogonality condition,

378

$$\nabla z_n \cdot \nabla z_m = \delta_{nm}.$$



(32)

379 In other words, the generalized eigenvectors z_n are orthonormal with respect to the “discrete inner-product” $\langle \cdot, \cdot \rangle_{1,2}$ defined by $\langle \xi, \zeta \rangle_{1,2}$
 380 $= \langle \nabla \xi \cdot \nabla \zeta \rangle$, for $\xi, \zeta \in \mathbb{C}^K$ and $\langle \cdot \rangle$ denotes ensemble averaging. Denoting by Z the matrix with columns consisting of the generalized eigenvec-
 381 tors z_n , q. (32) is seen to be equivalent to $[\nabla Z]^\dagger [\nabla Z] = I$, or $Z^\dagger C Z = I$. A key feature of the generalized eigenvalue problem is that the matrix
 382 Z simultaneously diagonalizes B and C . Specifically, if Λ is the diagonal matrix whose elements on the main diagonal are the generalized
 383 eigenvalues λ_n , then⁴⁷

$$384 \quad Z^\dagger B Z = \Lambda, \quad Z^\dagger C Z = I. \quad (33)$$

385 We now derive the discrete version of Eqs. (16)–(18) comprising the key results of the spectral theorem, for the generalized eigen-
 386 value problem setting. These derivations will streamline and clarify our results for the current section, showing how the derived series
 387 representations of the symmetric \mathfrak{S}^* and antisymmetric \mathfrak{A}^* parts of the effective diffusivity matrix \mathfrak{D}^* can be written as the Stieltjes inte-
 388 grals in Eq. (19), involving a discrete spectral measure. This derivation will also clarify and streamline our results in the appendix, which
 389 lead to the numerical algorithm used in Sec. V for spectral computations of \mathfrak{D}^* for periodic fluid flows. The numerical algorithm used in
 390 Sec. V is analogous to the algorithm that we develop in this section, which is elegant for the full-rank setting—revealing a great deal of
 391 structure with minimal effort. The matrix analysis of the rank-deficient setting developed in Appendix G is quite a bit more involved. Devel-
 392 oping the full-rank setting in this section first makes the results of the rank-deficient setting more transparent and the final results more
 393 anticipated.

394 Since the z_n , $n = 1, \dots, K$, form a basis for \mathbb{C}^K and satisfy the orthogonality relation in (32), for all $\xi \in \mathbb{C}^K$, we have $\xi = \sum_n (\nabla z_n \cdot \nabla \xi) z_n$,
 395 which implies

$$396 \quad \sum_{n=1}^K Q_n = I, \quad Q_n = z_n [\nabla z_n]^\dagger \nabla, \quad Q_l Q_m = Q_l \delta_{lm}, \quad (34)$$

397 where the matrix operators Q_n , $n = 1, \dots, K$, are self-adjoint with respect to the discrete inner-product $\langle \cdot, \cdot \rangle_{1,2}$ defined above, i.e., $\langle Q_n \xi, \zeta \rangle_{1,2}$
 398 $= \langle \xi, Q_n \zeta \rangle_{1,2}$ for all $\xi, \zeta \in \mathbb{C}^K$. From $B z_n = \lambda_n C z_n$ and Eq. (34), we have that $B Q_n = \lambda_n C Q_n$ which is equivalent to $C^{-1} B Q_n = \lambda_n Q_n$, since
 399 the matrix C is invertible. This formula and (34) then imply that the matrix $C^{-1} B$ has the spectral decomposition $C^{-1} B = \sum_n \lambda_n Q_n$. By the
 400 mutual orthogonality of the projection matrices Q_n and by induction, we have that $[C^{-1} B]^m = \sum_n \lambda_n^m Q_n$ for all $m \in \mathbb{N}$. This, in turn, implies
 401 that $f(C^{-1} B) = \sum_n f(\lambda_n) Q_n$ for any polynomial $f : \mathbb{R} \mapsto \mathbb{C}$.

402 From the mutual orthogonality of the projection matrices Q_n and their symmetry with respect to the discrete inner-product $\langle \cdot, \cdot \rangle_{1,2}$, it follows that, for all $\xi, \zeta \in \mathbb{C}^K$ and all complex-valued polynomials $f(\lambda)$ and $h(\lambda)$, the bilinear functional $\langle f(C^{-1} B) \xi, h(C^{-1} B) \zeta \rangle_{1,2}$ has the
 403 integral representation in (17), with M substituted by $C^{-1} B$ and other appropriate notational changes. Moreover, the complex-valued function
 404 $\mu_{\xi\zeta}(\lambda) = \langle Q(\lambda) \xi, \zeta \rangle_{1,2}$ in (17) is now given by $\mu_{\xi\zeta}(\lambda) = \langle Q(\lambda) \xi, \zeta \rangle_{1,2}$, where the associated matrix representation $Q(\lambda)$ of the projection operator
 405 $Q(\lambda)$ and the discrete spectral measure $d\mu_{\xi\zeta}(\lambda)$ are given by

$$407 \quad Q(\lambda) = \sum_{n: \lambda_n \leq \lambda} \theta(\lambda - \lambda_n) Q_n, \quad d\mu_{\xi\zeta}(\lambda) = \sum_{n: \lambda_n \leq \lambda} \langle \delta_{\lambda_n}(d\lambda) [\nabla Q_n \xi \cdot \nabla \zeta] \rangle. \quad (35)$$

408 Here, $\theta(\lambda)$ is the Heaviside function, satisfying $\theta(\lambda) = 0$ for $\lambda < 0$ and $\theta(\lambda) = 1$ for $\lambda \geq 0$, and $\delta_{\lambda_n}(d\lambda) = d\theta(\lambda - \lambda_n)$ is the δ -measure centered at
 409 λ_n . From Eq. (34) and the well-known properties of $\theta(\lambda)$, we have that $Q(\lambda)$ satisfying Eq. (16). From Eq. (34) and the well-known properties
 410 of the δ -measure, the mass $\mu_{\xi\zeta}^0$ of the spectral measure in (35) satisfies Eq. (18) with appropriate notational changes. We are now ready to
 411 present the main result of this section.

412 **Theorem 3.** Consider the generalized eigenvalue problem $B z_n = \lambda_n z_n$ in (31). Let Z be the matrix with columns consisting of the eigen-
 413 vectors z_n and Λ be the diagonal matrix with eigenvalues λ_n on the diagonal which satisfy Eq. (33). The discrete, matrix representations of the
 414 bilinear functional formulas for \mathfrak{S}_{jk}^* and \mathfrak{A}_{jk}^* in Eq. (11) are given by

$$415 \quad \mathfrak{S}_{jk}^* = \varepsilon(\delta_{jk} + \langle \nabla \chi_j \cdot \nabla \chi_k \rangle), \quad \mathfrak{A}_{jk}^* = \langle \nabla C^{-1} [iB] \chi_j \cdot \nabla \chi_k \rangle. \quad (36)$$

416 Also, the discrete representation of the resolvent formula for Eq. (12) is given by

$$417 \quad \chi_j = Z(\varepsilon I + i\Lambda)^{-1} Z^\dagger u_j. \quad (37)$$

418 The discrete representations of the bilinear functional formulas for \mathfrak{S}_{jk}^* and \mathfrak{A}_{jk}^* in (13) are given by

$$419 \quad \mathfrak{S}_{jk}^* = \varepsilon(\delta_{jk} + \langle (\varepsilon I + i\Lambda)^{-1} Z^\dagger u_j \cdot (\varepsilon I + i\Lambda)^{-1} Z^\dagger u_k \rangle), \quad (38)$$

$$420 \quad \mathfrak{A}_{jk}^* = \langle i\Lambda(\varepsilon I + i\Lambda)^{-1} Z^\dagger u_j \cdot (\varepsilon I + i\Lambda)^{-1} Z^\dagger u_k \rangle.$$

421 Consequently, from the discrete analog of Eq. (23) and the formulas for \mathfrak{S}_{jk}^* and \mathfrak{A}_{jk}^* in (38), we have the following series representations:

$$422 \quad \mathfrak{S}_{jk}^*/\varepsilon - \delta_{jk} = \sum_{n=1}^K \frac{\operatorname{Re} [\overline{(z_n^\dagger u_j)} u_k]}{\varepsilon^2 + \lambda_n^2}, \quad \mathfrak{A}_{jk}^* = \sum_{n=1}^K \frac{\lambda_n \operatorname{Im} [\overline{(z_n^\dagger u_j)} z_n^\dagger u_k]}{\varepsilon^2 + \lambda_n^2}. \quad (39)$$

423 Finally, defining $\mathfrak{g}_j = (\nabla^T \nabla)^{-1} u_j$ and recalling the projection matrix Q_n in (34), we have

$$424 \quad (\overline{z_n^\dagger u_j})(z_n^\dagger u_k) = \nabla Q_n \mathfrak{g}_j \cdot \nabla \mathfrak{g}_k. \quad (40)$$

425 It follows from Eqs. (39) and (40) that the series representations for \mathfrak{S}_{jk}^* and \mathfrak{A}_{jk}^* in (39) have the Stieltjes integral representations in Eq. (19),
426 involving the discrete spectral measure μ_{jk} in (35) with $\xi = \mathfrak{g}_j$ and $\zeta = \mathfrak{g}_k$.

427 Proof of Theorem 3. From the matrix representation $A = (\nabla \cdot \nabla^T H \nabla)^{-1} (\nabla^T H \nabla)$ of the operator $A = \Delta^{-1} \nabla \cdot [H \nabla]$ and Eq. (31), the matrix
428 representation of the functional formulas $\mathfrak{S}_{jk}^* = \varepsilon(\delta_{jk} + \langle \chi_j, \chi_k \rangle_{1,2})$ and $\mathfrak{A}_{jk}^* = \langle A \chi_j, \chi_k \rangle_{1,2}$ in Eq. (11) are given by (36). Moreover, the matrix
429 representation of the cell problem $\varepsilon \Delta \chi_j + \nabla \cdot [H \nabla] \chi_j = -u_j$ in (4) is given by

$$430 \quad (\varepsilon C + iB)\chi_j = u_j. \quad (41)$$

431 The matrix Z is invertible, as the generalized eigenvectors z_n form a basis for \mathbb{C}^K . Consequently, by Eq. (33), we have that $B = Z^{-\dagger} \Lambda Z^{-1}$,
432 $C = Z^{-\dagger} Z^{-1}$. It now follows from Eq. (41) that $Z^{-\dagger}(\varepsilon I + i\Lambda)Z^{-1} u_j$, which implies the resolvent formula for χ_j in Eq. (37).

433 Substituting the resolvent formula for χ_j in (37) into Eq. (36) yields Eq. (38), where we have used that $[\nabla Z]^\dagger = [\nabla Z]^{-1}$. The quadratic
434 form $Z^\dagger u_j \cdot Z^\dagger u_k$ arising in (38) can be written in terms of the projection matrices Q_n defined in (34) as follows:

$$435 \quad Z^\dagger u_j \cdot Z^\dagger u_k = \sum_{n=1}^K (\overline{z_n^\dagger u_j})(z_n^\dagger u_k) = \sum_{n=1}^K z_n z_n^\dagger u_j \cdot u_k. \quad (42)$$

436 We now demonstrate that $z_n z_n^\dagger u_j \cdot u_k = \nabla Q_n \mathfrak{g}_j \cdot \nabla \mathfrak{g}_k$, where $\mathfrak{g}_j = (\nabla^T \nabla)^{-1} u_j$

$$437 \quad z_n z_n^\dagger u_j \cdot u_k = z_n z_n^\dagger [\nabla^T \nabla] \mathfrak{g}_j \cdot [\nabla^T \nabla] \mathfrak{g}_k = [\nabla z_n] [\nabla z_n]^\dagger \nabla \mathfrak{g}_j \cdot \nabla \mathfrak{g}_k = \nabla Q_n \mathfrak{g}_j \cdot \nabla \mathfrak{g}_k, \quad (43)$$

438 which establishes Eq. (40). This concludes our Proof of Theorem 3. \square

439 In Sec. V, we use a generalization of Eq. (39) to compute Stieltjes integral representations for the symmetric \mathfrak{S}^* and antisymmetric \mathfrak{A}^*
440 parts of the effective diffusivity matrix \mathfrak{D}^* for some model periodic fluid velocity fields. This generalization, discussed in Theorem 10, is a
441 direct analog of Eq. (39) and holds for the setting where the matrix gradient ∇ with periodic boundary conditions is rank-deficient, so the
442 negative matrix Laplacian $\nabla^T \nabla$ is noninvertible.

443 We conclude this section with a discussion that helps reduce the amount of memory required to store the eigenvalues and spectral
444 weights comprising the discrete spectral measure, which is useful when computing a large number of statistical realizations associated with
445 randomly perturbed periodic flows. From the formula for $\mu_{\xi\xi}(\lambda)$ above Eq. (35), the fact that the matrix ∇ and vectors \mathfrak{g}_k are real-valued and
446 the two identities $\operatorname{Re} \mu_{jk}(\lambda) = (\mu_{jk}(\lambda) + \bar{\mu}_{jk}(\lambda))/2$ and $\operatorname{Im} \mu_{jk}(\lambda) = (\mu_{jk}(\lambda) - \bar{\mu}_{jk}(\lambda))/(2i)$, we have

$$447 \quad \operatorname{Re} \mu_{jk}(\lambda) = \frac{1}{2} \sum_{n: \lambda_n \leq \lambda} \langle \theta(\lambda - \lambda_n) [\nabla(Q_n + \bar{Q}_n) \mathfrak{g}_j \cdot \nabla \mathfrak{g}_k] \rangle, \quad (44)$$

$$448 \quad \operatorname{Im} \mu_{jk}(\lambda) = \frac{1}{2i} \sum_{n: \lambda_n \leq \lambda} \langle \theta(\lambda - \lambda_n) [\nabla(Q_n - \bar{Q}_n) \mathfrak{g}_j \cdot \nabla \mathfrak{g}_k] \rangle,$$

449 with $[\nabla(Q_n + \bar{Q}_n) \mathfrak{g}_j \cdot \nabla \mathfrak{g}_k] = 2 \operatorname{Re} [\nabla Q_n \mathfrak{g}_j \cdot \nabla \mathfrak{g}_k]$ and $[\nabla(Q_n - \bar{Q}_n) \mathfrak{g}_j \cdot \nabla \mathfrak{g}_k] = 2i \operatorname{Im} [\nabla Q_n \mathfrak{g}_j \cdot \nabla \mathfrak{g}_k]$.

450 Consider the generalized eigenvalue problem in Eq. (31) written as $[iB]z_n = \omega z_n$, with $B = -i\nabla^T H \nabla$ and $C = \nabla^T \nabla$. Since the
451 matrices iB and C are real-valued, we have $[iB]\bar{z}_n = -i\lambda_n C \bar{z}_n$. Consequently, the (generalized) eigenvectors z_n in complex conjugate pairs and the λ_n come in \pm pairs. Therefore, if the size K of these matrices is even, then we may renumber the index set \mathcal{I}_K as
452 $\mathcal{I}_K = \{-K/2, \dots, -1, 1, \dots, K/2\}$ such that $\lambda_{-n} = -\lambda_n$ and $z_{-n} = \bar{z}_n$. If K is odd, then $\lambda_0 = 0$ is also an eigenvalue with a real-valued eigenvector z_0 . Consequently, the representations of the measures $\operatorname{Re} \mu_{jk}$ and $\operatorname{Im} \mu_{jk}$, following from the functions in Eq. (44), can be simplified⁴⁸
453 to depend only on the restricted index set $\{n \geq 0 : \lambda_n \leq \lambda\}$. This is clear from Eqs. (19) and (44), since for $n \geq 0$ we have $\lambda_{-n}^2 = (-\lambda_n)^2 = \lambda_n^2$ and
454 $z_{-n} = \bar{z}_n$ thus $Q_{-n} = \bar{Q}_n$. Consequently,

$$455 \quad \operatorname{Re} [\nabla Q_n \mathfrak{g}_j \cdot \nabla \mathfrak{g}_k] + \operatorname{Re} [\nabla Q_{-n} \mathfrak{g}_j \cdot \nabla \mathfrak{g}_k] = 2 \operatorname{Re} [\nabla Q_n \mathfrak{g}_j \cdot \nabla \mathfrak{g}_k]. \quad (45)$$

458

$$\lambda_n \operatorname{Im} [\nabla Q_n g_j \cdot \nabla g_k] + \lambda_{-n} \operatorname{Im} [\nabla Q_{-n} g_j \cdot \nabla g_k] = 2\lambda_n \operatorname{Im} [\nabla Q_n g_j \cdot \nabla g_k],$$



459 with $\lambda_0 \operatorname{Im} [Q_0 g_j \cdot g_k] \equiv 0$. For numerical computations of statistical properties of advection enhanced diffusion by randomly perturbed peri-
 460 odic flows, a useful consequence of this is only *half* of the eigenvalues and spectral weights need to be held in memory, as the other half are
 461 redundant, which saves memory consumption.

462 V. SPECTRAL COMPUTATIONS OF THE EFFECTIVE DIFFUSIVITY MATRIX

463 In Sec. IV, we developed a mathematical framework that provides discrete Stieltjes integral representations for the symmetric \mathfrak{S}^* and
 464 antisymmetric \mathfrak{A}^* parts of the effective diffusivity matrix \mathfrak{D}^* . These discrete integral representations can be written as the series shown in
 465 Eq. (39) or the integrals shown in (19), involving the discrete spectral measure in (35) with the appropriate notational changes described in
 466 Theorem 3. This framework assumes that the matrix gradient ∇ has Dirichlet boundary conditions, for example, so the matrix is *full-rank* and
 467 the negative matrix Laplacian $\nabla^T \nabla$ is invertible. However, for our studies of advection enhanced diffusion by spatially periodic fluid velocity
 468 fields, we need to use a matrix gradient ∇ with periodic boundary conditions and this matrix is *rank-deficient*. In order to streamline our
 469 presentation leading to the numerical results of this section, in Appendix G, we extend the discrete mathematical framework developed in
 470 Sec. IV to the rank-deficient setting. This analysis, in the Proof of Theorem 10, shows that the discrete Stieltjes integral representations for \mathfrak{S}^*
 471 and \mathfrak{A}^* are given by direct analogs of the formulas in Eq. (39).

472 In this section, we use these direct analogs of the formulas in Eq. (39) to compute \mathfrak{D}^* for various model periodic flows and randomly
 473 perturbed periodic flows. As a benchmark test, we compute the spectral measure and \mathfrak{D}^* for a shear flow, which are known in closed form,⁴
 474 and a cell flow with closed streamlines, for which it is known^{17,18} that $\mathfrak{D}^* \sim \varepsilon^{1/2}$ for $\varepsilon \ll 1$. Our numerical results are in good agreement
 475 with the theoretical results. We also consider a fluid velocity field that has a free parameter. As the parameter varies, the flow transitions
 476 from cell flow with closed streamlines to shear flow in the diagonal $x - y$ direction. This gives rise to transitional behavior in the spectral
 477 measure, which governs transitional behavior in the effective diffusivity matrix \mathfrak{D}^* . For the sake of brevity, we will focus our attention on
 478 the ε -behavior of the components \mathfrak{S}_{jk}^* , $j, k = 1, \dots, d$, of \mathfrak{S}^* . Also, for computational simplicity, we have restricted our computations to
 479 dimension $d = 2$.

480 A. Numerical methods

481 By Eq. (28), the time-independent fluid velocity field $\mathbf{u} = \mathbf{u}(\mathbf{x})$ is given in terms of an antisymmetric matrix $\mathsf{H} = \mathsf{H}(\mathbf{x})$, $\mathbf{u} = \nabla \cdot \mathsf{H}$. For
 482 dimension $d = 2$, the matrix H is determined by a stream function $\Psi = \Psi(\mathbf{x})$,

$$483 \quad \mathsf{H} = \begin{bmatrix} 0 & \Psi \\ -\Psi & 0 \end{bmatrix}, \quad (46)$$

484 yielding $\mathbf{u} = [-\partial_y \Psi, \partial_x \Psi]$, where ∂_x denotes partial differentiation in the variable x , for example. In this section, we consider two flows with
 485 free parameters which transition from cell flow to shear flow as parameters vary. In particular, we consider BC-flow¹¹ and “cat’s eye” flow,¹⁷
 486 which are defined by the following stream functions Ψ_{BC} and Ψ_{CE} , respectively:

$$487 \quad \Psi_{BC}(\mathbf{x}) = B \sin x - C \sin y, \quad \Psi_{CE}(\mathbf{x}) = \sin x \sin y + \alpha \cos x \cos y, \quad (47)$$

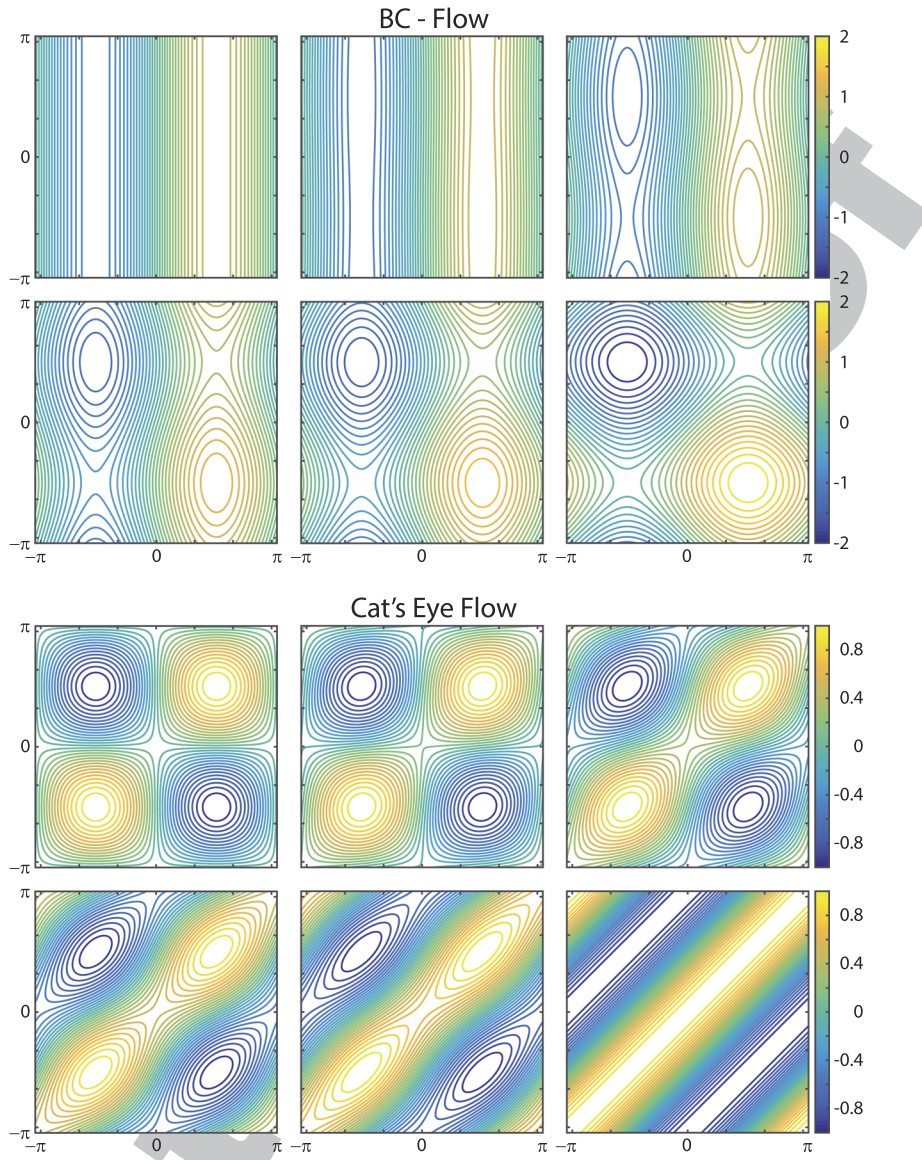
488 where we have denoted $\mathbf{x} = (x, y)$. The corresponding fluid velocity fields are

$$489 \quad \mathbf{u}_{BC}(\mathbf{x}) = (C \cos y, B \cos x), \quad (48)$$

$$\mathbf{u}_{CE}(\mathbf{x}) = (-\sin x \cos y + \alpha \cos x \sin y, \cos x \sin y - \alpha \sin x \cos y).$$

490 The flow geometry of these fluid velocity fields transition from the shear flow to cell flow structure as the system parameters
 491 $\alpha, B, C \in [0, 1]$ vary.

492 The streamlines of a 2D flow are level sets of the stream function Ψ , which define a family of curves that are instantaneously tangent to
 493 the fluid velocity field \mathbf{u} , since $\mathbf{u} = [-\partial_y \Psi, \partial_x \Psi]$ implies that $\mathbf{u} \cdot \nabla \Psi = 0$. In Fig. 1, we display streamlines of the flows in Eq. (47) for vari-
 494 ous parameter values. The streamlines for cat’s eye flow are symmetric about the line $y = x$, which follows from the symmetry of the stream
 495 function $\Psi_{CE}(x, y) = \Psi_{CE}(y, x)$. The stream function for BC-flow has a more complicated symmetry $\Psi(x, y; B, C) = -\Psi(y, x; C, B)$. This sym-
 496 metry indicates that if the values of B and C are interchanged, $B \leftrightarrow C$, then the original flow is recovered from a 90° rotation ($x \rightarrow y, y \rightarrow -x$)
 497 followed by a reflection about the x -axis ($y \rightarrow -y$). Consequently, flows elongated in the y -direction become flows elongated in the x -direction
 498 under the interchange $B \leftrightarrow C$. Consistently, our numerical computations of μ_{jk} and \mathfrak{S}_{jk}^* , $j, k = 1, 2$, exhibit these symmetries. For BC-flow,
 499 these symmetries allow us to restrict our attention to the behavior of μ_{jk} and \mathfrak{S}_{jk}^* as only one parameter varies. Here, we discuss our results for
 500 cat’s eye flow for various (deterministic) values of the parameter α as well as α uniformly distributed on the interval $[0, p]$ for various values of
 501 p . For the sake of brevity, we consider BC-shear flow in the x and y directions only, which are obtained for parameter values $(B, C) = (0, 1)$ and
 502 $(B, C) = (1, 0)$, respectively, and do not display our results for the transitional behavior from one extreme to the other. The spectral measure
 503 and \mathfrak{D}^* were computed for BC-cell flow in Ref. 44.



504
505 FIG. 1. Transitions in the flow structure. The streamlines for BC-flow and cat's eye flow are displayed for various parameter values, transitioning from the shear to cell flow
506 structure. From left to right and top to bottom, the parameter values associated with the BC-flow are $B = 1$ fixed and $C = 0, 0.01, 0.1, 0.3, 0.5$, and 1 , while those for cat's eye
flow are $\alpha = 0, 0.1, 0.3, 0.5, 0.7$, and 1 .

507 In Sec. III, we gave an overview of the effective parameter problem for the setting of randomly perturbed \mathcal{V} -periodic flows and introduced
508 the Hilbert space \mathcal{H} in Eq. (7). Numerically, it is natural to set \mathcal{H} to be the space of randomly perturbed \mathcal{V} -periodic functions, $\mathcal{H} = L^2(m \times \mathbb{S})$,
509 where P is the probability measure associated with the random variable α .²⁹ In this case, by Fubini's theorem,²⁰ $\langle \cdot \rangle$ can be considered to denote
510 spatial averaging followed by statistical averaging.

511 We now discuss in more detail our discrete, matrix formulation of the effective parameter problem. To illustrate how to generalize
512 these ideas to dimension d larger than $d = 2$, we will maintain the aspects of our general notation. In this discrete setting, the spatial
513 region $\mathcal{V} = [0, 2\pi]^d$, for example, is replaced by a square lattice \mathcal{V}_L^d of size L containing L^d equally spaced points in \mathcal{V} . As discussed in
514 Sec. IV, the differential operators ∇ and $\nabla \cdot$ are replaced by finite difference, matrix operators ∇ and $-\nabla^T$, respectively, with suitable
515 boundary conditions. Periodic boundary conditions will be assumed throughout this section. Since these matrices operate on vectors,
516 the d -dimensional lattice \mathcal{V}_L^d must be bijectively mapped to a one dimensional lattice \mathcal{V}_N of size $N = L^d d$. The specific structure of \mathcal{V}_N

and ∇ depend on the bijective mapping Θ chosen. In our computations discussed in this section, we used the mapping Θ described in Ref. 42.

The spatially dependent d -dimensional vector field $\mathbf{v}(\mathbf{x}) = (v_1(\mathbf{x}), \dots, v_d(\mathbf{x}))$, say, is bijectively mapped by Θ to a discretized *constant* vector $(\mathbf{v}_1, \dots, \mathbf{v}_2)$ with N elements, where the vectors $\mathbf{v}_i, i = 1, \dots, d$, each have L^d elements and contain all of the spatial information about the $v_i(\mathbf{x})$ for $\mathbf{x} \in \mathcal{V}_L^d$. Similarly, the d -dimensional standard basis vector $\mathbf{e}_1 = (1, 0, \dots, 0)$ is mapped to the N -dimensional vector $(\mathbf{1}, \mathbf{0}, \dots, \mathbf{0})$, where $\mathbf{1}$ and $\mathbf{0}$ are vectors of ones and zeros with L^d elements, and similarly for the \mathbf{e}_j for $j = 2, \dots, d$. Therefore, the vectors $\widehat{\mathbf{e}}_j, j = 1, \dots, d$, satisfying

$$\widehat{\mathbf{e}}_j = \Theta(\mathbf{e}_j)/L^{d/2}, \quad \widehat{\mathbf{e}}_j \cdot \widehat{\mathbf{e}}_k = \delta_{jk}, \quad (49)$$

serve as “lattice standard basis vectors.” With this convention, the division by $L^{d/2}$ in (49) takes care of the uniform L -scaling in discrete approximations of spatial integrals; instead of the $(2\pi)^d$ normalized Lebesgue measure $d\mathbf{x}$, we have $\Delta\mathbf{x} = (2\pi/L)^d/(2\pi)^d$ when $\mathcal{V} = [0, 2\pi]^d$ and the spatial average $\langle \xi(\mathbf{x}) \zeta(\mathbf{x}) \rangle_{\mathcal{V}}$ becomes $\xi \cdot \zeta/L^d$. In a similar way, the 2×2 matrix $\mathsf{H}(\mathbf{x})$ in (46) becomes a $N \times N$ antisymmetric banded matrix, where the stream function $\Psi(\mathbf{x})$ is represented by a diagonal $L^d \times L^d$ matrix and the zero element 0 is represented by a matrix of zeros. As in previous sections, for notational simplicity, we will not make a notational distinction for the matrix H between the continuum and discrete settings as the context will be clear.

In Theorem 10 of Appendix G, we extend our results developed in Theorem 1 of Sec. III to the setting where the matrix gradient ∇ has periodic boundary conditions and is rank-deficient. This is accomplished by considering the singular value decomposition (SVD) $\nabla = \mathbf{U}\Sigma\mathbf{V}^T$. Here, ∇ is of size $N \times K$, say, where $K = L^d$ and $N = Kd$. Also, $\Sigma = \text{diag}(\sigma_1, \dots, \sigma_K)$, where $0 \leq \sigma_1 \leq \dots \leq \sigma_K$. The matrices \mathbf{U} and \mathbf{V} are of size $N \times K$ and $K \times K$, respectively, and satisfy $\mathbf{U}^T \mathbf{U} = \mathbf{I}$ and $\mathbf{V}^T \mathbf{V} = \mathbf{V} \mathbf{V}^T = \mathbf{I}$, where \mathbf{I} is the identity matrix of size K .¹⁴ When ∇ is of full rank, then the singular values satisfy $\sigma_j > 0$ for all $j = 1, \dots, K$ and the matrix Laplacian $\nabla^T \nabla = \nabla \Sigma^2 \nabla^T$ is invertible. When ∇ is rank-deficient, then there are K_1 nonzero singular values and $K_0 = K - K_1$ zero singular values, say. For example, when $d = 2$, the nullity of ∇ is 1 so $K_1 = K - 1$. In this case, we write $\mathbf{U} = [\mathbf{U}_0 \ \mathbf{U}_1]$, $\Sigma = \text{diag}(\mathbf{O}, \Sigma_1)$, and $\mathbf{V} = [\mathbf{V}_0 \ \mathbf{V}_1]$, where \mathbf{O} is a matrix of zeros so that $\nabla = \mathbf{U}_1 \Sigma_1 \mathbf{V}_1^T$. The negative matrix Laplacian $\nabla^T \nabla = \mathbf{V}_1 \Sigma_1^2 \mathbf{V}_1^T$ is noninvertible, since $\mathbf{V}_1 \mathbf{V}_1^T \neq \mathbf{I}$.

The associated matrix analysis in Appendix G demonstrates that the spectral measure μ_{jk} underlying the Stieltjes integral representation of \mathfrak{G}_{jk}^* is given by

$$d\mu_{jk}(\lambda) = \sum_{n: \lambda_n^1 \leq \lambda} \langle m_{jk}(n) \delta_{\lambda_n^1}(d\lambda) \rangle, \quad (50)$$

where $\lambda_n^1, n = 1, \dots, K_1$, are the eigenvalues of the matrix $-\imath \mathbf{U}_1^T \mathsf{H} \mathbf{U}_1$, while various equivalent representations of the spectral weights $m_{jk}(n)$, $j, k = 1, \dots, d$, are given in Eq. (G7) of Theorem 10. For notational simplicity, in this section, we denote $\text{Re } \mu_{jk}$ by μ_{jk} . In our computations of μ_{jk} , we used

$$m_{jk}(n) = \text{Re} \left[\overline{([\mathbf{r}_n^1]^\dagger \mathbf{U}_1^T \mathsf{H} \mathbf{e}_j)} ([\mathbf{r}_n^1]^\dagger \mathbf{U}_1^T \mathsf{H} \mathbf{e}_k) \right], \quad n = 1, \dots, K_1, \quad (51)$$

which follows from Eqs. (43), (44), (G6), and (G7). Here, $\mathbf{r}_n^1, n = 1, \dots, K_1$, are the *complex* eigenvectors of the matrix $-\imath \mathbf{U}_1^T \mathsf{H} \mathbf{U}_1$. Consequently, $m_{kk}(n) \geq 0$, so μ_{kk} is a positive measure and $\mu_{jk}, j \neq k$, is a signed measure, where $m_{jk}(n)$ in (51) can take positive or negative values.

To reveal the structure of μ_{12} and \mathfrak{G}_{12}^* in our numerical computations discussed in Sec. V B, we denote the spectral weights $m_{jk}(n)$ associated with the Jordan decomposition $\mu_{jk} = \mu_{jk}^+ - \mu_{jk}^-$ in (27) by $m_{jk}^+(n)$ and $m_{jk}^-(n)$, where $m_{jk}^\pm(n) \geq 0$. Also, we define the functions $[\mathfrak{G}_{12}^*]^+$ and $[\mathfrak{G}_{12}^*]^-$,

$$[\mathfrak{G}_{12}^*]^+(\varepsilon) = \max\{\mathfrak{G}_{12}^*(\varepsilon), 0\}, \quad [\mathfrak{G}_{12}^*]^{-}(\varepsilon) = \max\{-\mathfrak{G}_{12}^*(\varepsilon), 0\}, \quad (52)$$

for each $0 < \varepsilon < \infty$, so that $\mathfrak{G}_{12}^* = [\mathfrak{G}_{12}^*]^+ - [\mathfrak{G}_{12}^*]^-$, $[\mathfrak{G}_{12}^*]^\pm(\varepsilon) = \mathfrak{G}_{12}^*(\varepsilon; \mu_{12}^\pm)$, and $[\mathfrak{G}_{12}^*]^\pm \geq 0$.

In the case of a nonrandom fluid velocity field \mathbf{u} , we used $L = 200$ so that $K_1 = 39\,999$. The eigenvalues λ_n^1 and eigenvectors \mathbf{r}_n^1 of the nonrandom Hermitian matrix $-\imath \mathbf{U}_1^T \mathsf{H} \mathbf{U}_1$ were computed using the Matlab function `eig()`. In this case, the averaging $\langle \cdot \rangle$ in (50) is interpreted as spatial averaging over the period cell \mathcal{V} . In the setting of a randomly perturbed flow, we used $L = 100$ so that $K_1 = 9999$. In this case, the averaging $\langle \cdot \rangle$ in (50) is interpreted as spatial averaging followed by ensemble averaging over $\sim 10^3$ statistical trials.

The numerical accuracy of the eigenvalue problem is determined by the *eigenvalue condition numbers* $\mathcal{K}(\lambda_n^1), n = 1, \dots, K_1$, which are the reciprocals of the cosines of the angles between the left and right eigenvectors. Large eigenvalue condition numbers of a Hermitian matrix implies that it is near a matrix with multiple eigenvalues, while eigenvalue condition numbers close to 1 imply that the eigenvalue problem is well-conditioned. The eigenvalue problem for the matrix $-\imath \mathbf{U}_1^T \mathsf{H} \mathbf{U}_1$ is extremely well conditioned with $\max_n |1 - \mathcal{K}(\lambda_n^1)| \sim 10^{-14}$ typical, computed using Matlab’s function `condeig()`.

To the best of our knowledge, Matlab does not provide a function that describes the accuracy of the computed SVD of the matrix $\nabla = \mathbf{U}\Sigma\mathbf{V}^T$. In order to better understand the numerical accuracy in the entries of the matrix \mathbf{U} , which is central to our computational method, we performed the following tests. For the case of Dirichlet boundary conditions, the matrix ∇ is full-rank; hence, the matrix Laplacian $\nabla^T \nabla$ is invertible. We computed the matrix $\Gamma = \nabla(\nabla^T \nabla)^{-1} \nabla^T$ diluting using Matlab’s `mldivide` function, i.e., $\Gamma = \nabla((\nabla^T \nabla) \backslash \nabla^T)$, and also using the

566 SVD of the matrix ∇ , with $\Gamma = \mathbf{U}\mathbf{U}^T$. We then computed the componentwise maximum difference $\max_{lm} |[\nabla((\nabla^T \nabla) \setminus \nabla^T)]_{lm}|$. When
 567 $L = 100$ and $L = 200$, this difference is $\sim 10^{-15}$, which gives an idea of the accuracy of the SVD of ∇ for the rank-deficient, periodic setting. The
 568 matrix Γ is used extensively throughout Appendix E. In all of our computations, Matlab's sparse architecture was employed wherever possible
 569 to reduce roundoff errors.

570 B. Numerical results

571 Before we discuss our numerical results in this section, it is helpful to first describe the relationship between the spectral measure μ_{jk} and
 572 the ε -behavior of \mathfrak{S}_{jk}^* . This relationship is easiest to understand when $j = k$, in terms of the enhancement in scalar transport above the bare
 573 diffusive value ε , as shown in Eq. (20). Consider μ_{kk} and \mathfrak{S}_{kk}^* , for some $k = 1, \dots, d$, and write the formula in (20) as

$$574 \quad \mathfrak{S}_{kk}^*(\varepsilon) = \varepsilon + \mathcal{E}_{kk}(\varepsilon), \quad \mathcal{E}_{kk}(\varepsilon) = \varepsilon \int_{-\infty}^{\infty} \frac{d\mu_{kk}(\lambda)}{\varepsilon^2 + \lambda^2}, \quad (53)$$

575 where $\mathcal{E}_{kk}(\varepsilon) \geq 0$ denotes the *enhancement* above ε . By Eq. (15), the spectrum Σ of the self-adjoint operator M is a bounded subset of \mathbb{R} .
 576 Consequently, in the *diffusion dominated regime* where $\varepsilon \gg |\lambda|$ for all $\lambda \in \Sigma$, we have²⁰ $\mathfrak{S}_{kk}^* \sim \varepsilon + \mu_{kk}^0/\varepsilon$. The enhancement $\mathcal{E}_{kk}(\varepsilon) \sim \mu_{kk}^0/\varepsilon$ is
 577 only nominal in this regime where $\varepsilon \gg 1$ and is independent of the distribution of measure mass—dependent only the total mass. However,
 578 in the *advection dominated regime* where $\varepsilon \ll 1$, if the spectral measure μ_{kk} has significant mass near the spectral origin $\lambda = 0$, e.g., if the
 579 spectral weights $m_{kk}(n)$ in (50) have values significantly greater than zero for $|\lambda_n| \ll 1$, then the integrand associated with $\mathcal{E}_{kk}(\varepsilon)$ can intro-
 580 duce singular behavior that competes with the small ε prefactor in front of the integral, giving rise to a significant enhancement $\mathcal{E}_{kk}(\varepsilon)$ for
 581 $0 < \varepsilon \ll 1$. Although, if the mass of the measure is zero or extremely small in a neighborhood of $\lambda = 0$, then the enhancement $\mathcal{E}_{kk}(\varepsilon)$ can be less
 582 pronounced, since the small ε prefactor dominates the (lack of) singular behavior in the integrand near $\varepsilon = 0$. This illustrates that in the advect-
 583 tion dominated regime, where $0 < \varepsilon \ll 1$, the ε -behavior of the enhancement $\mathcal{E}_{kk}(\varepsilon)$ depends strongly on the details of the spectral measure μ_{kk}
 584 near $\lambda = 0$.

585 We emphasize that, due to roundoff errors and finite resolution ($L < \infty$) effects, our numerical approximations of μ_{jk} and the ε -behavior
 586 of \mathfrak{S}_{jk} breakdown for extremely small values of ε . For example, in the discrete setting, it is highly unlikely that $\lambda_n = 0$ is (exactly) a numerical
 587 eigenvalue solution of Eq. (30), even though in the continuum setting $\lambda = 0$ is an accumulation point^{28,56} of the discrete spectra for the
 588 compact^{9,10} operator M . Therefore, our numerical simulations can probe the ε -behavior of \mathfrak{S}_{jk} for moderately small values of ε , but the
 589 approximation ultimately breaks down in the limit $\varepsilon \rightarrow 0$. However, for moderately small values of ε , our description above regarding the
 590 relationship between μ_{jk} and the ε -behavior of \mathfrak{S}_{jk} is still valid—illustrating that the details of the spectral measure μ_{jk} near the spectral origin
 591 $\lambda = 0$ strongly influence the ε -behavior of \mathfrak{S}_{jk} when $\varepsilon \ll 1$.

592 These concepts are illustrated in our computations of μ_{jk} and \mathfrak{S}_{jk} for “cat’s eye” flow displayed in Sec. V B 2. As the free parameter α
 593 increases from 0 to 1, the flow transitions from cell flow with closed streamlines to shear flow in the $y = x$ direction, as shown in Fig. 1. Our
 594 computations of μ_{jk} display a transitional behavior near $\lambda = 0$ which gives rise to a pronounced change in the ε -behavior of \mathfrak{S}_{jk} near $\varepsilon = 0$, as
 595 well as a significant enhancement in \mathfrak{S}_{kk} above the bare diffusive value ε .

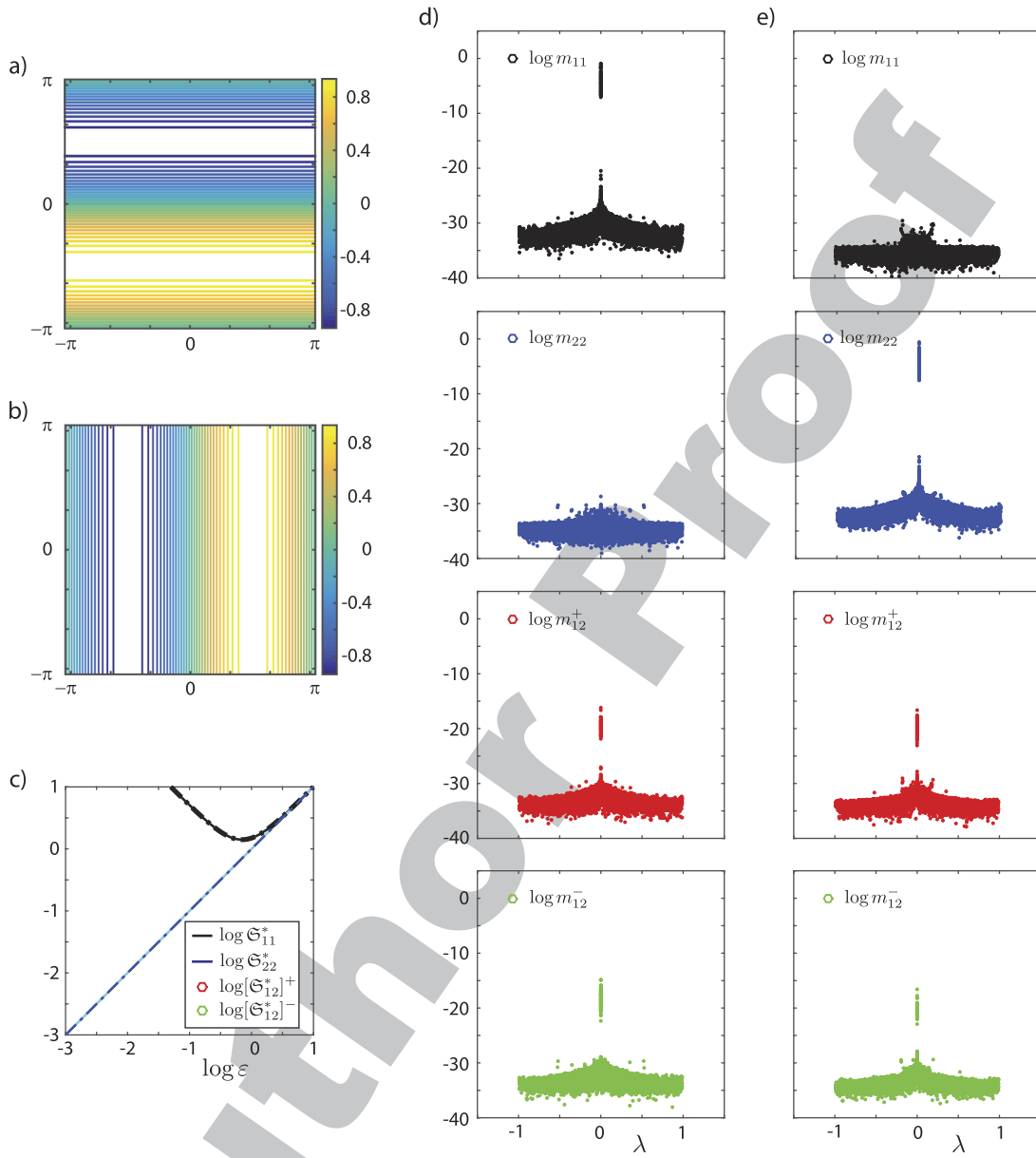
596 As a benchmark result, we demonstrate in Sec. V B 1 that our computations accurately capture the known behavior of μ_{kk} and \mathfrak{D}_{kk}^* for
 597 shear flow in the k th direction,⁴ where $\mu_{kk} = \mu_{kk}^0 \delta_0(d\lambda)$ and $\mathfrak{D}_{kk}^* = \varepsilon + \mu_{kk}^0/\varepsilon$. As another benchmark result, we demonstrate in Sec. V B 2 that
 598 our computations accurately capture the known^{17,18} asymptotic behavior $\mathfrak{D}_{kk}^* \sim \varepsilon^a$ with critical exponent $a = 1/2$, for $\varepsilon \ll 1$. In particular, the
 599 numerical methods developed in this manuscript compute $a \approx 0.54$, with an 8% error relative to the true value. For the sake of comparison,
 600 our Fourier approach to computing the spectral measure μ_{kk} discussed in Ref. 44 computes $a \approx 0.52$, with a 4% relative error, and our imple-
 601 mentation of the linear systems approach to computing \mathfrak{D}_{kk}^* discussed in Ref. 48 computes $a \approx 0.49$ with a 2% relative error. This marked
 602 increase in the accuracy of the linear systems approach is largely due to the ability to handle larger matrix sizes which, in turn, is due to the
 603 $O(N^2)$ numerical complexity of the method compared to the $O(N^3)$ numerical complexity of the spectral measure method.

604 1. BC-shear flow

605 In the continuum setting, it is known⁴ for shear flow in the x -direction that the measure μ_{11} is given by a δ -measure concentrated at
 606 the spectral origin, while $\mu_{22} \equiv 0$, and similarly for shear flow in the y -direction. As a baseline result, we computed the spectral measures
 607 and effective diffusivities for BC-shear-flow in both the x and y directions, which are obtained for parameter values $(B, C) = (0, 1)$ and (B, C)
 608 = $(1, 0)$, respectively. Our computations for the components μ_{jk} , $j, k = 1, 2$, of the spectral measure for BC-shear-flow displayed in Fig. 2 are in
 609 good agreement with the theoretical prediction in Ref. 4.

610 Figure 2 displays the streamlines for BC-shear-flow in (a) the x -direction and (b) the y -direction. In Fig. 2(c), the components \mathfrak{S}_{jk}^* ,
 611 $j, k = 1, 2$, of the effective diffusivity matrix are displayed for BC-shear-flow in the x -direction. The analogous result for BC-shear-flow in
 612 the y -direction is visually identical to Fig. 2(c) under the mapping $\mathfrak{S}_{11}^* \leftrightarrow \mathfrak{S}_{22}^*$, i.e., under the exchange of the colors black \leftrightarrow blue. The
 613 components μ_{jk} , $j, k = 1, 2$, of the spectral measure are displayed for BC-shear-flow in (d) the x -direction and (e) the y -direction.

614 We focus our discussion on the results for BC-shear-flow in the x -direction, as the discussion regarding BC-shear-flow in the y -direction
 615 is analogous. For all $n = 1, \dots, K_1$, the spectral weights $m_{22}(n)$ in Fig. 2(d) satisfy $m_{22}(n) \lesssim 10^{-29}$. With the effects of finite resolution ($L < \infty$)
 616 and roundoff error associated with a machine epsilon of $\sim 10^{-16}$, these spectral weights can be considered “numerically zero.” The spectral
 617 weights $m_{12}^\pm(n)$ satisfy $m_{12}^\pm(n) \lesssim 10^{-28}$ for λ_n away from the spectral origin $\lambda = 0$ with a peak near $\lambda = 0$ having magnitudes $m_{12}^\pm(n) \lesssim 10^{-16}$. The
 618 spectral weights for the x -direction satisfy $m_{11}(n) \lesssim 10^{-28}$ away from $\lambda = 0$, while the weights near $\lambda = 0$ satisfy $10^{-9} \lesssim m_{11} \lesssim 10^{-1}$, resembling



619
620
621
622 **FIG. 2.** Shear flow baseline result. The streamlines of BC-shear-flow in (a) the x-direction and (b) the y-direction. (c) The ε behavior of \mathfrak{G}_{jk}^* , $j, k = 1, 2$, for shear flow in the x-direction. The weights m_{jk} of the spectral measure $\text{Re } \mu_{jk}$ for shear flow in (d) the x-direction and (e) the y-direction as a function of λ . Consistent with theoretical predictions, the measure associated with the direction of the flow resembles a delta measure centered at the origin, while the other two components have spectral weights m_{jk} with very small magnitudes.

623 a δ -measure with virtually all of its mass concentrated near $\lambda = 0$. This is consistent with theoretical predictions.⁴ Due to the antisymmetry of
624 the *real-valued* matrix $U_1^T H U_1$, its complex eigenvectors and purely imaginary eigenvalues come in complex conjugate pairs.²⁵ Consequently,
625 the eigenvalues of the Hermitian matrix $-i U_1^T H U_1$ come in \pm pairs with identical spectral weights, resulting in the symmetry about $\lambda = 0$
626 displayed by the spectral measures in Fig. 2.

627 Due to the high concentration of measure mass in μ_{11} very near the spectral origin, our computation of \mathfrak{G}_{11}^* displayed in Fig. 2(c)
628 behaves like it is being governed by a delta function concentrated at the origin. In particular, Fig. 2(c) shows that the computed ε -behavior
629 of \mathfrak{G}_{11}^* , displayed in black color with solid line-style, lays right on top of the graph of its upper bound $\varepsilon[1 + \mu_{11}^0/\varepsilon^2]$ given in (24), with
630 $\mu_{11}^0 \approx 4.975 \times 10^{-1}$, displayed in black color and dashed-dotted line-style. (We had to increase the linewidth of the upper bound to be able

to distinguish between the two black lines.) Due to the extremely small magnitudes of the spectral weights m_{22} and m_{12}^\pm , with measure masses $\mu_{22}^0 \approx 5.33 \times 10^{-29}$, $[\mu_{12}^0]^+ \approx 1.03 \times 10^{-16}$, and $[\mu_{12}^0]^- \approx 3.34 \times 10^{-15}$, both the upper and lower bounds for \mathfrak{S}_{22}^* and \mathfrak{S}_{12}^* in Eqs. (24) and (25) are very close to ε and 0, respectively; the graph of \mathfrak{S}_{22}^* is virtually right on top of the lower bound ε in cyan color and solid line-style, and the magnitudes of $[\mathfrak{S}_{12}^*]^+$ and $[\mathfrak{S}_{12}^*]^-$ are so small they do not even appear. Since the support of the spectral measure is contained in the interval $[-1, 1]$, the components of the effective diffusivity approach their bare diffusive value $\varepsilon\delta_{jk}$ for large ε , as discussed above.

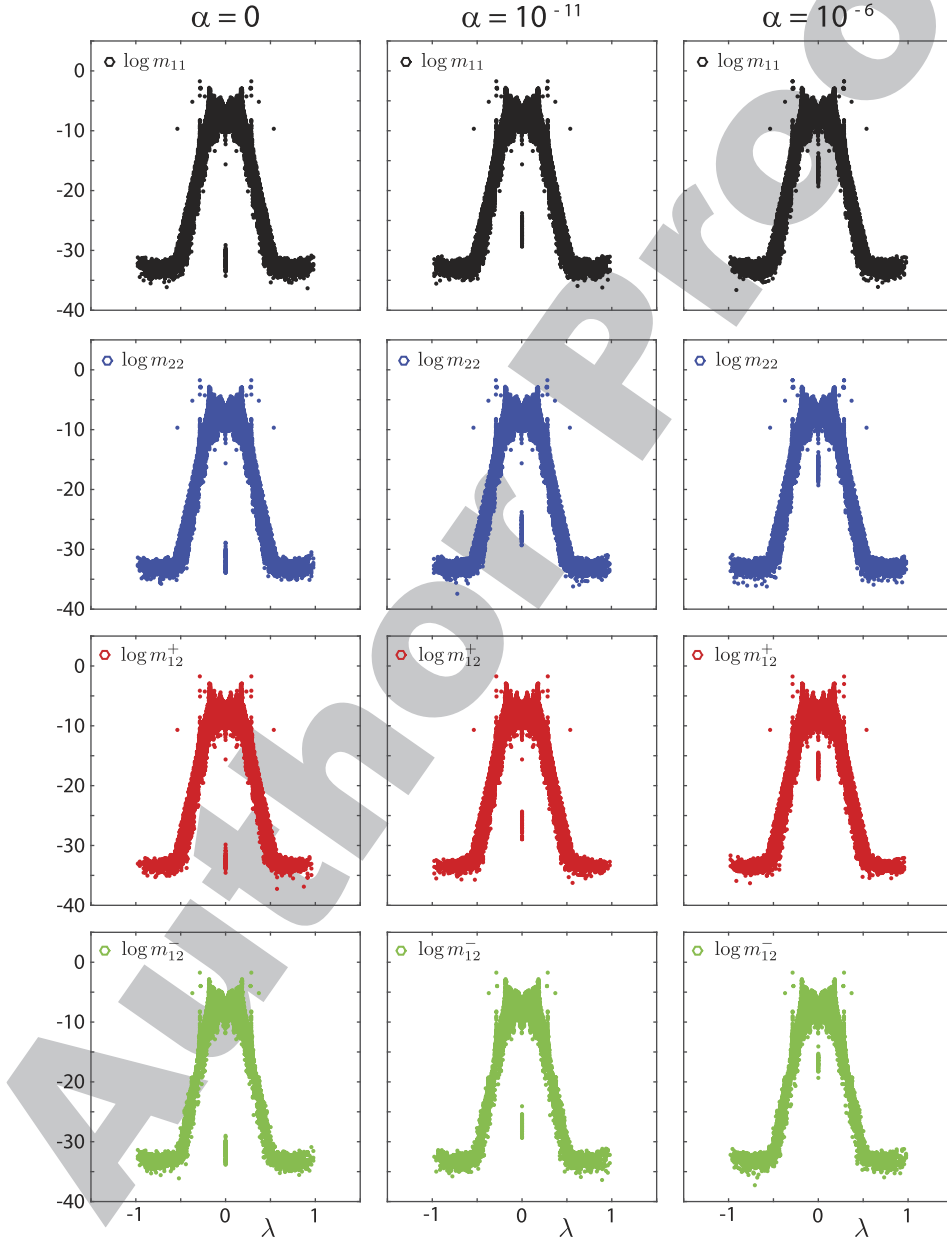


FIG. 3. Transition away from cat's eye cell flow. The spectral weights m_{jk} for the components $\text{Re } \mu_{jk}, j, k = 1, 2$, of the spectral measure are displayed with increasing values of the free parameter α from left to right. As the parameter α increases, the streamlines of the flow transition away from cell structures to open channels. This is reflected in the measure by a dramatic increase in the magnitude of the spectral weights m_{jk} associated with the "accumulation point" of the measure at $\lambda = 0$, while the other weights change only slightly.

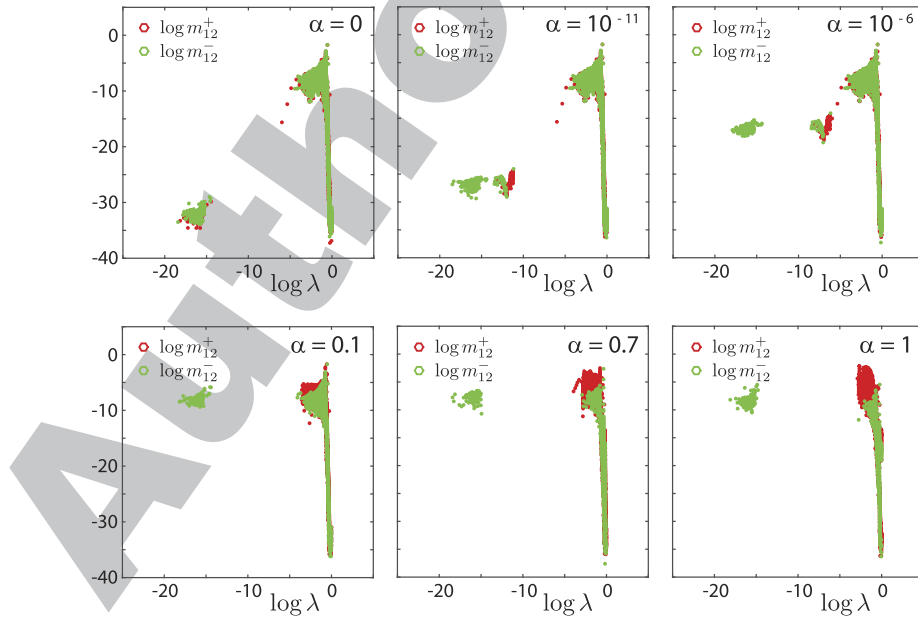
640 In Ref. 44, we developed Fourier methods for the computation of the spectral measure μ_{jk} for BC-cell flow, with $B = C = 1$. In particular,
 641 the eigenvalue problem $M\varphi_n = \lambda_n\varphi_n$ associated with the operator $M = -i\Delta^{-1}[\mathbf{u} \cdot \nabla]$ was transformed into an infinite algebraic system of
 642 equations defining a discrete, generalized eigenvalue problem. The Fourier coefficients of the eigenfunctions φ_n , $n = 1, 2, 3, \dots$, for the continuum
 643 setting comprise the components of the generalized eigenvectors in the discrete setting. Since we already treated BC-cell flow in Ref. 44,
 644 and for the sake of brevity, we now turn our attention to a discussion regarding our numerical results for “cat’s eye flow” displayed in Fig. 3.

645 2. Cat’s eye flow

646 Since the streamlines for cat’s eye flow in Fig. 1 are symmetric about the line $y = x$ for all $\alpha \in [0, 1]$, as discussed above, we anticipate
 647 that $\mu_{11} = \mu_{22}$. Our computations of the components μ_{jk} , $j, k = 1, 2$, of the spectral measure shown in Figs. 3 and 5 display this symmetry. A
 648 closer look at these figures reveals a deeper symmetry, namely, that $\mu_{11} = \mu_{22} = |\mu_{12}|$, where $|\mu_{12}| = \mu_{12}^+ + \mu_{12}^-$ is the total variation of the signed
 649 measure μ_{12} introduced in Eq. (27), i.e., superimposing the panels for m_{12}^+ and m_{12}^- in Figs. 3 and 5 yields the figure panels for m_{11} and m_{22} .
 650 We have also numerically verified the behavior $\mu_{11} = \mu_{22} = |\mu_{12}|$.

651 Since the operator $A = \Delta^{-1}[\nabla \cdot \mathbf{u}]$ is compact,^{9,10} its spectrum is discrete with an accumulation point at the spectral origin $\lambda = 0$.⁵⁶ This
 652 accumulation point behavior of the measures μ_{jk} , $j, k = 1, 2$, can be seen in all of the panels of Fig. 3. When the parameter $\alpha = 0$, the streamlines
 653 of cat’s eye flow are closed cell structures, as shown in Fig. 1, so that large scale transport occurs only when $\varepsilon > 0$.¹⁷ In this case, the computed
 654 “accumulation point” has eigenvalues λ_n with very small magnitude $10^{-19} \lesssim |\lambda_n| \lesssim 10^{-14}$. (It is clear that a finite number of eigenvalues do not
 655 constitute an accumulation point, but we will use this terminology to identify the concentration of eigenvalues near $\lambda = 0$ shown in Figs. 3–5
 656 and to set ideas.) However, the spectral measure weights $m_{kk}(n)$ and $m_{jk}^\pm(n)$ of the accumulation point have even smaller magnitudes with
 657 $10^{-35} \lesssim m_{kk}(n) \lesssim 10^{-29}$ and similarly for $m_{jk}^\pm(n)$, as shown in Fig. 3. Consequently, this component of the spectral measure does not contribute
 658 significantly to the enhancement $\mathcal{E}_{jk}(\varepsilon) = \varepsilon \sum_n m_{jk}(n) / (\varepsilon^2 + \lambda_n^2)$ of $\mathfrak{S}_{jk}^*(\varepsilon) = \varepsilon \delta_{jk} + \mathcal{E}_{jk}(\varepsilon)$. Plotting the panels of Fig. 3 with the log scale x -axis
 659 reveals that there is a *gap* in the spectral measure with no spectra in the interval $10^{-14} \lesssim |\lambda_n| \lesssim 10^{-7}$, as shown in Fig. 4. The other component
 660 of the spectral measure has spectra in the interval $10^{-7} \lesssim |\lambda_n| \lesssim 10^0$ and weights $10^{-37} \lesssim m_{kk}(n) \lesssim 10^{-1}$. However, the part of this component
 661 of the spectral measure with spectral weights having more significant magnitudes $10^{-4} \lesssim m_{kk}(n) \lesssim 10^{-1}$ are associated with eigenvalues with
 662 magnitude $|\lambda_n| \gtrsim 10^{-1}$ and consequently also do not contribute significantly to the enhancement \mathcal{E}_{jk} .

663 When $0 < \alpha \ll 1$, open channels connect neighboring cells and large scale transport takes place both in thin boundary layers and within
 664 the channels.¹⁷ This is reflected in the spectral measure $d\mu_{jk}(\lambda) = \sum_n \langle m_{jk}(n) \delta_{\lambda_n} \rangle d\lambda$ in Eq. (50) by a dramatic increase in the magnitude of
 665 the spectral weights $m_{kk}(n)$ and $m_{jk}^\pm(n)$ associated with the accumulation point—by more than 14 orders of magnitude with $10^{-19} \lesssim m_{kk}(n) \lesssim 10^{-15}$ —corresponding to a change of only 10^{-6} in the magnitude of α , as shown in Figs. 3 and 4. The associated change in the spectral
 666 weights away from $\lambda = 0$ is nominal. However, Fig. 4 reveals that as α increases from 0 to 10^{-6} a localized portion of the accumulation point



668 FIG. 4. Migration of positive measure mass from the computed “accumulation point” near the spectral origin. As the free parameter α of cat’s eye flow increases from zero,
 669 the magnitude of the spectral weights m_{12}^\pm comprising the accumulation point increases dramatically. Moreover, the spectra associated with the positive weights m_{12}^+ migrate
 670 away from the spectral origin until the accumulation point is composed only of negative valued mass. The corresponding behavior for m_{kk} , $k = 1, 2$, is determined by the
 671 relation $\mu_{kk} = |\mu_{12}|$ between the components of the spectral measure $d\mu_{jk}(\lambda) = \sum_n \langle m_{jk}(n) \delta_{\lambda_n} \rangle d\lambda$.

begins to migrate away from $\lambda = 0$ to the other component of the spectral measure with spectra in the interval $10^{-7} \lesssim |\lambda_n| \lesssim 10^0$ —decreasing the mass of the accumulation point for μ_{kk} . Moreover, all of the positive masses $m_{12}^+(n)$ migrate away from the accumulation point so the accumulation point of μ_{12} becomes comprised with purely negative weights. From this discussion, it is clear that the increased magnitudes of the masses comprising the accumulation point provide an increased contribution to the enhancement $\mathcal{E}_{jk}(\varepsilon)$ for $\varepsilon \sim 10^{-14}$, for example, but only a moderate increase, and the increase in $\mathcal{E}_{jk}(\varepsilon)$ for $10^{-7} \lesssim \varepsilon \lesssim 10^0$ is also not significant.

As the value of α increases to $\alpha = 1$, the magnitudes of the masses comprising the accumulation point increase until they reach maximum values with $10^{-11} \lesssim m_{kk}(n) \lesssim 10^{-5}$, associated with eigenvalues with magnitudes $10^{-19} \lesssim |\lambda_n| \lesssim 10^{-14}$, as shown in Fig. 4. This marked increase in the magnitudes of the spectral weights provide a significant contribution to the enhancement $\mathcal{E}_{jk}(\varepsilon)$ for $\varepsilon \sim 10^{-14}$, for example. Moreover, as

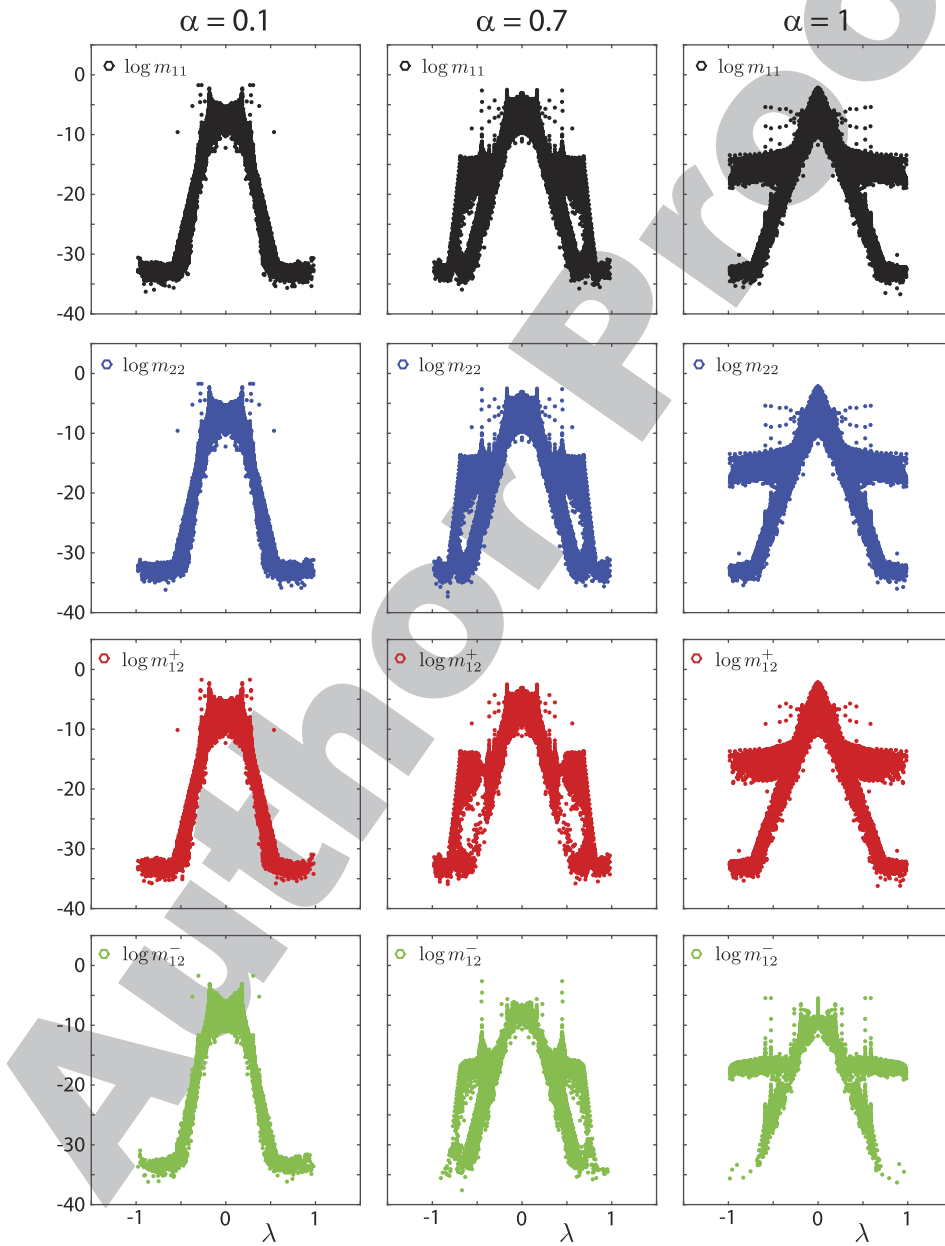


FIG. 5. Transition toward cat's eye shear flow. The spectral weights m_{jk} for the components $\text{Re } \mu_{jk}, j, k = 1, 2$, of the spectral measure are displayed with increasing values of the free parameter α from left to right. As the value of the parameter α increases, the streamlines become more elongated in the $x - y$ diagonal direction, becoming shear flow when $\alpha = 1$. This is reflected in the spectral measure by an increase in the breadth of the spectral region with significant measure mass.

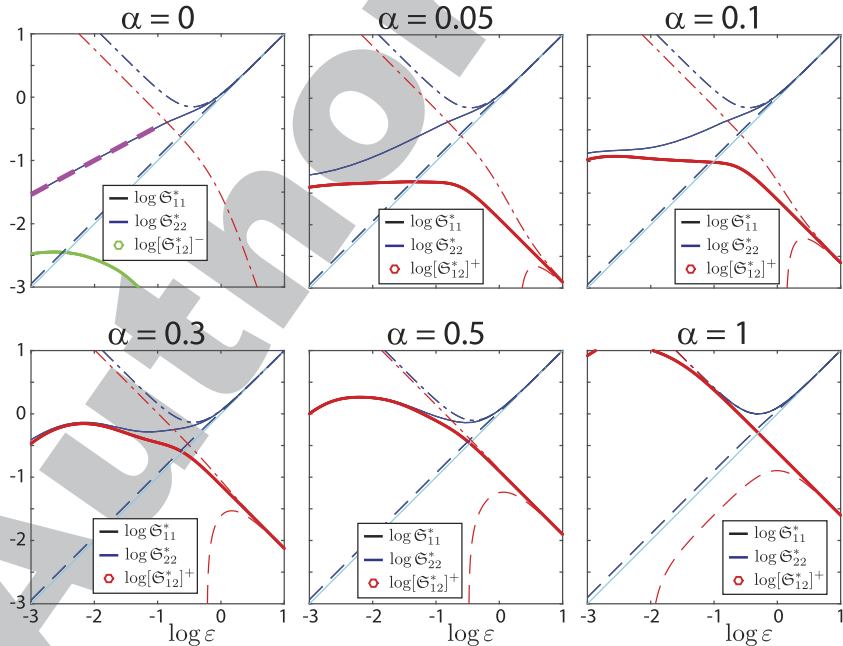
683 α increases in the range $(10^{-1}, 10^0)$, a significant transitional behavior arises in the other component of the spectral measure away from $\lambda = 0$,
 684 as shown in Figs. 4 and 5. In particular, a bulge of measure weights with significant magnitude forms for eigenvalues in the range $10^{-4} \lesssim |\lambda_n| \lesssim$
 685 10^{-1} , with a marked increase in weight magnitude from $10^{-7} \lesssim m_{kk}(n) \lesssim 10^{-4}$ to $10^{-7} \lesssim m_{kk}(n) \lesssim 10^{-2}$. This provides a significant contribution
 686 to the enhancement $\mathcal{E}_{jk}(\varepsilon)$ even for $10^{-4} \lesssim \varepsilon \lesssim 10^{-1}$.

687 The behavior of \mathfrak{S}_{jk}^* that we deduced from the behavior of the spectral measure μ_{jk} is consistent with our computations of the components
 688 $\mathfrak{S}_{jk}^*, j, k = 1, 2$, of the matrix \mathfrak{S}^* , which are displayed in Fig. 6. Since the support of the spectral measure μ_{jk} is contained in the interval $[-1, 1]$,
 689 the components \mathfrak{S}_{jk}^* of the effective diffusivity approach their bare diffusive value $\varepsilon\delta_{jk}$ as ε surpasses $\varepsilon = 1$, as discussed in the beginning of
 Sec. V B.

690 For cat's eye cell-flow, when $\alpha = 0$ the log-log plot of \mathfrak{S}_{kk}^* displays a linear trend for $10^{-3} \lesssim \varepsilon \lesssim 10^{-1}$, capturing the known^{17,18} power law
 691 behavior $\mathfrak{S}_{kk}^* \sim \varepsilon^a$ as $\varepsilon \rightarrow 0$. The polynomial fit $P(\varepsilon)$ to this line is given by $P(\varepsilon) = 0.54\varepsilon + 0.08$. This calculation of the critical exponent $a = 0.54$
 692 has an 8% error relative to the value of the theoretical result $a = 1/2$.^{17,18} The presence of spectral weights with magnitudes $10^{-7} \lesssim m_{kk}(n) \lesssim$
 693 10^{-4} and associated eigenvalues $10^{-4} \lesssim |\lambda_n| \lesssim 10^{-1}$ gives rise to a moderate enhancement in \mathfrak{S}_{kk}^* . This enhancement increases from a fraction
 694 of an order of magnitude to one and a half orders of magnitude above its bare diffusive value ε , as ε decreases from 10^{-1} – 10^{-3} , as shown in
 695 Fig. 3 for $\alpha = 0$.

696 We deduced from Fig. 3 that for $\alpha \in (0, 10^{-2})$ the behavior of the spectral measure gives rise to only a moderate enhancement
 697 $\mathcal{E}_{jk}(\varepsilon) = \varepsilon \sum_n m_{jk}(n)/(\varepsilon^2 + \lambda_n^2)$ of the effective diffusivity $\mathfrak{S}_{jk}^*(\varepsilon) = \varepsilon\delta_{jk} + \mathcal{E}_{jk}(\varepsilon)$ both for the advection dominated regime where $\varepsilon \sim 10^{-14}$, for
 698 example, and for the transitional regime $10^{-3} \lesssim \varepsilon \lesssim 10^{-1}$. This is consistent with the behavior of \mathfrak{S}_{jk}^* shown in Fig. 6 for $\alpha = 0$ and $\alpha = 0.05$.
 699 We further deduced from Figs. 4 and 5 that for $\alpha \in (10^{-2}, 1)$ the behavior of the spectral measure gives rise to a significant enhance-
 700 ment for both $\varepsilon \sim 10^{-14}$ and $10^{-3} \lesssim \varepsilon \lesssim 10^{-1}$ where there is a marked increase in spectral weight magnitude from $10^{-7} \lesssim m_{kk}(n) \lesssim 10^{-4}$ to
 701 $10^{-7} \lesssim m_{kk}(n) \lesssim 10^{-2}$ for eigenvalues satisfying $10^{-4} \lesssim |\lambda_n| \lesssim 10^{-1}$. This is consistent with the panels of Fig. 6 corresponding to $0.1 \leq \alpha \leq 1$,
 702 with \mathfrak{S}_{jk}^* enhanced many orders of magnitude above its bare diffusive value $\delta_{jk}\varepsilon$, and \mathfrak{S}_{kk}^* as well as \mathfrak{S}_{12}^* closely following their upper bounds for
 703 $\varepsilon \gtrsim 10^{-0.5}$ when $\alpha = 1$.

704 We conclude this section with a description of various symmetries arising in our numerical computations and their consequences. We
 705 discussed above that our computations of $\mu_{jk}, j = 1, 2$, display the symmetry $\mu_{11} = \mu_{22} = |\mu_{12}|$. This gives rise to the symmetry $\mathfrak{S}_{11}^*(\varepsilon) = \mathfrak{S}_{22}^*(\varepsilon) =$
 706 $\varepsilon + \mathcal{E}_{12}(\varepsilon; \mu_{12}^+) + \mathcal{E}_{12}(\varepsilon; \mu_{12}^-)$ between the components of the effective diffusivity, where we have denoted $\mathcal{E}_{jk}(\varepsilon; \mu_{jk}) = \varepsilon \int d\mu_{jk}(\lambda)/(\varepsilon^2 + \lambda^2)$, e.g.,

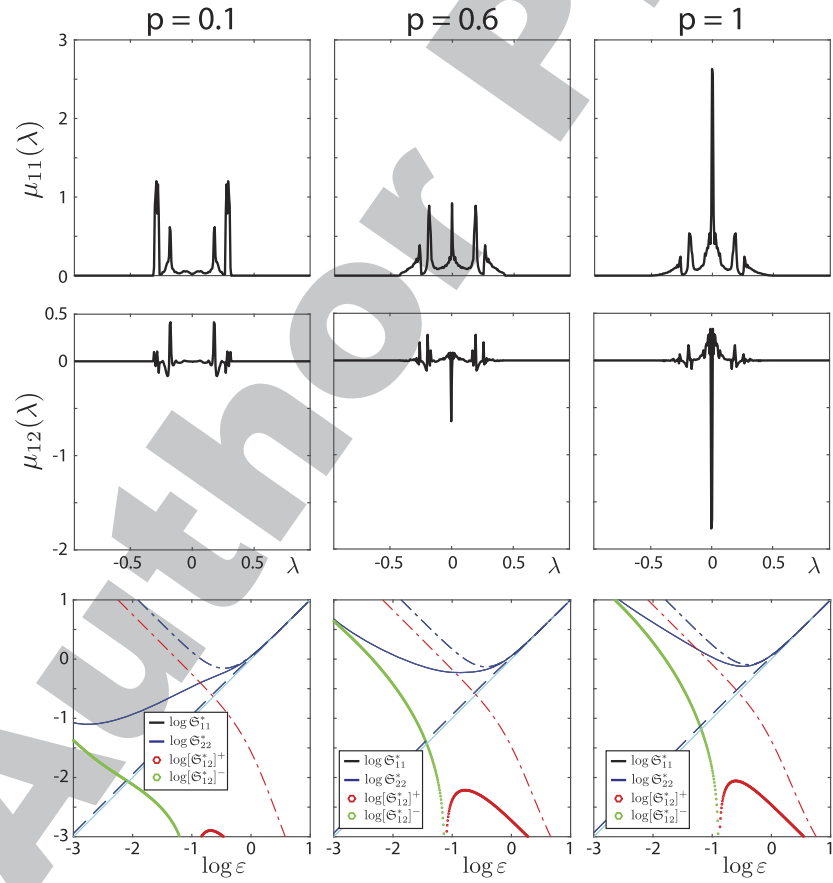


707 **FIG. 6.** Transitional behavior of the effective diffusivity from cat's eye cell flow to shear flow. The behavior of the components $\mathfrak{S}_{jk}^*, j, k = 1, 2$, of the effective diffusivity as
 708 a function of the nondimensionalized molecular diffusivity ε and increasing values of the free parameter α from left to right and top to bottom. The upper and lower bounds
 709 corresponding to \mathfrak{S}_{jk}^* are in dashed-dotted and dashed line-style, respectively, and are the same line colors as the line colors for $\mathfrak{S}_{kk}^*, k = 1, 2$, and red for \mathfrak{S}_{12}^* . The trivial
 710 lower bound ε for \mathfrak{S}_{kk}^* is in cyan color and solid line-style. When the lower bound for \mathfrak{S}_{12}^* becomes negative, it tends to $-\infty$ in this log-scale. For $\alpha = 0$, a polynomial fit to
 711 \mathfrak{S}_{kk}^* is also displayed in magenta color and dashed line-style. As the value of the parameter α increases and the flow transitions from the cell to shear structure, there is a
 712 substantial enhancement in the effective diffusivity for small values of ε .

713 $\mathfrak{S}_{11}^*(\varepsilon) = \varepsilon + \mathcal{E}(\varepsilon; \mu_{11})$. The symmetry $\mathfrak{S}_{11}^* = \mathfrak{S}_{22}^*$ can be clearly seen in our computations of \mathfrak{S}_{jk}^* , $j, k = 1, 2$, displayed in Fig. 6; the two curves
 714 lay right on top of one another, as do their upper and lower bounds as $\mu_{11}^0 = \mu_{22}^0$. We have also numerically explored the empirical relationship
 715 $\mathfrak{S}_{11}^* \approx \varepsilon + [\mathfrak{S}_{12}^*]^+ + [\mathfrak{S}_{12}^*]^-$ by plotting \mathfrak{S}_{11}^* and $\varepsilon + [\mathfrak{S}_{12}^*]^+ + [\mathfrak{S}_{12}^*]^-$ on one graph. For most values of α and ε considered, the three curves
 716 lay virtually on top of each other (not shown), and when there is a deviation of $\varepsilon + [\mathfrak{S}_{12}^*]^+ + [\mathfrak{S}_{12}^*]^-$ from \mathfrak{S}_{11}^* , it is slight. This property
 717 also leads to the inequalities $\mathfrak{S}_{11}^* \geq \varepsilon + [\mathfrak{S}_{12}^*]^+$ and $\mathfrak{S}_{11}^* \geq \varepsilon + [\mathfrak{S}_{12}^*]^-$, with $\mathfrak{S}_{11}^* = \mathfrak{S}_{22}^*$, which is consistent with the behavior of \mathfrak{S}_{jk}^* shown
 in Fig. 6.

718 3. Randomly perturbed cat's eye flow

719 We now discuss our computations of the components μ_{jk} and \mathfrak{S}_{jk}^* , $j, k = 1, 2$, of the spectral measure and effective diffusivity matrix,
 720 respectively, for randomly perturbed cat's eye flow with α uniformly distributed on the interval $[0, p]$. For each statistical trial of a sample
 721 space Ω_0 , with $|\Omega_0| \sim 10^3$ and $L = 100$, we computed *every* eigenvalue λ_n^1 and eigenvector r_n^1 , $n = 1, \dots, K_1$, of the matrix $-\imath U_1^T H U_1$ to form
 722 the spectral measure μ_{jk} in Eq. (50). In order to visually determine the behavior of the function $\mu_{jk}(\lambda) = \langle Q(\lambda) \widehat{\mathbf{e}}_j, \widehat{\mathbf{e}}_k \rangle$ underlying the spectral
 723 measure μ_{jk} , we plot a histogram representation of $\mu_{jk}(\lambda)$ called the *spectral function*, which we will also denote by $\mu_{jk}(\lambda)$. We now describe
 724 how we computed this graphical representation of the measure μ_{jk} . First, the spectral interval $I \supseteq \Sigma$ was divided into V subintervals I_v ,
 725 $v = 1, \dots, V$, of equal length. In our computations of the spectral functions, we typically used $V \sim 10^2$. Second, for fixed v , we identified all of
 726 the eigenvalues that satisfy $\lambda_n^1(\omega) \in I_v$, for $n = 1, \dots, K_1$ and $\omega \in \Omega_0$. The assigned value of $\mu_{jk}(\lambda)$ at the midpoint λ of the interval I_v is the sum
 727 of the spectral weights $m_{jk}(\omega)$ associated with all such $\lambda_n^1(\omega) \in I_v$, normalized by $|\Omega_0|$. In this way, the area underneath the curve is the measure
 728 mass μ_{jk}^0 .



729 **FIG. 7.** Spectral functions and effective diffusivities for randomly perturbed cat's eye flow. The random parameter α is uniformly distributed on the interval $[0, p]$. The spectral
 730 functions $\mu_{jk}(\lambda)$ are displayed with the corresponding effective diffusivities \mathfrak{S}_{jk}^* directly below for various values of p , increasing from left to right. As p increases and the
 731 streamlines of the flow become more elongated in the $x - y$ direction, on average, the region about the spectral origin $\lambda = 0$ with substantial measure mass increases in
 732 breadth and magnitude. This gives rise to a substantial enhancement in the components \mathfrak{S}_{jk}^* of the effective diffusivity for larger values of the nondimensionalized molecular
 733 diffusivity ε . The color scheme of the panels for \mathfrak{S}_{jk}^* is the same as that in Fig. 6.

734 Consistent with the symmetries of the randomly perturbed flow, our computations of the spectral function satisfy $\mu_{11}(\lambda) = \mu_{22}(\lambda)$; hence,
735 the ensemble averaged components \mathfrak{S}_{jk}^* of the effective diffusivity also satisfy $\mathfrak{S}_{11}^* = \mathfrak{S}_{22}^*$, as shown in Fig. 7. Similar to our computations for
736 nonrandom α , when $p = 0.1$, the measure mass of μ_{jk} , $j, k = 1, 2$, near the spectral origin $\lambda = 0$ is quite small and, on average, the region with
737 a significant magnitude increases in breadth as p increases, with the formation of a high concentration of measure mass at the spectral origin
738 $\lambda = 0$ as $p \rightarrow 1$ —due to the incorporation of statistical realizations with near shear-flow characteristics associated with $\alpha \approx 1$. This average
739 increase in the breadth of the region with significant mass and the formation of the high concentration of measure mass at $\lambda = 0$ give rise to a
740 substantial enhancement of the components \mathfrak{S}_{jk}^* of the effective diffusivity above the bare molecular diffusivity values $\varepsilon\delta_{jk}$. The sign changes
741 in $\mu_{12}(\lambda)$ give rise to sign changes in $\mathfrak{S}_{12}^* = [\mathfrak{S}_{12}^*]^+ - [\mathfrak{S}_{12}^*]^-$. In the log-log plot of \mathfrak{S}_{12}^* , a negative singularity forms in \mathfrak{S}_{12}^* at the location of
742 sign changes.

743 VI. CONCLUSIONS

744 We adapted and extended two methods previously introduced in Refs. 3, 4, 9, 10, and 48 to provide new Stieltjes integral representations
745 for the symmetric \mathfrak{S}^* and antisymmetric \mathfrak{A}^* parts of effective diffusivity matrix \mathfrak{D}^* in (19)—for all components of these homogenized matrices.
746 Each integral representation involves the nondimensionalized molecular diffusivity ε and a spectral measure of a self-adjoint operator
747 acting on an appropriate Hilbert space. We utilized these integral representations to derive rigorous bounds for the off-diagonal components
748 of the matrices \mathfrak{S}^* and \mathfrak{A}^* . We also proved that the spectral measures of both methods are identical, establishing that the two approaches
749 yield equivalent spectral representations for \mathfrak{D}^* .

750 We developed discrete formulations of these two mathematical frameworks involving matrix representations of the self-adjoint operators
751 and developed a standard and a *nonstandard* spectral theorem in terms of a standard and *generalized* eigenvalue problem, respectively. This
752 matrix analysis provided the Stieltjes integral representations for \mathfrak{S}^* and \mathfrak{A}^* in (19), involving discrete spectral measures given explicitly in
753 terms of the eigenvalues and eigenvectors of the matrices. We developed these discrete frameworks for both of the settings where the matrix
754 gradient ∇ has Dirichlet boundary conditions, for example, and is therefore *full-rank*, and where ∇ has periodic boundary conditions and is
755 therefore *rank-deficient*. In our studies of advection enhanced diffusion by a *periodic* fluid velocity field \mathbf{u} here, it is necessary to use a matrix
756 gradient ∇ with periodic boundary conditions. We also proved, in both the full-rank and rank-deficient settings, that the spectral measures of
757 both methods are identical, establishing that the two approaches yield equivalent spectral representations for the effective diffusivity matrix
758 \mathfrak{D}^* . More specifically, this matrix analysis demonstrates that both approaches can be formulated in terms of a common *standard* eigenvalue
759 problem involving a matrix with the *smaller size* encountered in the generalized eigenvalue problem, thus combining the beneficial numerical
760 attributes of both approaches.

761 We employed these discrete formulations to compute the components \mathfrak{S}_{jk}^* , $j, k = 1, \dots, d$, of the matrix \mathfrak{S}^* for some model 2D ($d = 2$)
762 periodic flows and randomly perturbed periodic flows, by directly computing the associated discrete spectral measure $\text{Re } \mu_{jk}$. As a base-
763 line result, we computed \mathfrak{S}_{jk}^* and $\text{Re } \mu_{jk}$ for *BC*-shear-flow, for which the spectral measure is known.⁴ Our numerical results are in good
764 agreement with the theoretical result. We also computed \mathfrak{S}_{jk}^* and $\text{Re } \mu_{jk}$ for the “cat’s eye” flow, for both the nonrandom and randomly
765 perturbed settings, as a function of a free parameter. As the parameter varies, the flow transitions from cell-flow to shear-flow in the dia-
766 gonal direction $y = x$. For cat’s eye cell-flow, our computations capture the known^{17,18} power law behavior $\mathfrak{S}_{kk}^* \sim \varepsilon^{1/2}$ for $\varepsilon \ll 1$. The spectral
767 measure $\text{Re } \mu_{jk}$ and \mathfrak{S}_{jk}^* have transitional behavior as the parameter varies. This reveals how the details of $\text{Re } \mu_{kk}$ near the spectral origin
768 govern the enhancement of \mathfrak{S}_{kk}^* above its bare diffusive value ε in the advection dominated regime where $\varepsilon \ll 1$ and similarly for \mathfrak{S}_{12}^* . Cons-
769 sistent with the symmetries of the flow, our computations indicate that $\text{Re } \mu_{11} = \text{Re } \mu_{22}$. Our computations of $\text{Re } \mu_{12}$ for cat’s eye flow also
770 suggest a deeper symmetry, namely, $|\text{Re } \mu_{12}| = \text{Re } \mu_{11} = \text{Re } \mu_{22}$, where $|\text{Re } \mu_{12}|$ is the total variation of the signed measure $\text{Re } \mu_{12}$. Our com-
771 putations of \mathfrak{S}_{jk}^* are consistent with these symmetries and rigorous bounds derived in Theorem 2. In order to streamline the presentation
772 of the main theoretical and numerical results in the body of the manuscript, we have placed more detailed developmental material in an
773 appendix.

774 In almost 30 years since the initial formulation^{3,4} of Stieltjes integral representations for the effective diffusivity matrix \mathfrak{D}^* , analytical
775 calculations of \mathfrak{D}^* have been obtained for only a few simple flows, such as shear flow. Our results help further advance the applicability of
776 this spectral measure approach by providing a mathematical foundation for computation of spectral representations of \mathfrak{D}^* . For randomly
777 perturbed periodic flows, the spectral method differs from more traditional methods in that it enables statistical investigation of the random
778 eigenvalues and eigenvectors, thus connecting homogenization of advection diffusion processes to random matrix theory.⁴⁵ The results in
779 this manuscript lay the groundwork for such investigations.

780 ACKNOWLEDGMENTS

781 We gratefully acknowledge support from the Applied and Computational Analysis Program and the Arctic and Global Prediction Pro-
782 gram at the U.S. Office of Naval Research through Grant Nos. N00014-12-10861, N00014-13-10291, and N00014-18-1-2552. We are also
783 grateful for support from the Division of Mathematical Sciences at the U.S. National Science Foundation (NSF) through Grant Nos. DMS-
784 0940249, DMS-1413454, DMS-1715680, DMS-1211179, and DMS-1522383. Finally, we would like to thank the NSF Math Climate Research
785 Network (MCRN) for their support of this work.

786 APPENDIX A: APPENDIX OVERVIEW

In order to streamline the presentation of the main theoretical and numerical results in the body of the manuscript, we have placed more detailed developmental material in a series of appendixes here. We now give an overview of the topics covered in this appendix. In Appendix B, we comment on the notation used throughout this manuscript. In Appendix C, we derive important properties of the linear operator $A = \Delta^{-1}[\mathbf{u} \cdot \nabla]$ defined in Eq. (11).

In Theorem 1 of Sec. III, we adapted and extended a method^{9,10,48} involving a self-adjoint operator M acting on a Sobolev space of scalar-valued functions which provides the Stieltjes integral representations for \mathfrak{S}^* and \mathfrak{A}^* in Eq. (19). In Appendix D, we adapt and extend a different method^{3,4} involving a self-adjoint operator M acting on the Hilbert space of curlfree vector-valued functions which also leads to the Stieltjes integral representations for \mathfrak{S}^* and \mathfrak{A}^* in Eq. (19). These results are summarized in Corollary 4 of Theorem 1.

In Theorem 5 of Appendix D, we prove that the spectral measures arising in Theorem 1 and Corollary 4 are identical, establishing that the two approaches yield equivalent spectral representations of \mathfrak{D}^* . This is accomplished by proving that the masses and all the moments of the two spectral measures are equal and citing the Hausdorff moment problem for measures with bounded support.^{1,58} In Corollary 6 of Theorem 5, we utilize a one-to-one isometric correspondence⁴⁴ between the Sobolev space arising in Theorem 1 and the Hilbert space arising in Corollary 4, to extend the results of Theorem 5 to every spectral measure associated with the two self-adjoint operators M and M . This corollary also proves that the masses and all the moments of the two spectral measures are equal in the generalized setting of a space-time periodic flow, possibly associated with chaotic dynamics and unbounded spectrum.⁴⁴ In the setting of unbounded spectrum, the Hamburger or Stieltjes moment problems are instead relevant, and more conditions must be met beyond the equality of the masses and moments to ensure that the measures are identical, such as Carleman's criterion.¹ In Ref. 44, an alternate method was used to determine that the spectral measures arising in the two different approaches are indeed identical in the time-dependent setting.

In Appendix E, we develop a discrete formulation of the mathematical framework given in Appendix D, involving a Hermitian matrix representation for the self-adjoint operator M . We also briefly review the standard spectral theorem for Hermitian matrices. This provides the Stieltjes integral representations for \mathfrak{S}^* and \mathfrak{A}^* in (19) involving a discrete spectral measure, given explicitly in terms of the eigenvalues and eigenvectors of the matrix. This discrete framework holds for the setting where the matrix gradient has Dirichlet boundary conditions, for example, and is therefore *full-rank*. These results are analogs of those in Theorem 3 and are summarized in Corollary 7. In Theorem 8, we develop a *projection method* that is used to generalize the results in Theorem 3 and Corollary 7 to the setting where the matrix gradient has periodic boundary conditions, for example, and is therefore *rank-deficient*. The results of Theorem 8 are also used to prove that the discrete spectral representations arising in Theorem 3 and Corollary 7 are equivalent in this rank-deficient setting.

Specifically, in Lemma 9 of Appendix F, we use the properties of the singular value decomposition of the matrix gradient ∇ to reveal symmetries between the two discrete approaches formulated in Sec. IV and Appendix E, establishing that the two approaches yield equivalent spectral representations of the effective diffusivity matrix \mathfrak{D}^* when ∇ is full-rank. In particular, we establish in the Proof of Lemma 9 that the eigenvalues and generalized eigenvalues underlying the spectral measures for each method are in fact eigenvalues of a Hermitian matrix arising in both methods. Moreover, the eigenvectors \mathbf{w}_n and generalized eigenvectors \mathbf{z}_n of the two methods are related by $\mathbf{w}_n = \nabla \mathbf{z}_n$, which leads to the equivalence of the discrete spectral measures of the two approaches.

In Theorem 10 of Appendix G, we generalize Lemma 9 to the rank-deficient setting. This generalizes both the numerical algorithms developed in Sec. IV and Appendix E to the setting of periodic boundary conditions and combines beneficial numerical attributes of each algorithm. In Sec. V, this common method is used to compute \mathfrak{S}^* for model flows and relate spectral characteristics to flow geometry and transport properties.

826 APPENDIX B: NOTATION

We now briefly discuss the notation used throughout the manuscript. Operators are denoted by capital letters, while functions comprising the domains of these operators are denoted by lowercase letters. (Capital letters are also used to denote the size of matrices.) Furthermore, the vector-valued functions are denoted by lowercase bold font, e.g., ξ , while the scalar-valued functions are denoted by lowercase nonbold font, e.g., ξ . Matrices denoted by capital Latin letters are in math-serif font, e.g., $H, B, C, Z, Q, A, U, V, W$, etc. Integrodifferential operators mapping scalar-valued functions to scalar-valued functions are in standard math-italic font, e.g., A and M . Integrodifferential operators mapping vector-valued functions to vector-valued functions are in math-boldface font, e.g., A and M . We use a similar notation for differential operators, e.g., $\nabla \xi$ and $-\Delta \xi$ and their discrete, matrix counterparts $\nabla \xi$ and $\nabla^T \nabla \xi$, respectively. All homogenized matrices are in Gothic font and have a superscript asterisk, e.g., \mathfrak{D}^* , \mathfrak{S}^* , and \mathfrak{A}^* .

835 APPENDIX C: PROPERTIES OF THE LINEAR OPERATOR A

In this section, we derive various properties of the linear operator $A = \Delta^{-1}[\mathbf{u} \cdot \nabla]$ defined in Eq. (11). In particular, we demonstrate that A is antisymmetric on the Hilbert space $\mathcal{H}^{1,2}$ defined in (8). Moreover, we show that A is bounded on $\mathcal{H}^{1,2}$ and we provide an upper bound for $\|A\|_{1,2}$ when \mathbf{u} is uniformly bounded on the period cell \mathcal{V} .

839 We first show that the incompressibility condition $\nabla \cdot \mathbf{u} = 0$ implies that the operator A is antisymmetric on $\mathcal{H}^{A,2}$ ^{9,10} i.e., $\langle Af, h \rangle_{1,2} =$
 840 $-\langle f, Ah \rangle_{1,2}$. On the Hilbert space \mathcal{H} defined in Eq. (7), the linear operator Δ^{-1} satisfies $\langle \Delta\Delta^{-1}f, h \rangle = \langle f, h \rangle$ in a distributional sense, for all
 841 $f, h \in \mathcal{H}$.^{19,37,44} Consequently, integration by parts and $\nabla \cdot \mathbf{u} = 0$ yields^{9,10,44,48}

$$\begin{aligned} 842 \langle Af, h \rangle_{1,2} &= \langle [\nabla(\Delta^{-1})(\mathbf{u} \cdot \nabla)f] \cdot \nabla h \rangle \\ 843 &= -\langle [(\mathbf{u} \cdot \nabla)f], h \rangle \\ 844 &= -\langle [\nabla \cdot (\mathbf{u}f)], h \rangle \\ &= \langle f, [(\mathbf{u} \cdot \nabla)h] \rangle \\ &= \langle f, [\Delta(\Delta^{-1})(\mathbf{u} \cdot \nabla)h] \rangle \\ &= -\langle \nabla f \cdot [\nabla(\Delta^{-1})(\mathbf{u} \cdot \nabla)h] \rangle \\ &= -\langle f, Ah \rangle_{1,2}, \end{aligned} \tag{C1}$$

845 for all $f, h \in \mathcal{H}^{A,2}$ and real-valued incompressible \mathbf{u} (see Ref. 44 for more details).

846 Now, we derive the bound for $\| A \|_{1,2}$ given in Eq. (14). From the Cauchy-Schwartz inequality $|\langle f, h \rangle| \leq \| f \| \| h \|$, we have

$$\begin{aligned} 847 \| Af \|_{1,2}^2 &= |\langle \nabla[\Delta^{-1}(\mathbf{u} \cdot \nabla f)] \cdot \nabla[\Delta^{-1}(\mathbf{u} \cdot \nabla f)], h \rangle| \\ 848 &= |-\langle [\Delta^{-1}(\mathbf{u} \cdot \nabla f)], (\mathbf{u} \cdot \nabla f) \rangle| \\ 849 &\leq \|\Delta^{-1}(\mathbf{u} \cdot \nabla f)\| \|\mathbf{u} \cdot \nabla f\| \\ 850 &\leq \|\Delta^{-1}\| \|\mathbf{u} \cdot \nabla f\|^2. \end{aligned} \tag{C2}$$

851 We now provide an upper bound for $\| \mathbf{u} \cdot \nabla f \|$ when the components $u_k, k = 1, \dots, d$, of the fluid velocity field \mathbf{u} are uniformly bounded on
 852 the period cell \mathcal{V} . By the Cauchy-Schwartz inequality, $|\xi \cdot \zeta| \leq |\xi||\zeta|$, we have

$$853 \|\mathbf{u} \cdot \nabla f\|^2 = \langle |\mathbf{u} \cdot \nabla f|^2 \rangle \leq \langle |\mathbf{u}|^2 |\nabla f|^2 \rangle \leq \sup_{x \in \mathcal{V}} |\mathbf{u}(x)|^2 \|f\|_{1,2}^2. \tag{C3}$$

854 The result in Eq. (14) is now clear.

APPENDIX D: CURLFREE FIELDS AND THE EFFECTIVE DIFFUSIVITY MATRIX

855 In this section, we adapt and extend an alternative method^{3,4} to the method discussed in Sec. III which leads to the integral representations
 856 for the symmetric \mathfrak{S}^* and antisymmetric \mathfrak{A}^* parts of the effective diffusivity matrix \mathfrak{D}^* in Eq. (19). More specifically, in Appendix D 1, we
 857 provide functional formulas for \mathfrak{S}^* and \mathfrak{A}^* that are analogous to the formulas in (11). We review a Hilbert space formulation of this effective
 858 parameter problem^{3,4,17,18,33} in Appendix D 2 which leads to a resolvent formula for $\nabla \chi_j$ that is analogous to the resolvent formula for χ_j in
 859 (12), involving a self-adjoint operator. We use this result and the spectral theorem^{53,58} to provide the Stieltjes integral representations for \mathfrak{S}^*
 860 and \mathfrak{A}^* in (19), involving a spectral measure of the operator. Finally, we prove that the spectral measure corresponding to the Stieltjes integral
 861 representation for \mathfrak{D}^* in Eq. (19) of Theorem 1 is identical to the spectral measure corresponding the Stieltjes integral representation for \mathfrak{D}^*
 862 developed in this section. This establishes that the two different approaches yield equivalent spectral representations of \mathfrak{D}^* .

1. Functional formulas for the effective diffusivity matrix

863 In this section, we derive functional formulas for the symmetric \mathfrak{S}^* and antisymmetric \mathfrak{A}^* parts of the effective diffusivity matrix \mathfrak{D}^*
 864 that are analogous to the formulas in Eq. (11). Using Eq. (29) and the representation of the fluid velocity field \mathbf{u} in (28), the advection diffusion
 865 equation in (1) can be written as a diffusion equation,^{17,18}

$$866 \phi_t = \nabla \cdot [\mathsf{D} \nabla \phi], \quad \phi(0, \mathbf{x}) = \phi_0(\mathbf{x}), \quad \mathsf{D} = \varepsilon \mathsf{I} + \mathsf{H}. \tag{D1}$$

867 Moreover, the cell problem in (4) can be written as a steady-state diffusion equation,^{17,18}

$$868 \nabla \cdot [\mathsf{D}(\nabla \chi_k + \mathbf{e}_k)] = 0, \quad \langle \nabla \chi_k \rangle = 0, \quad k = 1, \dots, d. \tag{D2}$$

869 Here, \mathbf{e}_k is a standard basis vector, $k = 1, \dots, d$, and $\mathsf{D}(\mathbf{x}) = \varepsilon \mathsf{I} + \mathsf{H}(\mathbf{x})$ can be viewed as a local diffusivity matrix with coefficients

$$870 \mathsf{D}_{jk} = \varepsilon \delta_{jk} + \mathsf{H}_{jk}, \quad j, k = 1, \dots, d, \tag{D3}$$

871 where δ_{jk} is the Kronecker delta and I is the identity operator on \mathbb{R}^d .

Substituting into Eq. (3) the expression for u_j in (4) and using Eq. (28), $\mathbf{u} = \nabla \cdot \mathbf{H}$, show that the components \mathfrak{S}_{jk}^* and \mathfrak{A}_{jk}^* of \mathfrak{S}^* and \mathfrak{A}^* can be written in terms of the following functional formulas involving the *real-valued* vector field $\nabla\chi_k$:

$$\mathfrak{S}_{jk}^* = \varepsilon(\delta_{jk} + \langle \nabla\chi_j \cdot \nabla\chi_k \rangle), \quad \mathfrak{A}_{jk}^* = \langle \mathbf{H} \nabla\chi_j \cdot \nabla\chi_k \rangle. \quad (\text{D4})$$

The functional formulas in (D4) are analogous to the functional formulas in Eq. (11). The symmetry $\mathfrak{S}_{jk}^* = \mathfrak{S}_{kj}^*$ of the matrix \mathfrak{S}^* follows from (D4) and the fact that the vector field $\nabla\chi_k$ is real-valued so that $\langle \nabla\chi_j \cdot \nabla\chi_k \rangle = \langle \nabla\chi_k \cdot \nabla\chi_j \rangle$. Moreover, the positivity condition $\langle \nabla\chi_k \cdot \nabla\chi_k \rangle = \langle |\nabla\chi_k|^2 \rangle \geq 0$ demonstrates that the effective transport of the scalar density ϕ is always *enhanced* by the presence of an incompressible velocity field, i.e., $\mathfrak{D}_{kk}^* = \mathfrak{S}_{kk}^* \geq \varepsilon$. The equality $\mathfrak{D}_{kk}^* = \mathfrak{S}_{kk}^*$ follows from the skew-symmetry of the matrix \mathfrak{A}^* , $\mathfrak{A}_{kj}^* = -\mathfrak{A}_{jk}^*$, hence $\mathfrak{A}_{kk}^* = 0$. The skew-symmetry of \mathfrak{A}^* follows from the skew-symmetry of the *real-valued* matrix \mathbf{H} , $\mathfrak{A}_{jk}^* = \langle \mathbf{H} \nabla\chi_j \cdot \nabla\chi_k \rangle = -\langle \nabla\chi_j \cdot \mathbf{H} \nabla\chi_k \rangle = -\langle \mathbf{H} \nabla\chi_k \cdot \nabla\chi_j \rangle = -\mathfrak{A}_{kj}^*$.

2. The analytic continuation method and integral representations of \mathfrak{D}^*

In this section, we begin by noting that the cell problem in Eq. (D2) is equivalent^{3,4,17,18} to the quasi-static limit of Maxwell's equations,^{22,27,40} which describe the transport properties of an electromagnetic wave in a composite material,

$$\nabla \times \mathbf{E}_k = 0, \quad \nabla \cdot \mathbf{J}_k = 0, \quad \mathbf{J}_k = \mathbf{D}\mathbf{E}_k, \quad \langle \mathbf{E}_k \rangle = \mathbf{e}_k, \quad \mathbf{D} = \varepsilon\mathbf{l} + \mathbf{H}. \quad (\text{D5})$$

Here, $\mathbf{E}_k = \nabla\chi_k + \mathbf{e}_k$ plays the role of the local electric field, $\mathbf{J}_k = \mathbf{D}\mathbf{E}_k$ plays the role of the local current density, and $\mathbf{D} = \varepsilon\mathbf{l} + \mathbf{H}$ plays the role of the local conductivity matrix of the medium. Since \mathbf{H} is skew-symmetric, the intensity-flux relation $\mathbf{J}_k = \mathbf{D}\mathbf{E}_k$ is not the usual Fourier law, but instead resembles that of a Hall medium.^{17,18,26,40}

In Refs. 3 and 4, the analytic continuation method for representing transport in composites was adapted to provide a Stieltjes integral representation for the symmetric part of the effective diffusivity matrix \mathfrak{D}^* , involving a spectral measure of a self-adjoint operator. This method provides Stieltjes integral representations for the bulk transport coefficients of composite media,²² such as the effective electrical conductivity. This method is based on the spectral theorem of Hilbert space theory and a resolvent formula for, say, the electric field, involving a self-adjoint operator²² or matrix⁴² which depends only on the composite geometry. In this section, we adapt the method developed in Refs. 3 and 4 to provide Stieltjes integral representations for *both* the symmetric and antisymmetric parts of the effective diffusivity matrix \mathfrak{D}^* , which encodes the flow geometry of the fluid velocity field in a spectral measure of a self-adjoint operator.

Following the discussion leading to Eq. (8), we consider a fluid velocity field that is spatially periodic on a region $\mathcal{V} \subset \mathbb{R}^d$ and define the Hilbert space \mathcal{H} ,^{18,33}

$$\mathcal{H} = \{\xi \in \otimes_{n=1}^d L^2(\mathcal{V}, v) : \xi(\mathbf{x}) \text{ is periodic in } \mathcal{V} \text{ and } \langle \xi \rangle = 0\}, \quad (\text{D6})$$

which is analogous to the Hilbert space \mathcal{H} defined in Eq. (7), where \mathcal{H} is defined over vector-fields instead of scalar-fields as in \mathcal{H} . The Hilbert space \mathcal{H} is equipped with a sesquilinear inner-product $\langle \cdot, \cdot \rangle$ defined by $\langle \xi, \zeta \rangle = \langle \xi \cdot \zeta \rangle$, with $\xi \cdot \zeta = \xi^\dagger \zeta$, \dagger is the operation of complex-conjugate-transpose, and $\langle \zeta, \xi \rangle = \overline{\langle \xi, \zeta \rangle}$ for $\xi, \zeta \in \mathcal{H}$. This inner-product induces a norm $\| \cdot \|$ defined by $\| \xi \| = \langle \xi, \xi \rangle^{1/2}$ and $\xi \in \mathcal{H}$ implies that $\| \xi \| < \infty$. Now consider the associated Hilbert space \mathcal{H}_x of curlfree fields,^{4,17,18,22,40,44}

$$\mathcal{H}_x = \{\xi \in \mathcal{H} : \nabla \times \xi = 0 \text{ weakly and } \langle \xi \rangle = 0\}. \quad (\text{D7})$$

The curlfree vector field $\nabla\chi_k$ in the cell problem in (D2) is mean-zero $\langle \nabla\chi_k \rangle = 0$. When the matrix \mathbf{D} in Eq. (D1) is bounded in the operator norm $\| \cdot \|$ induced by the \mathcal{H} -inner-product,²⁰ $\| \mathbf{D} \| < \infty$, then there exists unique $\nabla\chi_k \in \mathcal{H}_x$ satisfying Eq. (D2).^{22,46} We assume that

$$0 < \varepsilon < \infty, \quad \| \mathbf{H} \| < \infty, \quad (\text{D8})$$

which together imply $\| \mathbf{D} \| < \infty$.

The linear operator $\Gamma = \nabla(\Delta^{-1})\nabla \cdot$ is a projection onto the Hilbert space \mathcal{H}_x in the sense that $\Gamma : \mathcal{H} \mapsto \mathcal{H}_x$ and $\Gamma\xi = \xi$ (weakly) for all $\xi \in \mathcal{H}_x$, in particular, $\Gamma \nabla\chi_k = \nabla\chi_k$.^{17,44} It is based on convolution with respect to the Green's function for the Laplacian $\Delta = \nabla^2$.^{38,56} Applying the integrodifferential operator $\nabla\Delta^{-1}$ to the cell problem in Eq. (D2) yields $\Gamma[(\varepsilon\mathbf{l} + \mathbf{H})(\nabla\chi_k + \mathbf{e}_k)] = 0$. Since $\Gamma\mathbf{e}_k = 0$ and $\Gamma\nabla\chi_k = \nabla\chi_k$, this formula is equivalent to $(\varepsilon\mathbf{l} + \Gamma\mathbf{H}\Gamma)\nabla\chi_k = -\Gamma\mathbf{H}\mathbf{e}_k$, which yields the following resolvent formula for $\nabla\chi_k$:

$$\nabla\chi_k = (\varepsilon\mathbf{l} + \mathbf{A})^{-1}\mathbf{g}_k, \quad \mathbf{A} = \Gamma\mathbf{H}\Gamma, \quad \mathbf{g}_k = -\Gamma\mathbf{H}\mathbf{e}_k, \quad (\text{D9})$$

which is analogous to Eq. (12). Since Γ is a projection operator onto $\mathcal{H}_x \subset \mathcal{H}$, it is bounded by unity in operator norm on \mathcal{H} , $\| \Gamma \| \leq 1$.^{20,54} Integration by parts and the symmetry of the operator Δ^{-1} ⁵⁶ (or the projective nature of Γ itself) shows that Γ is also a *symmetric* operator, i.e., $\langle \Gamma\xi \cdot \zeta \rangle = \langle \xi \cdot \Gamma\zeta \rangle$ for all $\xi, \zeta \in \mathcal{H}$.⁴⁴ These two properties show that Γ with domain \mathcal{H} is a *self-adjoint* operator.⁵³ Since Γ is self-adjoint and $\Gamma\nabla\chi_k = \nabla\chi_k$, we may write \mathfrak{A}_{jk}^* in Eq. (D4) as $\mathfrak{A}_{jk}^* = \langle \mathbf{A} \nabla\chi_j \cdot \nabla\chi_k \rangle$. Consequently, substituting the resolvent formula for $\nabla\chi_k$ in Eq. (D9) into the functional formulas in Eq. (D4) yields

$$\mathfrak{S}_{jk}^* = \varepsilon(\delta_{jk} + \langle (\varepsilon\mathbf{l} + \mathbf{A})^{-1}\mathbf{g}_j \cdot (\varepsilon\mathbf{l} + \mathbf{A})^{-1}\mathbf{g}_k \rangle), \quad (\text{D10})$$

920

$$\mathfrak{A}_{jk}^* = \langle \mathbf{A} (\varepsilon \mathbf{l} + \mathbf{A})^{-1} \mathbf{g}_j \cdot (\varepsilon \mathbf{l} + \mathbf{A})^{-1} \mathbf{g}_k \rangle,$$

921 which is a direct analog of Eq. (13).

922 Since Γ is self-adjoint on \mathcal{H} , the antisymmetry of the matrix H implies that $\mathbf{A} = \Gamma \mathsf{H} \Gamma$ is an *antisymmetric* operator on \mathcal{H} , i.e., $\langle \mathbf{A} \xi \cdot \zeta \rangle = -\langle \xi \cdot \mathbf{A} \zeta \rangle$. We emphasize that the operator \mathbf{A} depends only on the fluid velocity field via Eq. (28). By Eq. (D8), the operator \mathbf{A} is bounded on \mathcal{H} with $\|\mathbf{A}\| \leq \|\mathsf{H}\| < \infty$. This, the skew-symmetry of \mathbf{A} , and the sesquilinearity of the \mathcal{H} -inner-product imply that $\mathbf{M} = -i\mathbf{A}$, where $i = \sqrt{-1}$, is a bounded symmetric operator, hence self-adjoint on \mathcal{H} with $\|\mathbf{M}\| = \|\mathbf{A}\| < \infty$. The spectrum Σ of the self-adjoint operator \mathbf{M} is real-valued with the spectral radius equal to its operator norm,⁵³ thus

$$\Sigma \subseteq [-\|\mathsf{H}\|, \|\mathsf{H}\|]. \quad (D11)$$

927 We are now ready to present the main results of this section. We start with the following corollary of Theorem 1.

928 Corollary 4. Let $\mathbf{Q}(\lambda)$ denote the resolution of the identity corresponding to the self-adjoint operator \mathbf{M} . Then, the components \mathfrak{S}_{jk}^* and \mathfrak{A}_{jk}^* , $j, k = 1, \dots, d$, of the symmetric \mathfrak{S}^* and antisymmetric \mathfrak{A}^* parts of the effective diffusivity matrix \mathfrak{D}^* have the Stieltjes-Radon integral representations in (19) with μ_{jk} replaced by the spectral measure $\tilde{\mu}_{jk}$ of \mathbf{M} in the $(\mathbf{g}_j, \mathbf{g}_k)$ state. The bounds in Theorem 2 hold for these integral representations for \mathfrak{S}_{jk}^* and \mathfrak{A}_{jk}^* . The mass $\tilde{\mu}_{jk}^0$ of the measure $\tilde{\mu}_{jk}$ is real-valued and satisfies

$$932 \quad \tilde{\mu}_{jk}^0 = \langle \mathsf{H}^T \Gamma \mathsf{H} \mathbf{e}_j \cdot \mathbf{e}_k \rangle, \quad |\tilde{\mu}_{jk}^0| \leq \|\mathsf{H}\|^2 < \infty. \quad (D12)$$

933 Proof of Corollary 4. Exactly as in the Proof of Theorem 1, Eq. (D10) and a direct analog of Eq. (17) lead to the Stieltjes integral representations in (19), involving a Stieltjes measure $\tilde{\mu}_{jk}$ associated with the function of the spectral variable λ defined by $\tilde{\mu}_{jk}(\lambda) = \langle \mathbf{Q}(\lambda) \mathbf{g}_j, \mathbf{g}_k \rangle$. Here, $\mathbf{g}_k = -\Gamma \mathsf{H} \mathbf{e}_k$ is defined in (D9) and $\{\mathbf{Q}(\lambda)\}_{\lambda \in \Sigma}$ is the family of self-adjoint projection operators that is in one-to-one correspondence with the bounded linear self-adjoint operator \mathbf{M} on the Hilbert space \mathcal{H}_x .^{53,58} From Eq. (18) and the fact that Γ is a self-adjoint projection operator on \mathcal{H}_x , the mass $\tilde{\mu}_{jk}^0$ of the measure $\tilde{\mu}_{jk}$ is real-valued and satisfies

$$938 \quad \tilde{\mu}_{jk}^0 = \langle \mathbf{g}_j, \mathbf{g}_k \rangle = \langle \Gamma \mathsf{H} \mathbf{e}_j \cdot \Gamma \mathsf{H} \mathbf{e}_k \rangle = \langle \mathsf{H}^T \Gamma \mathsf{H} \mathbf{e}_j \cdot \mathbf{e}_k \rangle, \quad |\tilde{\mu}_{jk}^0| \leq \|\mathsf{H}\|^2 < \infty. \quad (D13)$$

939 By analogy, the bounds in Theorem 2 also hold for these integral representations for \mathfrak{S}_{jk}^* and \mathfrak{A}_{jk}^* . This concludes our Proof of Corollary 4. \square

941 It is worth making the following observation. In the current setting, the formulas for \mathfrak{S}_{jk}^* and \mathfrak{A}_{jk}^* in (19) are computed with respect to 942 the standard basis $\{\mathbf{e}_k\}$, through the definition of $\tilde{\mu}_{jk}(\lambda) = \langle \mathbf{Q}(\lambda) \mathbf{g}_j, \mathbf{g}_k \rangle$ with $\mathbf{g}_k = -\Gamma \mathsf{H} \mathbf{e}_k$. We now show that, given \mathfrak{S}_{jk}^* and \mathfrak{A}_{jk}^* , $j, k = 1, \dots, d$, 943 the effective diffusivity matrix can be computed relative to any directions. This is due to the bilinearity of the inner-product underlying the 944 definition of $\tilde{\mu}_{jk}(\lambda)$. More specifically, if $\xi, \zeta \in \mathbb{R}^d$ are arbitrary directions of interest, then $\langle \mathbf{Q}(\lambda) \Gamma \mathsf{H} \xi, \Gamma \mathsf{H} \zeta \rangle = \sum_{jk} a_j b_k \langle \mathbf{Q}(\lambda) \mathbf{g}_j, \mathbf{g}_k \rangle$, where the 945 constants a_j and b_k , $j, k = 1, \dots, d$, are the coordinates of the vectors ξ and ζ with respect to the standard basis. This immediately leads to 946 integral representations for the effective diffusivity matrix relative to any desired directions. This observation had useful consequences in 947 Refs. 17 and 18.

948 **Theorem 5.** The spectral measure μ_{jk} in Theorem 1 is identical to the spectral measure $\tilde{\mu}_{jk}$ in Corollary 4,

$$\mu_{jk} \equiv \tilde{\mu}_{jk}. \quad (D14)$$

949 Before we prove Theorem 5, we give a brief outline of the proof and display the key formulas that lead to the result in (D14). The vector 950 field $\mathbf{g}_k = -\Gamma \mathsf{H} \mathbf{e}_k$ defined in Eq. (D9) and the scalar field $g_k = (-\Delta)^{-1} u_k$ defined in (12) are (weakly) related by⁴⁴

$$951 \quad \mathbf{g}_k = \nabla g_k. \quad (D15)$$

952 The operator $\mathbf{A} = \Gamma \mathsf{H} \Gamma$ defined in Eq. (D9) and the operator $A = \Delta^{-1} [\mathbf{u} \cdot \nabla]$ defined in (12), hence $\mathbf{M} = -i\mathbf{A}$ and $M = -iA$, are (weakly) 953 related by

$$953 \quad \mathbf{A} \nabla = \nabla A, \quad \mathbf{M} \nabla = \nabla M. \quad (D16)$$

954 Consequently, the masses and moments of the spectral measure μ_{jk} , $j, k = 1, \dots, d$, in Theorem 1 and the spectral measure $\tilde{\mu}_{jk}$ in Corollary 4 955 are identical,

$$956 \quad \mu_{jk}^n = \tilde{\mu}_{jk}^n, \quad n = 0, 1, 2, \dots. \quad (D17)$$

957 Since the self-adjoint operators \mathbf{M} and M are bounded, hence the spectra of these operators are bounded subsets of \mathbb{R} and the Hausdorff 958 moment problem is determinate,^{1,58} and this establishes Eq. (D14).

959 *Proof of Theorem 5.* In Ref. 44, Eqs. (D15) and (D16) were established in a more general context than our considerations here, where
 960 $\mathbf{u} = \mathbf{u}(\mathbf{x}, t)$ is periodic in both space and time t . We will see that the proof of Eq. (D17) essentially depends only on Eqs. (D15) and (D16).
 961 Consequently, en route, we will also establish that Eq. (D17) holds for this more general, time-dependent context. Here, we will only sketch the
 962 key ideas that were developed at length in Ref. 44. Equation (28), $\mathbf{u} = \nabla \cdot \mathbf{H}$, and the definitions $\Gamma = \nabla(\Delta^{-1})\nabla$, $\mathbf{g}_k = -\Gamma \mathbf{H} \mathbf{e}_k$, and $g_k = (-\Delta)^{-1} u_k$,
 963 together yield⁴⁴ Eq. (D15),

$$964 \quad \mathbf{g}_j = -\Gamma \mathbf{H} \mathbf{e}_j = \nabla(-\Delta)^{-1} u_j = \nabla g_j. \quad (\text{D18})$$

965 Consequently, by Eq. (18), the masses μ_{jk}^0 and $\tilde{\mu}_{jk}^0$ of the spectral measures μ_{jk} and $\tilde{\mu}_{jk}$ are equal,

$$966 \quad \tilde{\mu}_{jk}^0 = \langle \mathbf{g}_j \cdot \mathbf{g}_k \rangle = \langle \nabla g_j \cdot \nabla g_k \rangle = \langle g_j, g_k \rangle_{1,2} = \mu_{jk}^0. \quad (\text{D19})$$

967 Since $\Gamma \nabla \xi = \nabla \xi$ (weakly),⁴⁴ Eqs. (28) and (29), $\nabla \cdot [\mathbf{H} \nabla] = [\nabla \cdot \mathbf{H}] \cdot \nabla$, imply that for all $\xi \in \mathcal{H}^{1,2}$,

$$968 \quad \mathbf{A} \nabla \xi = \Gamma \mathbf{H} \Gamma \nabla \xi = \Gamma \mathbf{H} \nabla \xi = \nabla [(\Delta^{-1}) \mathbf{u} \cdot \nabla] \xi = \nabla \mathbf{A} \xi, \quad (\text{D20})$$

969 in a weak sense,⁴⁴ which establishes Eq. (D16). It follows from (D15) and (D16) that

$$970 \quad \begin{aligned} \tilde{\mu}_{jk}^1 &= \langle \mathbf{M} \mathbf{g}_j \cdot \mathbf{g}_k \rangle = \langle \mathbf{M} \nabla g_j \cdot \nabla g_k \rangle = \langle \nabla M g_j \cdot \nabla g_k \rangle = \langle M g_j, g_k \rangle_{1,2} = \mu_{jk}^1, \\ 971 \quad \tilde{\mu}_{jk}^2 &= \langle \mathbf{M}^2 \mathbf{g}_j \cdot \mathbf{g}_k \rangle = \langle \mathbf{M} \nabla M g_j \cdot \nabla g_k \rangle = \langle \nabla M^2 g_j \cdot \nabla g_k \rangle = \langle M^2 g_j, g_k \rangle_{1,2} = \mu_{jk}^2. \end{aligned} \quad (\text{D21})$$

972 An inductive argument establishes Eq. (D17). This concludes our Proof of Theorem 5. \square

973 We conclude this section with the following corollary of Theorem 5.

974 *Corollary 6.* For each $\xi \in \mathcal{H}^{1,2}$, we have $\nabla \xi \in \mathcal{H}_x$, and conversely, for each $\xi \in \mathcal{H}_x$, there exists unique $\xi \in \mathcal{H}^{1,2}$ such that $\xi = \nabla \xi$.
 975 Consequently, by Theorem 5, for every $\xi, \zeta \in \mathcal{H}^{1,2}$ and $\xi, \zeta \in \mathcal{H}_x$ related by $\xi = \nabla \xi$ and $\zeta = \nabla \zeta$, we have

$$976 \quad \mu_{\xi\xi}^n = \tilde{\mu}_{\xi\xi}^n, \quad n = 0, 1, 2, \dots. \quad (\text{D22})$$

977 This establishes that the spectral measures $\mu_{\xi\xi}$ and $\tilde{\mu}_{\xi\xi}$ are identical,

$$978 \quad \mu_{\xi\xi} \equiv \tilde{\mu}_{\xi\xi}. \quad (\text{D23})$$

979 Moreover, Eq. (D22) also holds for the class of space-time periodic fluid velocity fields $\mathbf{u} = \mathbf{u}(\mathbf{x}, t)$ described in Ref. 44.

980 *Proof of Corollary 6.* The Hilbert spaces $\mathcal{H}^{1,2}$ and \mathcal{H}_x are in one-to-one isometric correspondence.⁴⁴ More specifically, for every
 981 $\xi \in \mathcal{H}^{1,2}$, we have $\nabla \xi \in \mathcal{H}_x$ satisfying $\|\xi\|_{1,2} = \|\nabla \xi\|$ and $\|\mathbf{A} \xi\|_{1,2} = \|\mathbf{A} \nabla \xi\|$. Conversely, for each $\xi \in \mathcal{H}_x$, there exists unique⁴⁴
 982 $\xi \in \mathcal{H}^{1,2}$ (up to equivalence class) such that $\xi = \nabla \xi$, $\|\xi\| = \|\nabla \xi\|_{1,2}$, and $\|\mathbf{A} \xi\| = \|\mathbf{A} \nabla \xi\|_{1,2}$. By this and Theorem 5, we have Eqs. (D22)
 983 and (D23).

983 The proof of Eq. (D17) depends only on Eqs. (D15) and (D16), which also hold⁴⁴ for the class of space-time periodic fluid velocity
 984 fields $\mathbf{u} = \mathbf{u}(\mathbf{x}, t)$ described in Ref. 44. The argument in the previous paragraph above also holds for this time-dependent setting.⁴⁴ Therefore,
 985 Eq. (D22) holds for the time-dependent setting as well. This concludes our Proof of Corollary 6. \square

986 In order to establish Eq. (D23) for the time-dependent setting associated with operators having unbounded spectra,⁴⁴ one must first
 987 establish Carleman's criterion,¹ for example, associated with the Stieltjes or Hamburger moment problems. This requires an involved analysis
 988 that is outside of the scope of the current work. Our results in this direction will be published elsewhere.

989 APPENDIX E: DISCRETE SETTING: HILBERT SPACE OF CURL-FREE FIELDS

990 Here, we provide a matrix formulation for the effective parameter problem discussed in Appendix D 2, which provides discrete versions
 991 of the Stieltjes integral representations for \mathcal{D}^* shown in Eq. (19). These integrals involve a discrete spectral measure μ_{jk} analogous to the
 992 discrete measure in Eq. (35). More specifically, we use a discretized version of the cell problem in Eqs. (D2) and (D9), written as $(\varepsilon I + \mathbf{A}) \nabla \chi_k$
 993 $= \mathbf{g}_k$, to express the discrete spectral measure μ_{jk} explicitly in terms of the eigenvalues and eigenvectors of a matrix representation \mathbf{A} of the
 994 operator $\mathbf{A} = \Gamma \mathbf{H} \Gamma$. We then develop a *projection method* which additionally shows that the discrete measure μ_{jk} is actually determined by the
 995 eigenvalues and eigenvectors of a matrix that is much smaller than the matrix \mathbf{A} . This projection method is used in Appendix G to establish the
 996 equivalence of the two discrete approaches given in this appendix and Sec. IV, for the setting where the matrix gradient ∇ is rank-deficient.
 997 This equivalence proof establishes, en route, that the common discrete spectral measure can be computed by a method that combines the
 998 computational benefits of both approaches.

999 From the discussion in Sec. IV, the discrete representation of the projection operator $\Gamma = \nabla(\Delta^{-1})\nabla$ is given by the symmetric projection
 1000 matrix $\Gamma = \nabla(\nabla^T \nabla)^{-1} \nabla^T$ satisfying $\Gamma^2 = \Gamma$ and $\Gamma \nabla = \nabla$, where $(\nabla^T \nabla)^{-1}$ is now interpreted as a matrix inversion. We assume here that the

matrix ∇ is of full-rank so that $(\nabla^T \nabla)^{-1}$ exists. The rank-deficient case, where the matrix $\nabla^T \nabla$ is singular, is examined in Appendix G. In this way, the integrodifferential operator $\mathbf{A} = \Gamma \mathbf{H} \Gamma$ is represented by an antisymmetric matrix $\mathbf{A} = \Gamma \mathbf{H} \Gamma$ satisfying $\mathbf{A}^T = -\mathbf{A}$. In a similar way, the vectors $\mathbf{g}_k = -\Gamma \mathbf{H} \mathbf{e}_k$, $k = 1, \dots, d$, are redefined for this matrix setting. For simplicity, we will not make a notational distinction between the continuum and discrete cases for the vectors \mathbf{g}_k and \mathbf{e}_k as well as the matrix \mathbf{H} , as the context will be clear.

The spectrum of the antisymmetric matrix \mathbf{A} of size N , say, is composed of eigenvalues v_n , $n = 1, \dots, N$, with the corresponding eigenvectors \mathbf{w}_n satisfying $\mathbf{A} \mathbf{w}_n = v_n \mathbf{w}_n$. Since \mathbf{A} is skew-symmetric, the eigenvalues v_n are purely imaginary,²⁵ $v_n = i\lambda_n$ with $\lambda_n \in \mathbb{R}$. Therefore, the matrix $\mathbf{M} = -i\mathbf{A}$ is Hermitian ($\mathbf{M}^\dagger = \mathbf{M}$) and it has the same eigenvectors \mathbf{w}_n as the matrix \mathbf{A} and real eigenvalues given by $\lambda_n = \text{Im } v_n$. The eigenvectors \mathbf{w}_n , $n = 1, \dots, N$, of the Hermitian matrix \mathbf{M} form an orthonormal basis for \mathbb{C}^N ,^{25,28} i.e., $\mathbf{w}_n^\dagger \mathbf{w}_m = \delta_{nm}$ and for every $\xi \in \mathbb{C}^N$ we have $\xi = \sum_n (\mathbf{w}_n^\dagger \xi) \mathbf{w}_n = (\sum_n \mathbf{w}_n \mathbf{w}_n^\dagger) \xi$. Consequently, defining $\mathcal{Q}_n = \mathbf{w}_n \mathbf{w}_n^\dagger$, $n = 1, \dots, N$, to be the mutually orthogonal Hermitian projection matrices onto the eigenspaces spanned by the \mathbf{w}_n , we have the following analog of Eq. (34):

$$\sum_{n=1}^N \mathcal{Q}_n = I, \quad \mathcal{Q}_n = \mathbf{w}_n \mathbf{w}_n^\dagger, \quad \mathcal{Q}_l \mathcal{Q}_m = \mathcal{Q}_l \delta_{lm}. \quad (\text{E1})$$

With an argument similar to the one in the paragraph following Eq. (34), one can show that for all $\xi, \zeta \in \mathbb{C}^N$ and complex-valued polynomials $f(\lambda)$ and $h(\lambda)$, the bilinear functional $\langle f(\mathbf{M})\xi \cdot h(\mathbf{M})\zeta \rangle$ has the integral representation in Eq. (17), with M substituted by \mathbf{M} and the scalars ξ and ζ replaced by vectors ξ and ζ . Moreover, the complex-valued function $\mu_{\xi\zeta}(\lambda) = \langle \mathcal{Q}(\lambda)\xi, \zeta \rangle$ in Eq. (17) is now given by $\mu_{\xi\zeta}(\lambda) = \langle \mathcal{Q}(\lambda)\xi \cdot \zeta \rangle$, where the associated matrix representation $\mathcal{Q}(\lambda)$ of the projection operator $\mathcal{Q}(\lambda)$ and the discrete spectral measure $d\mu_{\xi\zeta}(\lambda)$ are given by the following analog of Eq. (35):

$$\mathcal{Q}(\lambda) = \sum_{n: \lambda_n \leq \lambda} \theta(\lambda - \lambda_n) \mathcal{Q}_n, \quad d\mu_{\xi\zeta}(\lambda) = \sum_{n: \lambda_n \leq \lambda} \langle \delta_{\lambda_n}(d\lambda) [\mathcal{Q}_n \xi \cdot \zeta] \rangle. \quad (\text{E2})$$

We are now ready to present the main results of this section, given in the following corollary of Theorem 3.

Corollary 7. Consider the standard eigenvalue problem $\mathbf{M}\mathbf{w}_n = \lambda_n \mathbf{w}_n$ associated with the Hermitian matrix $\mathbf{M} = -i\mathbf{A}$. Let \mathbf{W} be the matrix with columns consisting of the eigenvectors \mathbf{w}_n and Λ be the diagonal matrix with eigenvalues λ_n on its diagonal. The discrete, matrix representations of the bilinear functional formulas for \mathfrak{S}_{jk}^* and \mathfrak{A}_{jk}^* in Eq. (D4) with H replaced by \mathbf{A} , as discussed right before Eq. (D10), are given by

$$\mathfrak{S}_{jk}^* = \varepsilon(\delta_{jk} + \langle \nabla \chi_j \cdot \nabla \chi_k \rangle), \quad \mathfrak{A}_{jk}^* = \langle \mathbf{A} \nabla \chi_j \cdot \nabla \chi_k \rangle, \quad (\text{E3})$$

which is analogous to Eq. (36). Also, the discrete representation of the resolvent formula for $\nabla \chi_j$ in Eq. (D9) is given by

$$\nabla \chi_j = \mathbf{W}(\varepsilon I + i\Lambda)^{-1} \mathbf{W}^\dagger \mathbf{g}_j, \quad \mathbf{g}_j = -\Gamma \mathbf{H} \mathbf{e}_j, \quad (\text{E4})$$

which is analogous to Eq. (37). The discrete representations of the bilinear functional formulas for \mathfrak{S}_{jk}^* and \mathfrak{A}_{jk}^* in (D10) are given by

$$\begin{aligned} \mathfrak{S}_{jk}^* &= \varepsilon(\delta_{jk} + \langle (\varepsilon I + i\Lambda)^{-1} \mathbf{W}^\dagger \mathbf{g}_j \cdot (\varepsilon I + i\Lambda)^{-1} \mathbf{W}^\dagger \mathbf{g}_k \rangle), \\ \mathfrak{A}_{jk}^* &= \langle i\Lambda(\varepsilon I + i\Lambda)^{-1} \mathbf{W}^\dagger \mathbf{g}_j \cdot (\varepsilon I + i\Lambda)^{-1} \mathbf{W}^\dagger \mathbf{g}_k \rangle, \end{aligned} \quad (\text{E5})$$

which are analogous to those in Eq. (38). Consequently, the formulas for \mathfrak{S}_{jk}^* and \mathfrak{A}_{jk}^* in (E5) have the following series representations:

$$\mathfrak{S}_{jk}^*/\varepsilon - \delta_{jk} = \sum_{n=1}^N \frac{\text{Re} [\overline{(\mathbf{w}_n^\dagger \mathbf{g}_j)} (\mathbf{w}_n^\dagger \mathbf{g}_k)]}{\varepsilon^2 + \lambda_n^2}, \quad \mathfrak{A}_{jk}^* = \sum_{n=1}^N \frac{\lambda_n \text{Im} [\overline{(\mathbf{w}_n^\dagger \mathbf{g}_j)} (\mathbf{w}_n^\dagger \mathbf{g}_k)]}{\varepsilon^2 + \lambda_n^2}, \quad (\text{E6})$$

which is analogous to Eq. (39). Finally, recalling the projection matrix $\mathcal{Q}_n = \mathbf{w}_n \mathbf{w}_n^\dagger$ in (E1), we have

$$\overline{(\mathbf{w}_n^\dagger \mathbf{g}_j)} (\mathbf{w}_n^\dagger \mathbf{g}_k) = \mathcal{Q}_n \mathbf{g}_j \cdot \mathbf{g}_k, \quad (\text{E7})$$

which is analogous to Eq. (40). It follows from Eq. (E7) that the series representations for \mathfrak{S}_{jk}^* and \mathfrak{A}_{jk}^* in (E6) have the Stieltjes integral representations in Eq. (19), involving the discrete spectral measure μ_{jk} in (E2) with $\xi = \mathbf{g}_j = -\Gamma \mathbf{H} \mathbf{e}_j$ and $\zeta = \mathbf{g}_k = -\Gamma \mathbf{H} \mathbf{e}_k$.

Proof of Corollary 7. Equation (E3) follows from the discrete version of (D4) and $\Gamma \nabla = \nabla$ so $\langle \mathbf{H} \nabla \chi_j \cdot \nabla \chi_k \rangle = \langle \mathbf{A} \nabla \chi_j \cdot \nabla \chi_k \rangle$. Consider the spectral decomposition $\mathbf{M} = \mathbf{W} \Lambda \mathbf{W}^\dagger$ of the Hermitian matrix $\mathbf{M} = -i\mathbf{A}$ involving the real eigenvalues λ_n comprising the main diagonal of the diagonal matrix Λ and the eigenvectors \mathbf{w}_n comprising the columns of the unitary matrix \mathbf{W} satisfying $\mathbf{W}^\dagger \mathbf{W} = \mathbf{W} \mathbf{W}^\dagger = I$.²⁵ Equation (E4) follows from this spectral decomposition of $\mathbf{A} = i\mathbf{M}$, the discrete version of the resolvent formula in Eq. (D9) written as $\nabla \chi_j = (\varepsilon I + \mathbf{A})^{-1} \mathbf{g}_j$, the fact that \mathbf{W} is unitary satisfying $\mathbf{W}^\dagger = \mathbf{W}^{-1}$, and the elementary properties of matrix inversion.²⁵ Substituting the resolvent formula for

1040 $\nabla \chi_j$ in (E4) into Eq. (E3) and using $W^\dagger = W^{-1}$ yield Eq. (E5). The quadratic form $W^\dagger g_j \cdot W^\dagger g_k$ arising in (E5) can be written in terms of the
 1041 projection matrices $Q_n = w_n w_n^\dagger$ defined in (E1) as follows:

$$1042 \quad W^\dagger g_j \cdot W^\dagger g_k = \sum_{n=1}^N \overline{(w_n^\dagger g_j)(w_n^\dagger g_k)} = \sum_{n=1}^N Q_n g_j \cdot g_k. \quad (\text{E8})$$

1043 Exactly as in Theorem 3, we have Eq. (E6), which can be written in terms of the integral representations in Eq. (19) involving the discrete
 1044 spectral measure $d\mu_{jk}(\lambda)$ in Eq. (E2) with $\xi = g_j = -\Gamma H e_j$ and $\zeta = g_k = -\Gamma H e_k$. This concludes our Proof of Corollary 7. \square

1045 We conclude this section with the development of a *projection method* that is used in the Proof of Theorem 10. This method shows
 1046 that the presence of the projection matrix Γ in the operator $\Gamma H \Gamma$ and $g_k = -\Gamma H e_k$ projects out contributions of the null space of Γ in the
 1047 series representation for \mathfrak{D}^* in (E6). This is reminiscent of problems encountered for many elliptic equations on periodic domains, where the
 1048 analysis requires a deficient dimension to be projected out.⁷ Theorem 10 establishes that the discrete framework developed in Sec. IV and this
 1049 section yield equivalent Stieltjes integral representations for the effective diffusivity matrix \mathfrak{D}^* , involving a discrete spectral measure, and also
 1050 generalizes this result to the setting where the matrix ∇ is rank-deficient. The Proof of Theorem 10 demonstrates that the common discrete
 1051 spectral measure can be computed by a method that combines the computational benefits of both approaches. This, in turn, is used in our
 1052 numerical computations of Stieltjes integral representations of \mathfrak{D}^* in Sec. V.

1053 **Theorem 8** (Projection method). *The real-symmetric projection matrix Γ of size N has eigenvalues satisfying $\gamma_n = 0, 1$, hence the spectral
 1054 decomposition*

$$1055 \quad \Gamma = PGP^T, \quad G = \text{diag}(\mathbf{0}_{N_0}, \mathbf{1}_{N_1}), \quad P = [P_0 \ P_1]. \quad (\text{E9})$$

1056 Here, $\mathbf{0}_{N_0}$ and $\mathbf{1}_{N_1}$ are vectors of zeros and ones with N_0 and N_1 components, respectively, where $N = N_0 + N_1$. Moreover, the columns comprising the $N \times N_0$ matrix P_0 and the $N \times N_1$ matrix P_1 are orthonormal eigenvectors that span the null space and range of Γ , respectively.
 1057 Consequently, the matrix Γ can be written as

$$1058 \quad \Gamma = P_1 P_1^T. \quad (\text{E10})$$

1059 Consider the spectral composition of the antisymmetric matrix $P_1^T H P_1$ of size N_1 ,

$$1060 \quad P_1^T H P_1 = i R_{11} \Lambda_{11} R_{11}^T, \quad (\text{E11})$$

1061 where R_{11} is a unitary matrix, $R_{11}^T R_{11} = R_{11} R_{11}^T = I_{N_1}$, Λ_{11} is a real-valued diagonal matrix, and I_{N_1} is the identity matrix of size $N_1 \times N_1$.
 1062 Consequently, the matrix $A = i \Gamma H \Gamma$ has the spectral decomposition

$$1063 \quad A = i W \Lambda W^\dagger, \quad W = [P_0 \ P_1 R_{11}], \quad \Lambda = \text{diag}(O_{00} \ \Lambda_{11}). \quad (\text{E12})$$

1064 Equations (E10) and (E12), and the mutual orthogonality of the matrices P_0 and P_1 yield

$$1065 \quad W^\dagger g_k = W^\dagger \Gamma H e_k = [O_0 \ P_1 R_{11}]^\dagger H e_k, \quad (\text{E13})$$

1066 where O_0 is a matrix of zeros of size $N \times N_0$. Consequently, Eq. (E8) can be written as

$$1067 \quad W^\dagger g_j \cdot W^\dagger g_k = (P_1 R_{11})^\dagger H e_k \cdot (P_1 R_{11})^\dagger H e_k. \quad (\text{E14})$$

1068 Moreover, the spectral weights in Eq. (E8) associated with $\gamma_n = 0$ are identically zero $[Q_n g_j \cdot g_k] = 0$.

1069 *Proof of Theorem 8.* Using the spectral decomposition $\Gamma = PGP^T$ in (E9), we write the matrix $A = \Gamma H \Gamma$ as $A = P[G(P^T H P)G]P^T =$
 1070 $P \text{diag}(O_{00} P_1^T H P_1) P^T$, where O_{00} is a matrix of zeros of size $N_0 \times N_0$. Due to the skew-symmetry of H , the $N_1 \times N_1$ matrix $P_1^T H P_1$ is also
 1071 skew-symmetric. Consequently, it has the spectral decomposition in Eq. (E11); hence, $A = P \text{diag}(O_{00} i R_{11} \Lambda_{11} R_{11}^T) P^T$. Writing this in block
 1072 matrix form⁴² and multiplying yield Eq. (E12). Equations (E10) and (E12), and the mutual orthogonality of the matrices P_0 and P_1 yield Eq.
 1073 (E13). This concludes our Proof of Theorem 8. \square

1074 APPENDIX F: DISCRETE EQUIVALENCE OF THE EFFECTIVE PARAMETER PROBLEMS

1075 In Sec. III, we provided Stieltjes integral representations for the symmetric \mathfrak{S}^* and antisymmetric \mathfrak{A}^* parts of the effective diffusivity
 1076 matrix \mathfrak{D}^* , associated with an incompressible fluid velocity field. A discrete version of this mathematical framework was formulated
 1077 in Sec. IV. An alternate approach to the effective parameter problem was formulated in Appendix D, and its discrete version was for-
 1078 mulated in Appendix E. In this section, we demonstrate that the discrete versions of these effective parameter problems yield equivalent
 1079 spectral representations of \mathfrak{D}^* when the matrix ∇ is of full-rank, as in the case of Dirichlet boundary conditions, so that the matrix Lapla-
 1080 cian is invertible. In Appendix G, this result is extended to the setting where ∇ is rank-deficient, as in the case of periodic boundary
 1081 conditions.

Let $\nabla = U\Sigma V^T$ be the singular value decomposition (SVD) of the matrix ∇ of size $N \times K$, where $K = L^d$ and $N = Kd$. Here, $\Sigma = \text{diag}(\sigma_1, \dots, \sigma_K)$, where $0 \leq \sigma_1 \leq \dots \leq \sigma_K$, and the matrices U and V are of size $N \times K$ and $K \times K$, respectively, and satisfy¹⁴

$$U^T U = I, \quad V^T V = VV^T = I, \quad (F1)$$

where I is the $K \times K$ identity matrix. The columns of U are called left singular vectors, the columns of V are called right singular vectors, and the σ_i are called singular values.

It follows from $\nabla = U\Sigma V^T$ and Eq. (F1) that the spectral decomposition of the negative matrix Laplacian $\nabla^T \nabla$ is given by $\nabla^T \nabla = V\Sigma^2 V^T$.¹⁴ We assume that ∇ is of full-rank so that $\sigma_i > 0$ for all $i = 1, \dots, K$. This implies that Σ^{-1} exists so that the matrix Laplacian is invertible. In this case, it follows from $\nabla = U\Sigma V^T$ and Eq. (F1) that the projection matrix $\Gamma = \nabla(\nabla^T \nabla)^{-1} \nabla^T$ is given by

$$\Gamma = UU^T, \quad (F2)$$

which is an $N \times N$ symmetric projection matrix satisfying $\Gamma^2 = \Gamma$ and $\Gamma \nabla = \nabla$. A key property of the SVD of the *full-rank* matrix ∇ is that its range is spanned by the columns of U ,¹⁴ hence, $\Gamma = UU^T$ projects subspaces of \mathbb{R}^N onto the range of ∇ .

From Eqs. (F1) and (F2), we can write the eigenvalue problem $-\imath\Gamma H\Gamma w_n = \lambda_n w_n$ discussed in Appendix E as

$$[-\imath U^T H U][U^T w_n] = \lambda_n [U^T w_n]. \quad (F3)$$

Now consider the generalized eigenvalue problem $-\imath\nabla^T H \nabla z_n = \alpha_n \nabla^T \nabla z_n$ discussed in Sec. IV and recall that $\nabla = U\Sigma V^T$ and $\nabla^T \nabla = V\Sigma^2 V^T$. Since Σ is invertible, by Eq. (F1), we can write this generalized eigenvalue problem as the following standard eigenvalue problem:

$$[-\imath U^T H U][\Sigma V^T z_n] = \alpha_n [\Sigma V^T z_n]. \quad (F4)$$

Comparing the formulas in Eqs. (F3) and (F4) indicates that spectrum associated with each of these eigenvalue problems is identical, $\alpha_n = \lambda_n$, and that the eigenvectors are related by $U^T w_n = \Sigma V^T z_n$. Since Γ is a projection matrix, $\Gamma^2 = \Gamma$, the eigenvalue problem $\Gamma H \Gamma w_n = \imath \lambda_n w_n$ can be written as $\Gamma H \Gamma [\Gamma w_n] = \imath \lambda_n [\Gamma w_n]$, which implies that $\Gamma w_n = w_n$. Consequently, applying the matrix U to both sides of the formula $U^T w_n = \Sigma V^T z_n$ and recalling that $\Gamma = UU^T$ and $\nabla = U\Sigma V^T$, we have

$$w_n = \nabla z_n. \quad (F5)$$

In the following lemma, we make precise the correspondence between the standard eigenvalue problem $-\imath\Gamma H\Gamma w_n = \lambda_n w_n$ and the generalized eigenvalue problem $-\imath\nabla^T H \nabla z_n = \alpha_n \nabla^T \nabla z_n$, as well as the associated spectral measures in Eqs. (E2) and (35), respectively.

Lemma 9. Consider the standard eigenvalue problem and the generalized eigenvalue problem given, respectively, in the following equations:

$$-\imath\Gamma H\Gamma w_n = \lambda_n w_n, \quad (F6)$$

$$-\imath\nabla^T H \nabla z_n = \lambda_n \nabla^T \nabla z_n. \quad (F7)$$

Let $\nabla = U\Sigma V^T$ be the SVD of the matrix ∇ , which we assume to be of full-rank. Then, Eq. (F6) implies and is implied by Eq. (F7), with w_n and z_n related as in Eq. (F5). This implies that the spectrum associated with each of these eigenvalue problems is identical. Moreover, the spectral weights in Eqs. (E8) and (40) are identical; specifically,

$$Q_n \Gamma H e_j \cdot \Gamma H e_k = \nabla Q_n [\nabla^T \nabla]^{-1} u_j \cdot \nabla [\nabla^T \nabla]^{-1} u_k. \quad (F8)$$

This, in turn, implies that the associated spectral measures in Eqs. (E2) and (35) are identical.

Proof of Lemma 9. Recall that $\nabla = U\Sigma V^T$, $\nabla^T \nabla = V\Sigma^2 V^T$, and $\Gamma = UU^T$, where Σ is invertible, and the matrices V and U satisfy Eq. (F1). First, consider Eq. (F6) written as in Eq. (F3), $[-\imath U^T H U][U^T w_n] = \lambda_n [U^T w_n]$. Since the matrix Σ is invertible and $V^T V = I$, we can rewrite Eq. (F3) as

$$V\Sigma [-\imath U^T H U](\Sigma V^T)(V\Sigma^{-1})[U^T w_n] = \lambda_n (V\Sigma^2 V^T)(V\Sigma^{-1})[U^T w_n], \quad (F9)$$

which is precisely Eq. (F7) written in terms of $\nabla = U\Sigma V^T$ with $z_n = V\Sigma^{-1} U^T w_n$. This formula for z_n [Eq. (F1)] and the formula $\Gamma w_n = w_n$ above Eq. (F5) imply that $w_n = U\Sigma V^T z_n = \nabla z_n$, which is the formula in (F5). Now consider Eq. (F7) written as in (F4), $[-\imath U^T H U][\Sigma V^T z_n] = \lambda_n [\Sigma V^T z_n]$. Since $U^T U = I$, we can rewrite Eq. (F4) as

1121

$$\mathbf{U}[-\imath \mathbf{U}^T \mathbf{H} \mathbf{U}] (\mathbf{U}^T \mathbf{U}) [\Sigma \nabla^T \mathbf{z}_n] = \lambda_n \mathbf{U}[\Sigma \nabla^T \mathbf{z}_n], \quad (\text{F10})$$

1122 which is precisely (F6) written in terms of $\Gamma = \mathbf{U} \mathbf{U}^T$ with $\mathbf{w}_n = \mathbf{U} \Sigma \nabla^T \mathbf{z}_n = \nabla \mathbf{z}_n$.

1123 We now establish Eq. (F8). From the formula $\mathbf{u} = \nabla \cdot \mathbf{H}$ in (28), for the continuum setting, we have that $u_j = (\nabla \cdot \mathbf{H}) \cdot \mathbf{e}_j = \nabla \cdot (\mathbf{H} \mathbf{e}_j)$.
 1124 Since $\nabla = \mathbf{U} \Sigma \nabla^T$, the discrete version of this formula is given by

$$\mathbf{u}_j = -\nabla^T \mathbf{H} \mathbf{e}_j = -\nabla \Sigma \mathbf{U}^T \mathbf{H} \mathbf{e}_j. \quad (\text{F11})$$

1125 From $\nabla = \mathbf{U} \Sigma \nabla^T$ and $(\nabla^T \nabla)^{-1} = \nabla \Sigma^{-2} \nabla^T$, we have $\nabla(\nabla^T \nabla)^{-1} = \mathbf{U} \Sigma^{-1} \nabla^T$. Consequently, $\Gamma = \mathbf{U} \mathbf{U}^T$, and Eqs. (F1) and (F11) yield
 1126 $\nabla(\nabla^T \nabla)^{-1} \mathbf{u}_j = -\Gamma \mathbf{H} \mathbf{e}_j$. Equation (F8) now follows from the formula $\mathbf{w}_n = \nabla \mathbf{z}_n$ in (F5),

$$\begin{aligned} \mathbf{w}_n \mathbf{w}_n^\dagger \nabla(\nabla^T \nabla)^{-1} \mathbf{u}_j \cdot \nabla(\nabla^T \nabla)^{-1} \mathbf{u}_k &= [(\nabla^T \nabla)^{-1} \nabla^T \mathbf{w}_n] [(\nabla^T \nabla)^{-1} \nabla^T \mathbf{w}_n]^\dagger \mathbf{u}_j \cdot \mathbf{u}_k \\ &= [(\nabla^T \nabla)^{-1} \nabla^T \nabla \mathbf{z}_n] [(\nabla^T \nabla)^{-1} \nabla^T \nabla \mathbf{z}_n]^\dagger \mathbf{u}_j \cdot \mathbf{u}_k \\ &= \mathbf{z}_n \mathbf{z}_n^\dagger \mathbf{u}_j \cdot \mathbf{u}_k, \end{aligned} \quad (\text{F12})$$

1127 where we have used that the inverse of a symmetric matrix is also symmetric.²⁵ The equivalence of Eqs. (F8) and (F12) now follows from Eqs. (E1), (34), and (40). This concludes our Proof of Lemma 9. \square

1128 We conclude this section with a discussion regarding numerical computations of the effective diffusivity matrix \mathfrak{D}^* . The approach discussed in this section and the projection method discussed in Theorem 8 demonstrate that a hybrid of these two approaches leads to the most efficient algorithm for numerical computations of spectral representations for \mathfrak{D}^* —combining the computational advantages of both the methods discussed in Appendix E and Sec. IV. More specifically, in the full rank setting, the spectral measure underlying the discrete integral representation for \mathfrak{D}^* was calculated in Appendix E in terms of the *standard* eigenvalue problem $-\imath \Gamma \mathbf{H} \mathbf{G} \mathbf{w}_m = \lambda_m \mathbf{w}_m$, where the matrix $-\imath \Gamma \mathbf{H} \mathbf{G}$ is of size $N \times N$. In Sec. IV, \mathfrak{D}^* was calculated in terms of the *generalized* eigenvalue problem $-\imath \nabla^T \mathbf{H} \nabla \mathbf{z}_n = \lambda_n \nabla^T \nabla \mathbf{z}_n$, involving the $K \times K$ matrices $-\imath \nabla^T \mathbf{H} \nabla$ and $\nabla^T \nabla$. Since $\nabla^T = (\nabla_1^T, \dots, \nabla_d^T)$ is of size $K \times N$, we have that $K = N/d < N$. However, the generalized eigenvalue problem is more computationally intensive than the standard eigenvalue problem.⁴⁷ For the case of randomly perturbed flows, many statistical iterations are necessary to compute \mathfrak{D}^* and the efficiency of the numerical algorithm is key. Neither of the methods discussed in Appendix E and Sec. IV are optimal.

1129 The projection method developed in Theorem 8 demonstrates that, by first computing the standard eigenvalue decomposition of the nonrandom matrix Γ , the spectral statistics of the eigenvalue problem $-\imath \Gamma \mathbf{H} \mathbf{G} \mathbf{w}_m = \lambda_m \mathbf{w}_m$ can then be obtained by repeatedly computing the standard eigenvalue decomposition of smaller matrices. They are of size $K \times K$ by Eqs. (E10)–(E12) and (F2)f. We emphasize that in the setting of full-rank ∇ , the parameter K in this section and N_1 in Theorem 8 both denote the rank of the matrix Γ , i.e., $K = N_1$. Note, computing the matrix $\Gamma = \nabla(\nabla^T \nabla)^{-1} \nabla^T$ itself involves the cost of numerically solving N linear systems of size $K \times K$. Alternatively, the Proof of Lemma 9 illustrates that by first computing the SVD of the matrix gradient, $\nabla = \mathbf{U} \Sigma \nabla^T$, the spectral statistics of the generalized eigenvalue problem $-\imath \nabla^T \mathbf{H} \nabla \mathbf{z}_n = \lambda_n \nabla^T \nabla \mathbf{z}_n$ can then be obtained by repeatedly computing the *standard* eigenvalue decomposition of the matrix $-\imath \mathbf{U}^T \mathbf{H} \mathbf{U}$ which is of size $K \times K$. When N is large, these equivalent methods are more numerically efficient than the other approaches discussed in Appendix E and Sec. IV.

1130 In Appendix G, we generalize Lemma 9 to the case where ∇ is rank-deficient with rank K_1 satisfying $K_1 < K$. Our analysis demonstrates that the two formulations discussed in Appendix E and Sec. IV yield equivalent spectral representations of the effective diffusivity matrix \mathfrak{D}^* in this rank-deficient setting. Moreover, en route, a more efficient numerical algorithm for computations of \mathfrak{D}^* is revealed. More specifically, we demonstrate that by first computing the SVD of the matrix gradient, \mathfrak{D}^* can be computed via a *standard* eigenvalue problem for matrices of size $K_1 \times K_1$. Consequently, the rank deficiency of the problem actually increases the numerical efficiency of computations.

APPENDIX C: RANK DEFICIENCY AND A UNIFYING STANDARD EIGENVALUE PROBLEM

1131 In Sec. IV and Appendix E, we provided two discrete, matrix formulations of the effective parameter problem for advection enhanced diffusion, which led to discrete Stieltjes integral representations for the effective diffusivity matrix \mathfrak{D}^* involving spectral measures of Hermitian matrices. These two formulations assume that the $N \times K$ matrix ∇ is of full-rank K so that the negative matrix Laplacian $\nabla^T \nabla$ is invertible. Lemma 9 of Appendix F shows that, given this condition, the two formulations yield equivalent spectral representations of \mathfrak{D}^* . This analysis also demonstrates that a hybrid of the two formulations leads to a numerical algorithm for computing \mathfrak{D}^* that is more efficient than the numerical algorithms for either approach. In this section, we generalize Lemma 9 to the case where ∇ is rank-deficient, with rank K_1 satisfying $K_1 < K$. We demonstrate that the two formulations are equivalent in this rank-deficient setting and we also derive an efficient hybrid numerical algorithm for computations of \mathfrak{D}^* . This framework is used in Sec. V to compute \mathfrak{D}^* for periodic flows, for which the matrix ∇ with periodic boundary conditions is rank-deficient.

1166 Toward this goal, let $\nabla = U\Sigma V^T$ be the SVD of the matrix gradient ∇ of size $N \times K$, introduced in Sec. IV and Appendix F. We assume
 1167 that ∇ is rank deficient so that $\nabla^T \nabla = V\Sigma^2 V^T$ is singular, with K_1 nonzero eigenvalues and $K_0 = K - K_1$ zero eigenvalues, and write

$$1168 \quad U = [U_0 \ U_1], \quad \Sigma = \text{diag}(O_{00}, \Sigma_1), \quad V = [V_0 \ V_1]. \quad (\text{G1})$$

1169 Here, we denote O_{ab} , $a, b = 0, 1$, to be matrices of zeros of size $K_a \times K_b$, U_a is of size $N \times K_a$, V_a is $K \times K_a$, and Σ_1 is a $K_1 \times K_1$ diagonal,
 1170 invertible matrix. By Eq. (F1), the matrices U_1 and V_1 satisfy $U_1^T U_1 = I_1$ and $V_1^T V_1 = I_1$, where I_1 is the $K_1 \times K_1$ identity matrix, but $V_1 V_1^T \neq I$.
 1171 Due to the blocks of zeros in the matrix Σ in Eq. (G1), we can write the matrix gradient as $\nabla = U_1 \Sigma_1 V_1^T$ and the negative matrix Laplacian
 1172 as $\nabla^T \nabla = V_1 \Sigma_1^2 V_1^T$. An important property of the SVD of the matrix ∇ is that its null space is spanned by the columns of V_0 and its range
 1173 is spanned by the columns of U_1 .¹⁴ We emphasize that in the setting where ∇ is full-rank, we have $U_1 = U$, $\Sigma_1 = \Sigma$, and $V_1 = V$ satisfying
 1174 $V_1 V_1^T = V_1^T V_1 = I_1$.

1175 Consider the cell problem in Eq. (4) written, via (28) and $[\nabla \cdot H] \cdot \nabla \varphi = \nabla \cdot [H \nabla \varphi]$, as $\nabla \cdot H \nabla \chi_j + \varepsilon \Delta \chi_j = -u_j$. Discretizing this formula
 1176 yields (see the discussion following Eq. (29) for details regarding the discretization of these differential operators, etc.)

$$1177 \quad \nabla^T H \nabla \chi_j + \varepsilon \nabla^T \nabla \chi_j = u_j, \quad (\text{G2})$$

1178 where u_j is the discrete, vector representation of the j th component of the fluid velocity field u_j and similarly for χ_j . Substituting the formula
 1179 for u_j in (G2) into the discrete version $\mathfrak{D}_{jk}^* = \varepsilon \delta_{jk} + \langle u_j \cdot \chi_k \rangle$ of Eq. (3) yields

$$1180 \quad \mathfrak{D}_{jk}^* = \mathfrak{S}_{jk}^* + \mathfrak{A}_{jk}^*, \quad \mathfrak{S}_{jk}^* = \varepsilon(\delta_{jk} + \langle \nabla \chi_j \cdot \nabla \chi_k \rangle), \quad \mathfrak{A}_{jk}^* = \langle \nabla^T H \nabla \chi_j \cdot \chi_k \rangle, \quad (\text{G3})$$

1181 where, as before, $\mathfrak{S}_{kj}^* = \mathfrak{S}_{jk}^*$ and $\mathfrak{A}_{kj}^* = -\mathfrak{A}_{jk}^*$. We are now ready to state the key result of this appendix.

1182 **Theorem 10.** Let the matrix gradient ∇ be rank-deficient and let $\nabla = U_1 \Sigma_1 V_1^T$ be its SVD. Also, let $U_1^T H U_1 = i R_1 \Lambda_1 R_1^\dagger$ be the spectral
 1183 decomposition of the antisymmetric matrix $U_1^T H U_1$. Consider the discrete formulation of the effective parameter problem developed in Sec. IV.
 1184 We have the following generalization of Eq. (34):

$$1185 \quad \sum_{n=1}^{K_1} Q_n^1 = V_1 V_1^T, \quad Q_n^1 = z_n^1 [\nabla z_n^1]^\dagger \nabla, \quad Q_l^1 Q_m^1 = Q_l^1 \delta_{lm}, \quad (\text{G4})$$

1186 where the matrices Q_n^1 , $n = 1, \dots, K_1$, are self-adjoint with respect to the discrete inner-product $\langle \cdot, \cdot \rangle_{1,2}$ defined by $\langle \xi, \zeta \rangle_{1,2} = \langle \nabla \xi \cdot \nabla \zeta \rangle$, i.e.,
 1187 $\langle Q_n^1 \xi, \zeta \rangle_{1,2} = \langle \xi, Q_n^1 \zeta \rangle_{1,2}$ for $\xi, \zeta \in \mathbb{C}^{K_1}$. Moreover, the generalization of the resolvent formula $\chi_j = Z(\varepsilon l + i \Lambda)^{-1} Z^\dagger u_j$ in Eq. (37) is given by

$$1188 \quad V_1^T \chi_j = V_1^T Z_1 (\varepsilon l_1 + i \Lambda_1)^{-1} Z_1^\dagger u_j, \quad Z_1 = V_1 \Sigma_1^{-1} R_1. \quad (\text{G5})$$

1189 Now consider the discrete formulation of the effective parameter problem developed in Appendix E. Let $\Gamma_1 H \Gamma_1 = i W_1 \tilde{\Lambda} W_1^\dagger$ be the spectral
 1190 decomposition of the antisymmetric matrix $\Gamma_1 H \Gamma_1$, where $\Gamma_1 = U_1 U_1^T$, $\tilde{\Lambda}$ is a diagonal real-valued matrix with $\tilde{\lambda}_n^1$, $n = 1, \dots, N$, on its diagonal,
 1191 and W_1 is a unitary matrix with columns w_n^1 . Then, Eqs. (E1) and (E2) hold with Q_n and λ_n replaced by $Q_n^1 = [w_n^1][w_n^1]^\dagger$ and $\tilde{\lambda}_n^1$. Also, the
 1192 resolvent formula in Eq. (E4) holds with W replaced by W_1 and Λ replaced by $\tilde{\Lambda}$.

1193 These two discrete formulations of the effective parameter problem are related as follows: The diagonal eigenvalue matrices $\tilde{\Lambda}$ and Λ_1 are
 1194 related by $\tilde{\Lambda} = \text{diag}(O_{00}, \Lambda_1)$. The eigenvector matrices W_1 and Z_1 are related by the following generalization of Eq. (F5) [also see (E12)]:

$$1195 \quad W_1 = [P_0 \ \nabla Z_1], \quad \nabla Z_1 = U_1 R_1, \quad (\text{G6})$$

1196 where the columns of P_0 are eigenvectors of Γ_1 which span its null space. Moreover, the following formulas generalize Eqs. (E14), (F8)), and
 1197 (F12):

$$1198 \quad W_1^\dagger \Gamma_1 H e_j \cdot W_1^\dagger \Gamma_1 H e_k = [\nabla Z_1]^\dagger H e_j \cdot [\nabla Z_1]^\dagger H e_k = Z_1^\dagger u_j \cdot Z_1^\dagger u_k. \quad (\text{G7})$$

1199 In this rank-deficient setting, these two approaches both yield discrete Stieltjes integral representations for the functional formulas in (G3)
 1200 for the symmetric \mathfrak{S}^* and antisymmetric \mathfrak{A}^* parts of the effective diffusivity matrix \mathfrak{D}^* . The two representations are equivalent by the relations
 1201 discussed above and are given by Eq. (39), with z_n and λ_n replaced by $z_n^1 = V_1 \Sigma_1^{-1} r_n^1$ and λ_n^1 , $n = 1, \dots, K_1$, where (λ_n^1, r_n^1) are eigenpairs of
 1202 matrix $-i U_1^T H U_1$. The results discussed here also hold for the setting where ∇ is of full-rank and therefore generalize the discrete mathematical
 1203 frameworks developed in Sec. IV and Appendices E and F.

1203 **Proof of Theorem 10.** We first work with Eq. (G2) directly and develop a mathematical framework which parallels the framework of
 1204 Sec. IV for the rank-deficient setting. We then transform Eq. (G2) into a discrete analog of Eq. (D9) written as $(\varepsilon l + \Gamma H \Gamma) \nabla \chi_j = -\Gamma H e_j$, with
 1205 a suitable generalization of the formula for the matrix Γ in (F2), and develop a mathematical framework which parallels the framework of

1206 We then generalize Lemma 9 of [Appendix F](#), establishing the equivalence of these two formulations for the rank-deficient setting
 1207 and, en route, derive a hybrid numerical algorithm for computing spectral representations of \mathfrak{D}^* which is more efficient than both of the
 1208 other numerical algorithms.

1209 Since $\Sigma = \text{diag}(\mathcal{O}_{00}, \Sigma_1)$, we have $\nabla = U_1 \Sigma_1 V_1^T$ and $\nabla^T \nabla = V_1 \Sigma_1^2 V_1^T$, so the cell problem in [\(G2\)](#) can be written as
 1210 $[V_1 \Sigma_1] [U_1^T H U_1] [\Sigma_1 V_1^T] \chi_j + \varepsilon V_1 \Sigma_1^2 V_1^T \chi_j = u_j$. The $K_1 \times K_1$ antisymmetric matrix $U_1^T H U_1$ has the spectral decomposition $U_1^T H U_1$
 1211 $= i R_1 \Lambda_1 R_1^\dagger$, where Λ_1 is a diagonal real-valued matrix and R_1 is a unitary matrix, $R_1^\dagger R_1 = R_1 R_1^\dagger = I_1$. Equation [\(G5\)](#) follows from these
 1212 formulas, which is an analog of Eq. [\(37\)](#). The formula $\nabla = U_1 \Sigma_1 V_1^T$ and Eq. [\(G5\)](#), in turn, imply that $\nabla \chi_j = U_1 R_1 (\varepsilon I_1 + i \Lambda_1)^{-1} [V_1 \Sigma_1^{-1} R_1]^\dagger u_j$.

1213 Substituting this formula for $\nabla \chi_j$ into the formula for \mathfrak{S}_{jk}^* in Eq. [\(G3\)](#) and using $U_1^T U_1 = I_1$ and $R_1^\dagger R_1 = I_1$ yield the functional formula
 1214 for \mathfrak{S}_{jk}^* in [\(38\)](#) with Λ replaced by Λ_1 and Z replaced by $Z_1 = V_1 \Sigma_1^{-1} R_1$. We also have

$$1215 \langle \nabla^T H \nabla \chi_j \cdot \chi_k \rangle = \langle i [V_1 \Sigma_1 R_1] \Lambda_1 [R_1^\dagger \Sigma_1 V_1^T] \chi_j \cdot \chi_k \rangle = \langle i [\Sigma_1 R_1 \Lambda_1 R_1^\dagger \Sigma_1] V_1^T \chi_j \cdot V_1^T \chi_k \rangle. \quad (G8)$$

1216 This formula, $R_1^\dagger R_1 = I_1$, $\Sigma_1^T = \Sigma_1$, and Eqs. [\(G3\)](#) and [\(G5\)](#) yield the functional formula for \mathfrak{A}_{jk}^* in [\(38\)](#) with Λ replaced by Λ_1 and Z replaced
 1217 by $Z_1 = V_1 \Sigma_1^{-1} R_1$. The quadratic form $Z_1^\dagger u_j \cdot Z_1^\dagger u_k$ arising in these functional formulas yields Eq. [\(42\)](#) with z_n replaced by $z_n^1 = V_1 \Sigma_1^{-1} r_n^1$ and
 1218 other appropriate notational changes, where r_n^1 , $n = 1, \dots, K_1$, are the orthonormal eigenvectors of the matrix $U_1^T H U_1$ which comprise the
 1219 columns of R_1 . The formula $z_n^1 = V_1 \Sigma_1^{-1} r_n^1$ can be written as $\nabla z_n^1 = U_1 r_n^1$. The orthogonality properties of R_1 and U_1 then imply that the
 1220 vectors z_n^1 satisfy the Sobolev-type orthogonality condition in Eq. [\(32\)](#), $\nabla z_n^1 \cdot \nabla z_m^1 = \delta_{nm}$. Moreover, since $\sum_n r_n^1 [r_n^1]^\dagger = I_1$, we also have Eq.
 1221 [\(G4\)](#). Consequently, the functional representations of \mathfrak{S}_{jk}^* and \mathfrak{A}_{jk}^* in Eq. [\(G3\)](#) have the discrete integral representations in Eq. [\(39\)](#) with
 1222 z_n and λ_n replaced by z_n^1 and λ_n^1 , and (λ_n^1, r_n^1) are eigenpairs of Hermitian matrix $-i U_1^T H U_1$ of size K_1 . These summations have the same
 1223 properties as the summations discussed in the Proof of Theorem 3 and Eqs. [\(44\)](#) and [\(45\)](#).

1224 We now argue that the mathematical framework developed so far in this proof generalizes the full-rank case in Sec. [IV](#). Indeed, in the
 1225 full-rank setting, the matrix $V_1 = V$ is orthogonal, $\Sigma_1 = \Sigma$ is invertible, and $R_1 = R$ is orthogonal so that the matrix $Z_1 = Z$ defined in [\(G5\)](#) is
 1226 given by $Z = V \Sigma^{-1} R$ and is invertible with $Z^{-1} = R^\dagger \Sigma V^T$. Equation [\(33\)](#) is satisfied with $Z^{-\dagger} = V \Sigma R$ and $\Lambda = \Lambda_1$ which, in turn, establishes the
 1227 current rank-deficient setting generalizes the full-rank setting summarized by Eqs. [\(30\)–\(42\)](#).

1228 We now generalize the mathematical framework developed in [Appendix E](#) to the case that the matrix ∇ is rank deficient. Using
 1229 $\nabla = U_1 \Sigma_1 V_1^T$, $\nabla^T \nabla = V_1 \Sigma_1^2 V_1^T$, $U_1^T U_1 = V_1^T V_1 = I_1$, and the invertibility of the matrix Σ_1 , the cell problem in [\(G2\)](#) can be written as
 1230 $U_1 [U_1^T H U_1] [U_1^T U_1] [\Sigma_1 V_1^T] \chi_j + \varepsilon U_1 \Sigma_1 V_1^T \chi_j = U_1 \Sigma_1^{-1} V_1^T u_j$. Substituting $u_j = -\nabla^T H e_j$ into this expression yields $(\varepsilon I + \Gamma_1 H \Gamma_1) \nabla \chi_j = g_j^1$, where
 1231 $\Gamma_1 = U_1 U_1^T$ and $g_j^1 = -\Gamma_1 H e_j$ which is analogous to Eq. [\(D9\)](#). As in [Appendix F](#), the matrix $\Gamma_1 = U_1 U_1^T$ projects subspaces of \mathbb{R}^N onto
 1232 the range of ∇ . The antisymmetric matrix $\Gamma_1 H \Gamma_1$ has the spectral decomposition $\Gamma_1 H \Gamma_1 = i W_1 \tilde{\Lambda} W_1^\dagger$, where $\tilde{\Lambda}$ is a diagonal real-valued
 1233 matrix and W_1 is a unitary matrix $W_1^\dagger W_1 = W_1 W_1^\dagger = I$, which yields a generalization of [\(E4\)](#). From $\Gamma_1 \nabla = \nabla$, we have $\langle \nabla^T H \nabla \chi_j \cdot \chi_k \rangle$
 1234 $= \langle \Gamma_1 H \Gamma_1 \nabla \chi_j \cdot \nabla \chi_k \rangle$. Exactly as in [Appendix E](#), these formulas lead to generalizations of Eqs. [\(E1\)–\(E14\)](#), with appropriate notational
 1235 changes for the rank-deficient setting. In the case that the matrix ∇ is of full-rank, we have $U_1 = U$ hence $W_1 = W$, which establishes
 1236 that the mathematical framework discussed in this paragraph generalizes the mathematical framework in [Appendix E](#) for the full-rank
 1237 setting.

1238 We now establish that these two different approaches provide equivalent spectral representations for the effective diffusivity matrix \mathfrak{D}^*
 1239 for the rank-deficient setting. In Eq. [\(E9\)](#) of Theorem 8, we wrote the eigenvalue decomposition $\Gamma = P G P^T$, where P is an orthogonal matrix
 1240 and G is a diagonal matrix. Moreover, we wrote $P = [P_0 \ P_1]$, where the columns of the matrices P_0 and P_1 are orthonormal eigenvectors
 1241 that span the null space and range of Γ , respectively. Since the eigenvalues γ_n associated with the eigenvectors in the matrix P_1 satisfy $\gamma_n = 1$,
 1242 any linear combination of the corresponding eigenvectors is also an eigenvector of Γ with eigenvalue $\gamma_n = 1$. Therefore, since the orthonormal
 1243 columns of the matrix U_1 span the range of $\Gamma_1 = U_1 U_1^T$, we may take $P_1 = U_1$ so that $P = [P_0 \ U_1]$. Consequently, we can rewrite Eq. [\(E11\)](#)
 1244 as $U_1^T H U_1 = i R_{11} \Lambda_{11} R_{11}^\dagger$. Identifying the notations of [Appendix E](#) with this section, we have $R_{11} = R_1$ and $\Lambda_{11} = \Lambda_1$. This equation and Eq.
 1245 [\(E12\)](#) establish that $\tilde{\Lambda} = \text{diag}(\mathcal{O}_{00}, \Lambda_1)$.

1246 We now establish that the spectral weights associated with each approach are identical. Using the notation of this section, Eq. [\(E12\)](#) yields
 1247 $W_1 = [P_0 \ U_1 R_1]$. Consequently, from $\nabla = U_1 \Sigma_1 V_1^T$, $U_1^T U_1 = V_1^T V_1 = I_1$, and the formula $Z_1 = V_1 \Sigma_1^{-1} R_1$ in [\(G5\)](#), we have that $\nabla Z_1 = U_1 R_1$,
 1248 implying Eq. [\(G6\)](#), which is a generalization of Eq. [\(F5\)](#). Equation [\(G7\)](#) now follows from $\Gamma_1^T = \Gamma_1$, $\Gamma_1 P_0 = O$, $\Gamma_1 U_1 = U_1$, and the formula
 1249 $u_j = -\nabla^T H e_j$ in [\(F11\)](#). This establishes that the spectral weights associated with both of the approaches discussed in Sec. [IV](#) and [Appendix E](#)
 1250 are identical which, in turn, establishes that both approaches provide equivalent spectral representations of the effective diffusivity matrix \mathfrak{D}^* .
 1251 This concludes our Proof of Theorem 10. \square

1252 In Sec. [V](#), spectral representations of the symmetric \mathfrak{S}^* and antisymmetric \mathfrak{A}^* parts of the effective diffusivity matrix \mathfrak{D}^* are computed
 1253 for various periodic flows, and spectral characteristics are related to flow geometry and transport properties. We accomplish this by using Eq.
 1254 [\(39\)](#) with z_n and λ_n replaced by $z_n^1 = V_1 \Sigma_1^{-1} r_n^1$ and λ_n^1 , respectively, where (λ_n^1, r_n^1) are eigenpairs of matrix $-i U_1^T H U_1$. We emphasize that this
 1255 matrix is of size K_1 which is more than a factor of d smaller than the matrix $-i \Gamma_1 H \Gamma_1$. Moreover, we have established that the discrete spectral
 1256 measure at the heart of the integral representation for \mathfrak{D}^* is given in terms of the standard eigenvalues and eigenvectors of $-i U_1^T H U_1$, which

is a less costly numerical computation than the computation associated with the *generalized eigenvalue problem*⁴⁷ in (31). Consequently, in the process of establishing the equivalence of the effective parameter problems discussed in Sec. IV and Appendix E for the rank-deficient setting, we have also developed a hybrid numerical algorithm that is more efficient at computing the spectral representation of \mathfrak{D}^* than both of the other approaches.

REFERENCES

- 1 N. I. Akhiezer, *The Classical Moment Problem* (Oliver & Boyd, 1965).
- 2 G. S. Aslanyan, I. L. Maikov, and I. Z. Filimonova, "Simulation of pulverized coal combustion in a turbulent flow," *Combust., Explos. Shock Waves* **30**(4), 448–453 (1994).
- 3 M. Avellaneda and A. Majda, "Stieltjes integral representation and effective diffusivity bounds for turbulent transport," *Phys. Rev. Lett.* **62**, 753–755 (1989).
- 4 M. Avellaneda and A. Majda, "An integral representation and bounds on the effective diffusivity in passive advection by laminar and turbulent flows," *Commun. Math. Phys.* **138**, 339–391 (1991).
- 5 M. Avellaneda and M. Vergassola, "Stieltjes integral representation of effective diffusivities in time-dependent flows," *Phys. Rev. E* **52**(3), 3249–3251 (1995).
- 6 G. A. Baker and P. R. Graves-Morris, *Padé Approximants*, Encyclopedia of Mathematics and Its Applications (Cambridge University Press, 1996).
- 7 A. Bensoussan, J.-L. Lions, and G. Papanicolaou, *Asymptotic Analysis for Periodic Structures* (North-Holland, Amsterdam, 1978).
- 8 D. J. Bergman, "Exactly solvable microscopic geometries and rigorous bounds for the complex dielectric constant of a two-component composite material," *Phys. Rev. Lett.* **44**, 1285–1287 (1980).
- 9 R. Bhattacharya, "Multiscale diffusion processes with periodic coefficients and an application to solute transport in porous media," *Ann. Appl. Probab.* **9**(4), 951–1020 (1999).
- 10 R. N. Bhattacharya, V. K. Gupta, and H. F. Walker, "Asymptotics of solute dispersion in periodic porous media," *SIAM J. Appl. Math.* **49**(1), 86–98 (1989).
- 11 L. Biferale, A. Crisanti, M. Vergassola, and A. Vulpiani, "Eddy diffusivities in scalar transport," *Phys. Fluids* **7**, 2725–2734 (1995).
- 12 R. W. Bilger, S. B. Pope, K. N. C. Bray, and J. F. Driscoll, "Paradigms in turbulent combustion research," *Proc. Combust. Inst.* **30**, 21–42 (2005).
- 13 J. Bonn and R. M. McLaughlin, "Sensitive enhanced diffusivities for flows with fluctuating mean winds: A two-parameter study," *J. Fluid Mech.* **445**, 345–375 (2001).
- 14 J. W. Demmel, *Applied Numerical Linear Algebra* (SIAM, 1997).
- 15 E. Di Lorenzo, D. Mountain, H. P. Batchelder, N. Bond, and E. E. Hofmann, "Advances in marine ecosystem dynamics from US GLOBEC: The horizontal-advection bottom-up forcing paradigm," *Oceanography* **26**(4), 22–33 (2013).
- 16 R. Durrett, *Probability: Theory and Examples*, 4th ed. (Cambridge University Press, 2010).
- 17 A. Fannjiang and G. Papanicolaou, "Convection enhanced diffusion for periodic flows," *SIAM J. Appl. Math.* **54**(2), 333–408 (1994).
- 18 A. Fannjiang and G. Papanicolaou, "Convection-enhanced diffusion for random flows," *J. Stat. Phys.* **88**(5–6), 1033–1076 (1997).
- 19 G. B. Folland, *Introduction to Partial Differential Equations* (Princeton University Press, Princeton, NJ, 1995).
- 20 G. B. Folland, *Real Analysis: Modern Techniques and Their Applications* (Wiley-Interscience, New York, NY, 1999).
- 21 K. M. Golden, H. Eicken, A. L. Heaton, J. Miner, D. Pringle, and J. Zhu, "Thermal evolution of permeability and microstructure in sea ice," *Geophys. Res. Lett.* **34**, L16501, <https://doi.org/10.1029/2007gl030447> (2007).
- 22 K. M. Golden and G. Papanicolaou, "Bounds for effective parameters of heterogeneous media by analytic continuation," *Commun. Math. Phys.* **90**, 473–491 (1983).
- 23 Y. Gorb, D. Nam, and A. Novikov, "Numerical simulations of diffusion in cellular flows at high Pécel numbers," *Discrete Contin. Dyn. Syst., Ser. B* **15**(1), 75–92 (2011).
- 24 E. E. Hofmann and E. J. Murphy, "Advection, krill, and Antarctic marine ecosystems," *Antarct. Sci.* **16**(04), 487–499 (2004).
- 25 R. A. Horn and C. R. Johnson, *Matrix Analysis* (Cambridge University Press, 1990).
- 26 M. B. Isichenko and J. Kalda, "Statistical topography. II. 2D transport of passive scalar," *J. Nonlinear Sci.* **1**(4), 375–396 (1991).
- 27 J. D. Jackson, *Classical Electrodynamics* (John Wiley & Sons, New York, 1999).
- 28 J. P. Keener, *Principles of Applied Mathematics: Transformation and Approximation*, Advanced Book Program (Westview Press, Cambridge, MA, 2000).
- 29 D. Khoshnevisan, *Probability*, Graduate Studies in Mathematics (American Mathematical Society, 2007).
- 30 N. Kraitzman, R. Hardenbrook, N. B. Murphy, E. Cherkaev, J. Zhu, and K. M. Golden, "Bounds on convection enhanced thermal transport in sea ice," preprint arXiv:■ (2019).
- 31 J. V. Lukovich, D. G. Babb, and D. G. Barber, "On the scaling laws derived from ice beacon trajectories in the southern Beaufort Sea during the International Polar Year—Circumpolar Flaw Lead study, 2007–2008," *J. Geophys. Res.: Oceans* **116**(C9), C00G07, <https://doi.org/10.1029/2011jc007049> (2011).
- 32 V. I. Lytle and S. F. Ackley, "Heat flux through sea ice in the Western Weddell Sea: Convective and conductive transfer processes," *J. Geophys. Res.* **101**(C4), 8853–8868, <https://doi.org/10.1029/95jc03675> (1996).
- 33 A. Majda and P. R. Kramer, *Simplified Models for Turbulent Diffusion: Theory, Numerical Modelling, and Physical Phenomena*, Physics Reports (North-Holland, 1999).
- 34 A. J. Majda and P. E. Souganidis, "Large scale front dynamics for turbulent reaction-diffusion equations with separated velocity scales," *Nonlinearity* **7**(1), 1–30 (1994).
- 35 D. McLaughlin, G. Papanicolaou, and O. Pironneau, "Convection of microstructure and related problems," *SIAM J. Appl. Math.* **45**, 780–797 (1985).
- 36 R. M. McLaughlin and M. G. Forest, "An anelastic, scale-separated model for mixing, with application to atmospheric transport phenomena," *Phys. Fluids* **11**(4), 880–892 (1999).
- 37 R. C. McOwen, *Partial Differential Equations: Methods and Applications* (Prentice Hall PTR, 2003).
- 38 Y. A. Melnikov and M. Y. Melnikov, *Green's Functions: Construction and Applications*, De Gruyter Studies in Mathematics (De Gruyter, 2012).
- 39 G. W. Milton, "Bounds on the complex dielectric constant of a composite material," *Appl. Phys. Lett.* **37**, 300–302 (1980).
- 40 G. W. Milton, *Theory of Composites* (Cambridge University Press, Cambridge, 2002).
- 41 H. K. Moffatt, "Transport effects associated with turbulence with particular attention to the influence of helicity," *Rep. Prog. Phys.* **46**(5), 621–664 (1983).
- 42 N. B. Murphy, E. Cherkaev, C. Hohenegger, and K. M. Golden, "Spectral measure computations for composite materials," *Commun. Math. Sci.* **13**(4), 825–862 (2015).
- 43 N. B. Murphy, E. Cherkaev, J. Xin, and K. M. Golden, "Spectral measures and iterative bounds for effective diffusivity for periodic flows" (unpublished).
- 44 N. B. Murphy, E. Cherkaev, J. Xin, J. Zhu, and K. M. Golden, "Spectral analysis and computation of effective diffusivities in space-time periodic incompressible flows," *Ann. Math. Sci. Appl.* **2**, 3–66 (2017).

- 1314 ⁴⁵N. Benjamin Murphy, E. Cherkaev, and K. M. Golden, "Anderson transition for classical transport in composite materials," *Phys. Rev. Lett.* **118**, 036401 (2017).
1315 ⁴⁶G. Papanicolaou and S. Varadhan, "Boundary value problems with rapidly oscillating coefficients," in *Colloquia Mathematica Societatis János Bolyai*, Random Fields
1316 (Esztergom, Hungary 1979) (North-Holland, 1982), Vol. 27, pp. 835–873.
1317 ⁴⁷B. N. Parlett, *The Symmetric Eigenvalue Problem* (Prentice-Hall, Upper Saddle River, NJ, USA, 1998).
1318 ⁴⁸G. A. Pavliotis, "Homogenization theory for advection-diffusion equations with mean flow," Ph.D. thesis, Rensselaer Polytechnic Institute Troy, New York, 2002.
1319 ⁴⁹G. A. Pavliotis, "Asymptotic analysis of the Green–Kubo formula," *IMA J. Appl. Math.* **75**, 951–967 (2010).
1320 ⁵⁰N. Peters, *Turbulent Combustion*, Cambridge Monographs on Mechanics (Cambridge University Press, 2000).
1321 ⁵¹P. Rampal, J. Weiss, D. Marsan, and M. Bourgoin, "Arctic sea ice velocity field: General circulation and turbulent-like fluctuations," *J. Geophys. Res.: Oceans* **114**(C10),
1322 C10014, <https://doi.org/10.1029/2008jc005227> (2009).
1323 ⁵²P. Rampal, J. Weiss, D. Marsan, R. Lindsay, and H. Stern, "Scaling properties of sea ice deformation from buoy dispersion analysis," *J. Geophys. Res.: Oceans* **113**(C3),
1324 C03002, <https://doi.org/10.1029/2007jc004143> (2008).
1325 ⁵³M. C. Reed and B. Simon, *Functional Analysis* (Academic Press, San Diego, CA, 1980).
1326 ⁵⁴W. Rudin, *Real and Complex Analysis* (McGraw-Hill, New York, NY, 1987).
1327 ⁵⁵P. J. Samson, "Atmospheric transport and dispersion of air pollutants associated with vehicular emissions," in *Air Pollution, The Automobile, and Public Health*, edited
1328 by A. Y. Watson, R. R. Bates, and D. Kennedy (National Academy Press, US, 1988), pp. 77–97.
1329 ⁵⁶I. Stakgold, *Boundary Value Problems of Mathematical Physics*, Classics in Applied Mathematics (SIAM, 2000), Vol. 2, set.
1330 ⁵⁷T.-J. Stieltjes, "Recherches sur les fractions continues," *Ann. Fact. Sci. Toulouse*, **4**(1), J1–J35 (1995).
1331 ⁵⁸M. H. Stone, *Linear Transformations in Hilbert Space* (American Mathematical Society, Providence, RI, 1964).
1332 ⁵⁹R. J. Tabaczynski, "Turbulent flows in reciprocating internal combustion engines," in *Internal Combustion Engineering: Science and Technology*, edited by J. H. Weaving
1333 (Springer Netherlands, 1990), pp. 243–285.
1334 ⁶⁰G. I. Taylor, "Eddy motion in the atmosphere," *Philos. Trans. Royal Soc. A* **215**(523–537), 1–26 (1915).
1335 ⁶¹G. I. Taylor, "Diffusion by continuous movements," *Proc. London Math. Soc.: Third Series* **2**, 196–212 (1921).
1336 ⁶²H. J. Trodahl, S. O. F. Wilkinson, M. J. McGuinness, and T. G. Haskell, "Thermal conductivity of sea ice; dependence on temperature and depth," *Geophys. Res. Lett.*
1337 **28**(7), 1279–1282, <https://doi.org/10.1029/2000gl012088> (2001).
1338 ⁶³W. M. Washington and C. L. Parkinson, *An Introduction to Three-Dimensional Climate Modeling* (University Science Books, 1986).
1339 ⁶⁴E. Watanabe and H. Hasumi, "Pacific water transport in the western Arctic Ocean simulated by an eddy-resolving coupled sea ice–ocean model," *J. Phys. Oceanogr.*
1340 **39**(9), 2194–2211 (2009).
1341 ⁶⁵F. A. Williams, *Turbulent Combustion*, Frontiers in Applied Mathematics (Society for Industrial and Applied Mathematics (SIAM), Philadelphia, PA, 1985), Chap. 3,
1342 pp. 97–131.
1343 ⁶⁶J. Xin, *An Introduction to Fronts in Random Media*, Surveys and Tutorials in the Applied Mathematical Sciences (Springer, New York, 2009).



Q1

- 1335
1336
1337
1338
1339
1340
1341
1342
1343